

ABSTRACT

CHESTNUT, MELANIE MARIE. Using HYSCORE Spectroscopy for High Spatial Resolution Profiling of Water Concentrations in Lipid Membranes and Elucidating the Electronic Structure of the Primary Electron Donor $P_{700}^{+\bullet}$ in Photosystem I. (Under the direction of Dr. Alex I. Smirnov).

The first chapter of this work addresses the problem of measuring local water concentrations in highly heterogeneous systems in particular lipid bilayer membranes. Water is not only the driving force of self-assembly of lipid bilayers, but is crucial for the structure and function of membrane-associated proteins. Because lipid bilayers display large polarity gradients on very small length scales, it is difficult to experimentally build water permeation profiles with sufficient spatial resolution.

We propose a novel method to measure the concentration of water in lipid membranes with higher spatial resolution, based on hydrogen bonds formed between water molecules and nitroxide spin probes located at certain depths in the membrane. By directly measuring the fraction of H-bonded nitroxides using hyperfine sublevel correlation (HYSCORE) spectroscopy and estimating parameters relating to the H-bonding equilibrium constants between water(s) and EPR spin probes, we are able to obtain the local water concentration with spatial resolution that corresponds to the H-bonding reaction radius, $\sim 2 \text{ \AA}$.

Application of the method has been demonstrated in POPG bilayers using spin labeled stearic acid with a doxyl moiety on the 5th or 16th carbon atom positions along the acyl chain. Further, water concentration was profiled along a lipid-peptide interface using DOPC lipid bilayers doped with WALP-23, a membrane spanning, α -helical peptide with 23 residues, that was spin labeled with a nitroxide MTSL at various residue positions along the peptide.

The proposed HYSCORE method has also been extended for the detection of lithium ions. We demonstrate that $^7\text{Li}^+$ can not only be detected with HYSCORE but also its local concentration

could be determined. Further, we speculate that sensitivity of our method with respect to Li^+ detection could be improved by designing nitroxides with cation chelating groups.

Chapter 2 of this thesis describes multi-frequency (X- and Q-band) studies of the electronic structure of $\text{P}_{700}^{+\bullet}$ in PSI from thermophilic cyanobacterium *Synechococcus elongates* by HYSCORE spectroscopy. Six distinct types of ^{14}N and two ^1H nuclei were resolved by the combination of HYSCORE methods, yielding estimates of their magnetic interaction parameters, i.e. the principal values of the electron-nuclear hyperfine, as well as quadrupole interaction tensors (for ^{14}N). All the detected ^{14}N nuclei were tentatively assigned to the pyrrole ring nitrogen atoms of the $\text{P}_{700}^{+\bullet}$ radical, strongly indicating the dimeric nature of the P_{700} heterodimer.

© Copyright 2020 by Melanie Chestnut

All Rights Reserved

Using HYSORE Spectroscopy for High Spatial Resolution Profiling of Water Concentrations
in Lipid Membranes and Elucidating the Electronic Structure of the Primary
Electron Donor $P_{700}^{+\bullet}$ in Photosystem I.

by
Melanie Marie Chestnut

A dissertation submitted to the Graduate Faculty of
North Carolina State University
in partial fulfillment of the
requirements for the degree of
Doctor of Philosophy

Chemistry

Raleigh, North Carolina
2020

APPROVED BY:

Alex Smirnov
Committee Chair

Alex Nevzorov

Thomas Theis

Don Brenner

DEDICATION

To Mr. Landy (Warren Central), Dr. Philipp (Hanover College), my mom Susie, my dad Steve, and my brother Andrew.

BIOGRAPHY

Melanie Marie Chestnut was born in Indianapolis, Indiana, on June 20, 1990. She went to public schools in Indianapolis. Toward the end of high school, she attended a physics research program at Indiana University-Purdue University of Indianapolis. Besides art and music, she also loved sports—she became a state champion gymnast and also enjoyed golf, playing on the varsity team her first year at Hanover College. At Hanover, she became interested in chemistry. She did research in analytical chemistry, and her research was accepted to the Sci Mix at American Chemical Society National Convention, honoring the top 10% of abstracts in all divisions. She graduated from Hanover with a BA in Chemistry and minor in Mathematics. She then attended North Carolina State University, where she became especially interested in physical chemistry and in particular, electron paramagnetic resonance (EPR). After a short time in the field, she won a Young Investigator Award for the best poster at an international EPR conference.

TABLE OF CONTENTS

LIST OF TABLES	vi
LIST OF FIGURES	vii
Chapter 1: Profiling local water concentration in biological membranes down to ~2 Å spatial resolution by HYSCORE spectroscopy of nitroxide spin labels.	1
Section 1: Introduction.....	1
1.1. Lipid bilayers and associated proteins	1
1.2. Importance of hydration of cell membranes	3
Section 2: Existing methods to measure polarity profiles and/or water concentration in membranes	6
2.1. Continuous Wave (CW) EPR Spectroscopy	6
2.2. Electron Spin Echo Envelope Modulation (ESEEM) Spectroscopy	10
2.3. Overhauser Dynamic Nuclear Polarization (DNP).....	12
Section 3: Proposed Method to Measure Water Concentration in Membranes.....	14
3.1. Main idea of proposed method	14
3.2. HYSCORE spectroscopy as the optimal method to measure $\mathcal{F}_{\text{H-bond}}$	18
3.3. Basic principles of HYSCORE spectroscopy	20
3.4. Relation between HYSCORE signal and $\mathcal{F}_{\text{H-bond}}$	23
3.5. Use of ethanol-toluene model system to estimate K_d	26
Section 4: Experimental Methods	27
4.1. Sample preparation	27
4.1.1. POPG bilayers doped with doxyl stearic acids	27
4.1.2. DOPC bilayers doped with WALP-n-MTSL.....	27
4.2. EPR spectroscopy	29
4.3. Results and Discussion	30
4.3.1. Model system to mimic nonpolar region of hydrated lipid bilayer	30
4.3.2. Estimation of equilibrium constants by HYSCORE $\mathcal{F}_{\text{H-bond}}$ measurements	33
4.3.3. Comparison with the CW EPR spectroscopy at room temperature	37
4.3.4. Water concentration measurements	39
4.3.4.1. POPG bilayers doped with doxyl stearic acids	39
4.3.4.2. DOPC bilayers doped with WALP-n-MTSL (lipid-peptide interface).....	42
4.3.5. Comparison to existing methods.....	47
Section 5: Extension of the Proposed Method to Measure Local Lithium Ion Concentrations. .	49
5.1. Introduction.....	49
5.2. Preliminary results and outlook	51
CHAPTER 1 REFERENCES	56

Chapter 2: Electronic Structure of the Primary Electron Donor $P_{700}^{+\bullet}$ in Photosystem I Studied by Multifrequency HYSCORE Spectroscopy at X- and Q-Band.....	63
Section 1: Introduction.....	63
Section 2: Materials and Methods.....	68
2.1. Sample Preparation	68
2.2. EPR Spectroscopy.....	69
2.2.1. X-Band EPR.....	69
2.2.2. Q-Band EPR.....	70
2.2.3. Signal processing and analysis of HYSCORE spectra	70
Section 3: Results and Discussion	72
3.1. Field Swept Echo-Detected EPR Spectra of $P_{700}^{+\bullet}$	72
3.2. X-Band 4-pulse HYSCORE of $P_{700}^{+\bullet}$	74
3.3. X-Band 6-pulse HYSCORE of $P_{700}^{+\bullet}$	81
3.4. Q-Band HYSCORE of $P_{700}^{+\bullet}$	86
3.5. Spin density distribution in $P_{700}^{+\bullet}$	89
Section 4: Summary and Outlook.....	93
 CHAPTER 2 REFERENCES	 95

LIST OF TABLES

Table 1.1. Sequences of WALP23 peptides with single cysteine mutations of the n th residue position.....	28
Table 1.2. Experimental and kinetic parameters obtained by least square minimization procedure. In the parenthesis are the 95% confidence bounds.....	36
Table 2.1. ¹⁴ N and ¹ H hyperfine interaction parameters of P ₇₀₀ ⁺ • obtained from experimental HYSORE spectra.	86

LIST OF FIGURES

Figure 1.1. Lipid Bilayer Structure (A) and the Composition of a glycerophospholipid Molecule (B-D)	1
Figure 1.2. (A) Density distribution of different groups in a DOPC lipid bilayer. (B) Polarity profile of a DOPC bilayer (Wiener & White, Structure of a fluid dioleoylphosphatidylcholine bilayer determined by joint refinement of x-ray and neutron diffraction data. III. Complete structure., 1992).....	5
Figure 1.3. Polarity index vs distance of the spin label from bilayer center, based on measuring of the nitroxide hyperfine splitting constants using CW-EPR spectroscopy	8
Figure 1.4. Accessibility measurements of hydrophobic oxygen and hydrophilic chromium oxide, paramagnetic complexes, obtained using CW-EPR spectroscopy	9
Figure 1.5. (A) Pulse sequence used in a 3-pulse ESEEM experiment. (B) The energy diagram of spin sublevels of an unpaired electron (electron spin $S=1/2$) magnetically interacting with a nucleus (nuclear spin $I=1/2$) in presence of external magnetic field	11
Figure 1.6. Contribution of the ESEEM signal by nuclei as a function of the distance of nuclei from the paramagnetic center.	12
Figure 1.7. Normalized DNP parameter vs. spin label position, obtained by Overhauser DNP of MTSL-labeled WALP peptide in DOPC bilayers.....	13
Figure 1.8. Reversible hydrogen bonding interactions between nitroxide (Tempo) and water molecules.	15
Figure 1.9. Typical 4-pulse sequence of a HYSCORE Experiment.....	21
Figure 1.10. Hyperfine splittings measured by HYSCORE Spectroscopy and corresponding cross-correlation peaks	22
Figure 1.11. HYSCORE Spectrum of TEMPOL spin probe in frozen D_2O /glycerol solution and its corresponding Skyline Projection. High resolution of HYSCORE enables the selective detection of bonded water molecule(s) with very high sensitivity (small fractions, f_{H-Bond}).	23

Figure 1.12. Spin labeling reaction of the sulfhydryl group of a cysteine residue with the spin label 1-oxyl-2,2,5,5-tetramethylpyrroline-3-methyl-methanethio-sulfonate (MTSL), producing a nitroxide side chain	29
Figure 1.13. Frozen glass ^2H -HYSCORE spectra of TEMPOL spin probes in D_2O (50% vol. mixture with diglyme), CH_3OD , $\text{CH}_3\text{CH}_2\text{OD}$ and $\text{CH}_3\text{CHODCH}_3$	31
Figure 1.14. Normalized HYSCORE signal intensity of the hydrogen bonded deuteron for frozen glasses of partially deuterated water and three alcohols in diglyme using TEMPOL	33
Figure 1.15. Normalized HYSCORE signal intensity of the hydrogen bonded deuteron (H_D/A_{Echo}) to TEMPO for frozen CH_3OD in toluene.....	34
Figure 1.16. Normalized HYSCORE signal intensity of the hydrogen bonded deuteron (H_D/A_{Echo}) for frozen $\text{CH}_3\text{CH}_2\text{OD}$ in toluene using TEMPO	35
Figure 1.17. Isotropic nitrogen hyperfine coupling constants obtained for 20 μM Tempo in alcohol-toluene mixtures for both protonated and selectively deuterated methanol and ethanol.....	37
Figure 1.18. Normalized change of the isotropic nitrogen hyperfine coupling constants obtained for 20 μM Tempo in alcohol-toluene mixtures for both protonated and selectively deuterated methanol and ethanol.	38
Figure 1.19. HYSCORE spectrum of 5-DSA in POPG Bilayers.	40
Figure 1.20. HYSCORE spectrum of 16-DSA in POPG Bilayers	41
Figure 1.21. Water concentration profile obtained along WALP-DOPC bilayer interface using the proposed HYSCORE method and Tempo radical solution in methanol-toluene as a model system.	42
Figure 1.22. Water concentration profile obtained along WALP-DOPC bilayer interface using the proposed HYSCORE method and Tempo radical solution in ethanol-toluene as a model system.	43
Figure 1.23. Profile of relative concentration of water given in arbitrary units as obtained along WALP-DOPC bilayer interface using the 3-pulse ESEEM method.	46
Figure 1.24. Accessibility parameter of D_2O vs position obtained by 3-Pulse ESEEM of MTSL-WALP in DOPC bilayers	47
Figure 1.25. Normalized DNP parameter vs position obtained by Overhauser DNP of	

MTSL-WALP in DOPC bilayers	48
Figure 1.26. HYSCORE spectrum measured for TEMPO radicals in frozen MTHF glass in presence of 1M of LiClO ₄	51
Figure 1.27. Lithium ridges plotted in squared frequency coordinates from the HYSCORE spectrum measured for TEMPO radicals in frozen MTHF glass in presence of 1M of LiClO ₄	52
Figure 1.28. Dependence of HYSCORE signal intensity of matrix as well as nitroxide-bound ⁷ Li nuclei on concentration of LiClO ₄ salt in frozen MTHF.....	54
Figure 1.29. Compounds 1 and 2 (Amitina & Volodarskii, 1976); Compounds 4 and 5 (Grigor'ev, et al., 1985); Compounds 3 and 5 (Grigor'ev, Shchukin, Dikanov, Kuznetsova, & Volodarskii, 1982).....	55
Figure 2.1. Echo-detected field-swept spectra of the primary electron donor P ₇₀₀ ^{+•} in the oxidized state at X- (A) and Q-band (B) EPR frequencies. The arrows indicate the magnetic field positions for the respective HYSCORE experiments.....	73
Figure 2.2. (A) Experimental X-band 4-pulse HYSCORE spectrum of P ₇₀₀ ^{+•} measured at a delay of 120 ns between the first (π/2) and the second (π/2) microwave pulses. Spectral regions corresponding to multi-quantum nuclear transitions are denoted with red text. (B) Simulated 4-pulse HYSCORE spectrum yielding the best agreement with the experimental spectrum	74
Figure 2.3. Selected regions of the experimental X-band HYSCORE spectrum shown in Figure 2.2A corresponding to the DQ and SQ spectral features. (A) Zoomed (-,+) quadrant region with DQ-DQ ridges of N ₁ -N ₃ . (B) Zoomed (+,+) region with DQ-DQ and 3-pulse ESEEM ridges of N ₃ -N ₄	77
Figure 2.4. Selected region of the (-,+) quadrant (A) and (+,+) quadrant (B) of X-band 6-pulse HYSCORE spectrum of P ₇₀₀ ^{+•} measured with an inter-pulse delays of 68 ns and 120 ns between the first two and the last two microwave pulses, respectively. (C) Selected region of the (+,+) quadrant of the X-band 6-pulse HYSCORE spectrum of P ₇₀₀ ^{+•} measured with an inter-pulse delays of 68 ns and 234 ns between the first two and the last two microwave pulses, respectively. (D) Simulated HYSCORE spectrum of N ₅ and N ₆ nuclei.	81
Figure 2.5. (A) X-band ¹ H-HYSCORE spectrum obtained using 6-pulse sequence with 68 ns inter-pulse separation between the first two pulses and 120 ns inter-pulse delay between the last two pulses. (B) (+,+) quadrant of 4-pulse Q-band HYSCORE spectrum obtained with 140 ns separation between the first two pulses. (C) (+,+) quadrant of Q-band 6-pulse HYSCORE spectrum obtained with 68 ns inter-pulse separation between the first two pulses and 140 ns inter-pulse delay between the last two pulses (D) Simulated Q-band	

4-pulse HYSCORE spectrum of N_1 - N_4 nuclei. Contributions from N_5 and N_6 were neglected..... 87

CHAPTER 1

Section 1

1.1. Lipid bilayers and associated proteins

Cellular membranes are protective, semi-permeable barriers that encase the entire cell, and, in eukaryotes, the internal components of the cell. Almost all cellular membranes are made up of glycerophospholipids which self-assemble into a bilayer structure. **Figure 1.1** shows this bilayer structure, in which the hydrophilic head groups face outward and the hydrophobic hydrocarbon tails line up in the interior. The polar head group consists of choline (blue) and phosphate (orange) moieties. A glycerol moiety (green) connects the head group to the hydrophobic tails, also called fatty acids (purple). The typical bilayer thickness is 30-40 Å.

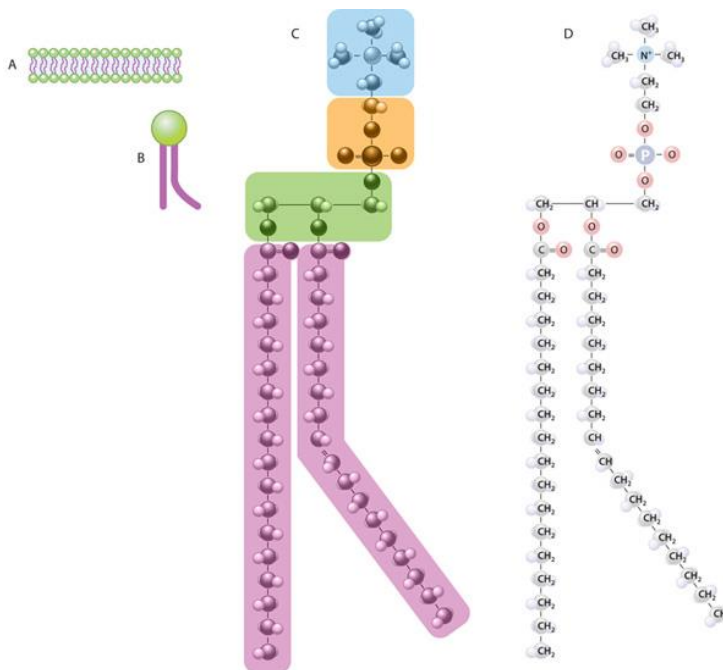


Figure 1.1. Lipid Bilayer Structure (A) and the Composition of a Glycerophospholipid Molecule (B-D). (O'Connor & Adams, 2010)

The plasma membranes of animal cells in addition to phospholipids also contain cholesterol, which affects the rigidity of the membrane. Membranes contain various types of proteins, accounting for about half of their mass (O'Connor & Adams, 2010). Integral membrane proteins are permanently attached to cellular membranes and typically span through the membranes. Peripheral proteins adhere to the membranes only temporarily by attaching to integral membrane proteins or penetrating the peripheral regions of the lipid bilayer.

Membrane proteins carry out a variety of functions, and are involved in many biological processes including photosynthesis, respiration, signal transduction, catalysis, and molecular transport (O'Connor & Adams, 2010). For example, membrane proteins may perform communication-related tasks, such as binding extracellular hormones or immune mediator molecules in highly specific pockets, or active sites; binding of these ligand molecules results in conformational changes of the proteins, which active intracellular processes.

Approximately a third of all proteins are membrane proteins, but only about 1% of known protein structures are membrane proteins. Membrane proteins remain one of the most challenging targets in structural biology as the major challenges remain to obtain high yields of stable and functional proteins and to re-solubilize the purified or expressed proteins in lipid environments, while maintaining functionality and native conformations. Membrane proteins are generally not soluble in aqueous solution, and require either lipid or detergent molecules for solubilization. Crystallization of membrane proteins is difficult, but has been accomplished for more than a handful of membrane proteins. The latter account for the most of the structures deposited in the protein data bank (PDB) although recently protein structures obtained by cryoEM were making rapid gains.

1.2. Importance of hydration of cellular membranes

Cellular membranes are semi-permeable to several molecules. While small hydrophobic molecules and many gases including oxygen and carbon dioxide diffuse rapidly across the membranes, small, polar molecules (e.g., water and ethanol), diffuse across membranes more slowly (O'Connor & Adams, 2010). Most ions and large molecules (e.g., sugars and amino acids) do not cross the membrane by diffusion in sufficient quantities but rely on specific transport proteins embedded in the membrane. The transport proteins often require additional energy to move molecules across the membrane, especially when pumping molecules against the concentration gradient.

Preventing the passive transport of charged molecules through the membrane is also a function of the hydrophobic membrane barrier. The location of the hydrophobic membrane barrier is largely determined by water permeation into the membrane, and is a function of alkyl length, saturation, and cholesterol mole fraction (Subczynski, Wisniewska, Hyde, & Kusumi, 1994). The membrane barrier is a reflection of the polarity profile of the membrane, such as the one in **Figure 1.2**, which was obtained by a combined refinement of X-ray and neutron diffraction data (Wiener & White 1992). In addition to the transport of small molecules, the hydrophobic membrane barrier also plays a role in stability of transmembrane proteins and governs the insertion of proteins and protein segments into the membrane (Marsh, 2001).

As mentioned earlier, lipid molecules would self-assemble into lipid bilayers when dispersed in water. This self-assembly is driven by water due to hydrophobic interactions with amphiphilic phospholipid molecules. Water is also crucial for stability and function of membrane-associated proteins. For example, water molecules stabilize transmembrane proteins by acting as a bridge between protein segments. Water molecules also stabilize transitional states of proteins,

such as those found in metalloprotein active sites. Water in the membrane plays roles in dynamics of protein segments, and significantly affects many types of membrane protein functions. Hydration waters at the membrane interface play a role in stabilization and insertion of proteins and protein segments, because many types of interactions are possible at the interface, and there is a steep water concentration gradient that helps to stabilize polar and nonpolar regions of proteins.

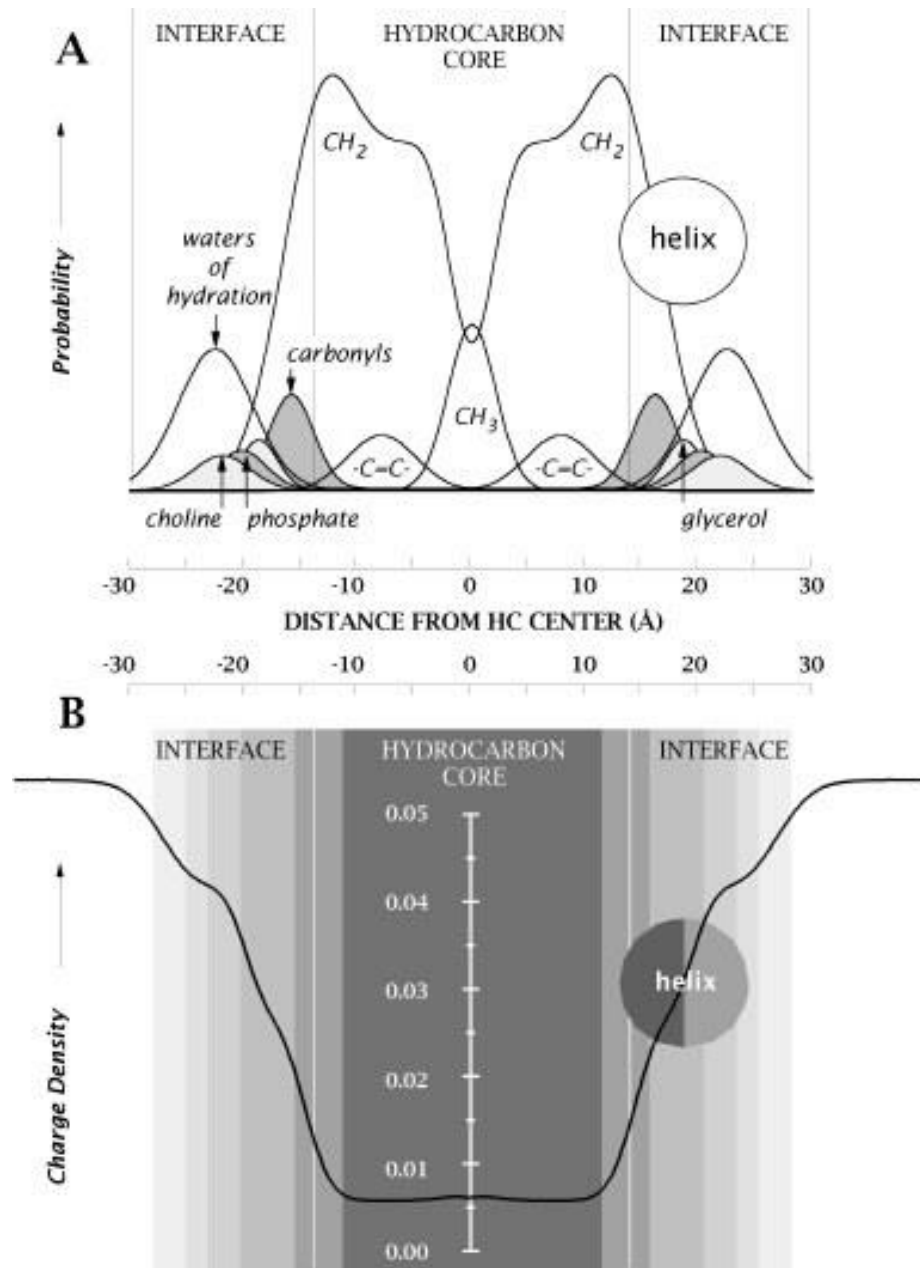


Figure 1.2. (A) Density distribution of different groups in a DOPC lipid bilayer. (B) Polarity profile of a DOPC bilayer (Wiener & White, Structure of a fluid dioleoylphosphatidylcholine bilayer determined by joint refinement of x-ray and neutron diffraction data. III. Complete structure., 1992)

Section 2.

Existing methods to measure polarity profiles and/or water concentration in membranes

While X-ray and neutron diffraction methods are highly powerful and precise in resolving crystalline samples, the resolutions of these methods are rather poor for semi-disordered systems, such as lipid membranes. Thus, it is very important to have precise, accurate, and sensitive spectroscopic tools to measure water concentration profiles across lipid bilayer systems with high spatial resolution. It is also important that these tools are sensitive enough to detect small water concentrations that are expected in the hydrophobic regions of these membranes.

However, due to the nature of the very steep gradients on very small length scales (typical bilayer thickness is only $\sim 30\text{-}40 \text{ \AA}$), profiling of water permeation with sufficient spatial resolution is challenging.

Many of the existing methods to study water permeation in membranes are based on magnetic resonance spectroscopy in conjunction with site-directed spin labeling (SDSL) of paramagnetic EPR spin probes, such as nitroxides. Those will be reviewed in the following sections.

2.1. Continuous Wave (CW) EPR Spectroscopy

Methods based on Continuous Wave (CW) EPR Spectroscopy can be divided into two groups. The first group is based on evaluation of solvent-dependent nitroxide magnetic parameters, usually the isotropic component of hyperfine coupling constant A_{iso}^N of the N-O \bullet group nitrogen and the g-tensor anisotropy, both of which depend on local environmental polarity and hydrogen bonding.

Because g-factor resolution at conventional EPR frequencies, such as X-band (9.5 GHz), is insufficient to measure changes in solvent polarity or hydrogen bonding accurately, more focus has been made on evaluating polarity effects from measuring the N–O• group nitrogen hyperfine coupling constants (Smirnova & Smirnov, 2007).

One of the first demonstrations of the use EPR and spin-labeling methods to reveal water penetration into a lipid bilayer and to deduce the shape of the hydrophobic membrane barrier has been provided by Griffith and coworkers (1974) who relied on the dependence of the isotropic nitrogen hyperfine coupling constant on the solvent polarity index (Griffith, Dehlinger, & Van, 1974). **Figure 1.3** shows the polarity index as a function of distance from the membrane center derived from such measurements.

Measurements of the isotropic nitrogen hyperfine coupling constants for nitroxide could be carried out at room or elevated temperatures by CW-EPR spectroscopy. However, there are some important drawbacks of this technique. First, nitrogen hyperfine coupling depends simultaneously on solvent polarity and proticity, and separation of these components is a difficult task. Second, extraction of nitrogen hyperfine parameters is rather simple for nitroxide spectra following into the fast motion limit, in which all disturbing anisotropies are averaged out. In proteins and membranes, however, movement of a spin label is usually hindered sterically, decreasing spin label mobility. Such decreased mobility results in incomplete averaging of the magnetic anisotropies, usually making the observed CW-EPR spectra rather complicated. Thus, sufficiently accurate measurements of nitrogen hyperfine coupling parameters in biological samples are not always possible.

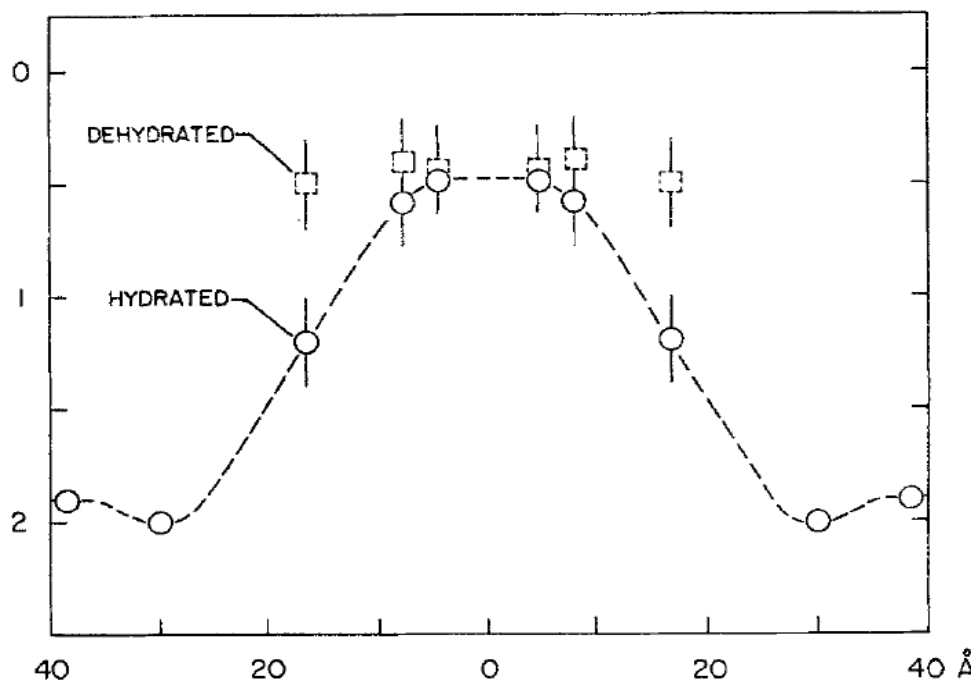


Figure 1.3. Polarity index vs distance of the spin label from bilayer center, based on measuring of the nitroxide hyperfine splitting constants using CW-EPR spectroscopy (Griffith, Dehlinger, & Van, 1974).

The second group of CW-EPR based measurements is based on the nitroxide relaxation enhancement by hydrophilic or hydrophobic paramagnetic complexes. Nitroxides in more nonpolar environments experience enhanced relaxation by hydrophobic paramagnetic molecules (i.e., apolar molecular oxygen). Nitroxides in more polar environments experience enhanced relaxation by hydrophilic paramagnetic complexes (i.e., chromium oxide). This is because molecular oxygen is more accessible to hydrophobic regions, and chromium oxide is more accessible to hydrophilic regions. **Figure 1.4** shows accessibility measurements of apolar molecular oxygen and chromium oxide in lipid bilayers, based on nitroxide relaxation measurements (Farahbakhsh, Altenbach, & Hubbell, 1992).

Changes in nitroxide relaxation (relaxation enhancement) are manifested in the changes in EPR spectral linewidth. Accessibility parameters can be indirectly derived from relaxation enhancement measurements using hydrophilic and hydrophobic paramagnetic complexes.

In spite of the relative experimental simplicity of this method, the accessibility parameters cannot be related to water concentration.

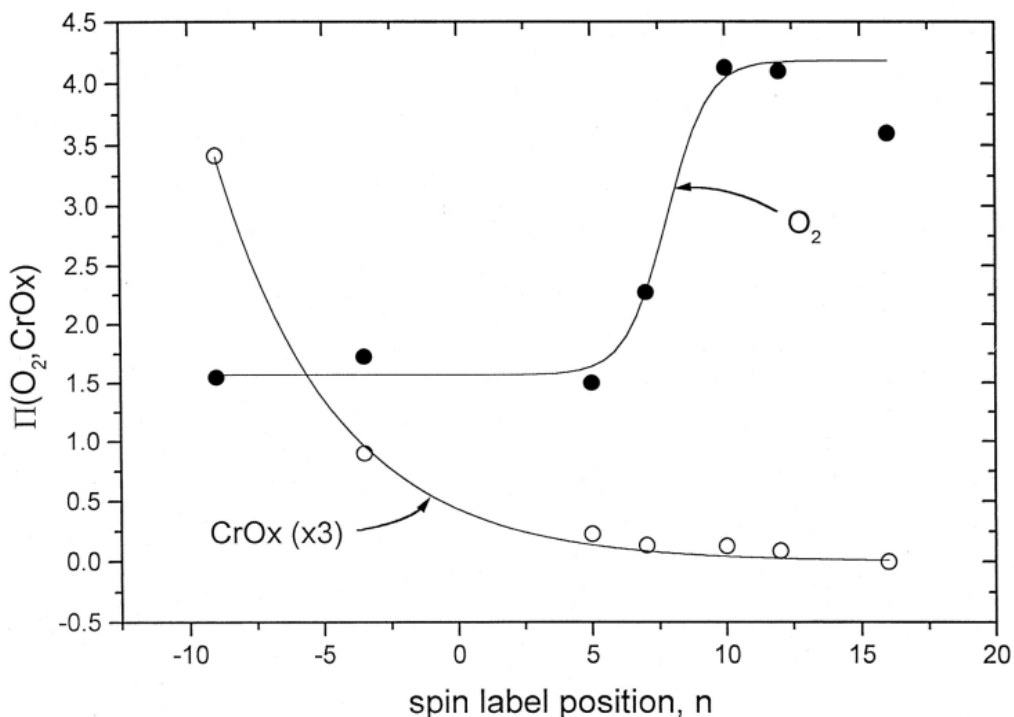


Figure 1.4. Accessibility measurements of hydrophobic oxygen and hydrophilic chromium oxide, paramagnetic complexes, obtained using CW-EPR spectroscopy. (Farahbakhsh, Altenbach, & Hubbell, 1992)

2.2. Electron Spin Echo Envelope Modulation (ESEEM) Spectroscopy

Electron Spin Echo Envelope Modulation abbreviated as ESEEM is a pulsed EPR technique, detecting magnetic nuclei (such as protons, deuterons, nitrogens, etc.) hyperfine-coupled to an unpaired electron. **Figure 1.5A** shows the pulse sequence used in a 3-pulse ESEEM experiment.

In this pulse sequence, three $\pi/2$ pulses are applied to generate a so-called stimulated electron spin echo. In a 3-pulse ESEEM experiment, the position of the first two pulses is fixed (time separation τ), while the time separation between the second and the third $\pi/2$ pulses t_1 is varied. The 3-pulse ESEEM time domain signal is the measured dependence of the electron spin echo intensity (its height) on the incremented time separation t_1 . The final 3-pulse ESEEM spectrum is obtained by Fourier transformation of the measured time domain data.

The energy diagram of spin sublevels of an unpaired electron (electron spin $S=1/2$) magnetically interacting with a nucleus (nuclear spin $I=1/2$) in presence of external magnetic field is shown in **Figure 1.5B**. The external magnetic field splits the two electronic spin sub-states due to the Zeeman interaction. Hyperfine interaction with magnetic nucleus results in additional much smaller splittings (ω_1 and ω_2) of the sub-state corresponding to two different nuclear spin sub-states. For a single electron-nuclear pair, frequency domain ESEEM (Fourier transformed) spectrum consists of two spectral lines positioned at frequencies ω_1 and ω_2 as shown in **Figure 1.5B**. The difference between the two frequencies ω_1 and ω_2 is determined by strength of the electron-nuclear hyperfine interaction and thus, nearly merge into one line for very weakly coupled matrix nuclei. The merged line is positioned exactly at the Larmor frequency of this particular type of nuclei.

In 3-pulse ESEEM, remote water molecules (matrix water) are typically detected through the matrix deuteron peak in lipid membrane samples, where water is exchanged with D₂O.

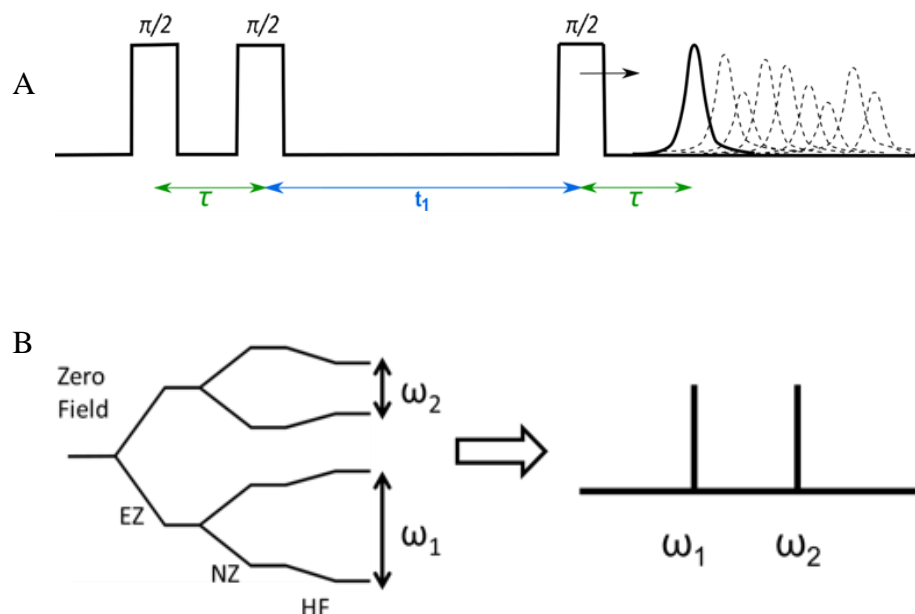


Figure 1.5. (A) Pulse sequence used in a 3-pulse ESEEM experiment. (B) The energy diagram of spin sublevels of an unpaired electron (electron spin $S=1/2$) magnetically interacting with a nucleus (nuclear spin $I=1/2$) in presence of external magnetic field.

Detection of waters coupled to nitroxides by 3-pulse ESEEM gives insufficient spatial resolution due to the long range nature of through-space hyperfine interactions between the electron and matrix nuclei. **Figure 1.6** shows the contribution to the ESEEM signal by matrix deuterons of D₂O as a function of the distance separating the nucleus and unpaired electron (Milov, Samoilova, Shubin, Grishin, & Dzuba, 2008). There is still a measurable contribution to the ESEEM signal from water molecules even at 1.5 nm away from the spin label, which is comparable to the thickness of a monolayer. Combined with a very high water concentration gradient, much of the ESEEM signal might actually originate from the bulk water outside of the membrane.

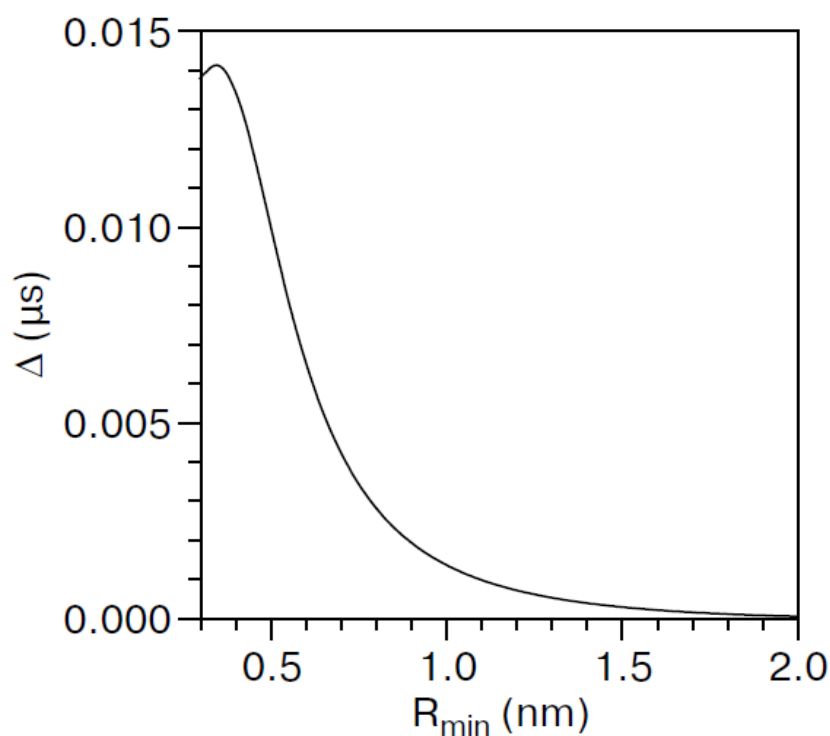


Figure 1.6. Contribution of the ESEEM signal by nuclei as a function of the distance of nuclei from the paramagnetic center. (Milov, Samoiloova, Shubin, Grishin, & Dzuba, 2008)

2.3. Overhauser Dynamic Nuclear Polarization (DNP)

Recently, Overhauser Dynamic Nuclear Polarization (DNP) of bulk water induced by microwave (MW) irradiation of nitroxides has been used to profile water permeation into DOPC lipid bilayers (Segawa, et al., 2016). DNP is based on the transfer of much higher electron spin polarization to much weaker polarized nuclei (~660 times for protons and even larger for other magnetic nuclei). The difference in the polarization is due to the much larger magnetic moment of electrons compared to any of the magnetic nuclei.

Overhauser DNP is determined by the transfer of electron spin polarization to protons of the water molecules located near the electron. This polarization is transferred to other water

molecules and is accumulated as bulk water polarization. The size of the measured polarization depends on many dynamical factors of the DNP process, such as the rate of the polarization transfer from electrons to nuclei, spin relaxation of the electron and protons, diffusion of water molecules from the bulk to locations in the vicinity of the electron, etc.

Figure 1.7 shows water permeation profile in arbitrary units estimated using Overhauser DNP in DOPC lipid bilayer (Segawa, et al., 2016). The profile was obtained as the magnitude of bulk water polarization depending on the position of the spin label in the WALP-23 peptide inserted into the bilayer.

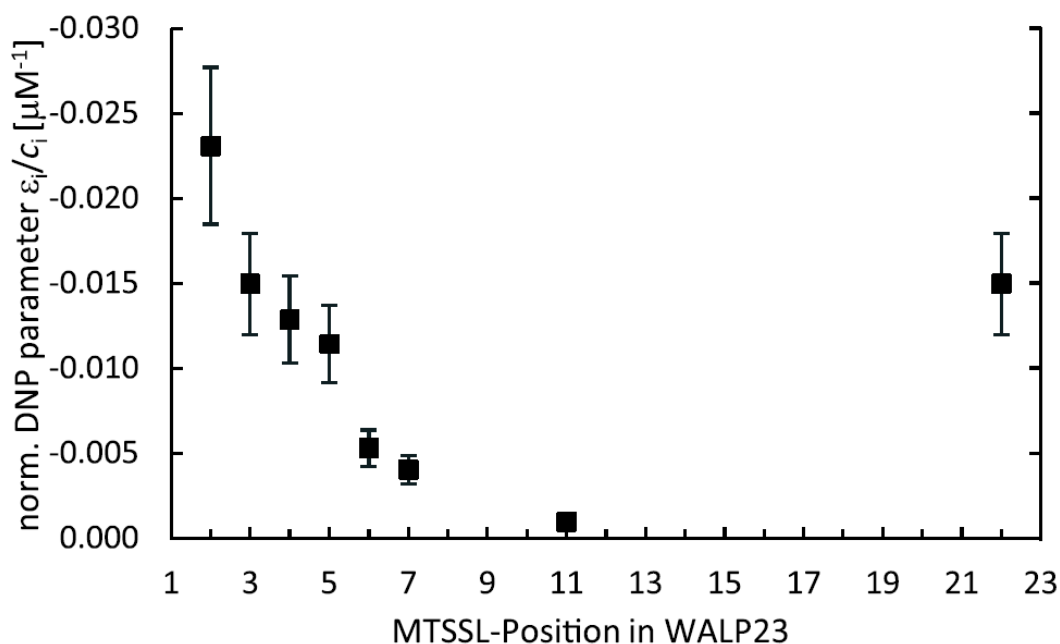


Figure 1.7. Normalized DNP parameter vs. spin label position, obtained by Overhauser DNP of MTSSL-labeled WALP peptide in DOPC bilayers (Segawa, et al., 2016).

While the main advantage of Overhauser DNP is the ability to perform measurements at physiologically relevant temperatures, the extremely high complexity of the DNP phenomenon

determines its major drawback: there is an unclear connection between the local water concentration and observed bulk water polarization. To establish such a connection, a detailed understanding of complex spin dynamics in the lipid bilayers is required, which is practically not feasible at this moment.

Section 3

Proposed Method to Measure Water Concentration in Membranes

3.1. Main idea of proposed method

We propose a novel method for detecting water molecules in the vicinity of EPR spin probes. The main idea of the proposed method is to estimate the local water concentration by measuring the fraction of water (or D₂O) molecules that are reversibly hydrogen- (or deuterium-) bonded to a spin probe. We note here that only water molecules that are within the reaction radius from the nitroxide group (N–O•) will be participating in H-bond formation, and, therefore, are accounted for in our method, and determine its spatial resolution. Although the reported N–O•···H lengths vary significantly (~1.7-3.1 Å) (Chion and Lajzerowiczbonneteau 1980; Plato, Steinhoff et al. 2002; Smirnova, Smirnov et al. 2007), realistically, the proposed method will provide a spatial resolution of ~ 3 Å. An example of hydrogen bonding of water molecules to N–O• moiety of the nitroxide spin probe (Tempo) is shown in **Figure 1.8**.

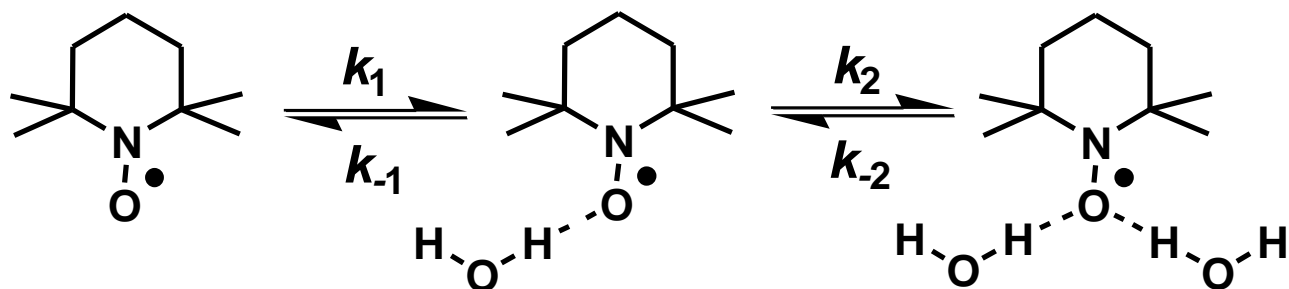
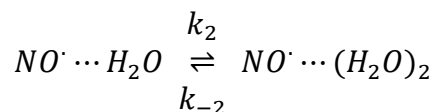
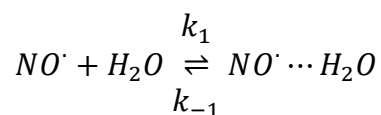


Figure 1.8. Reversible hydrogen bonding interactions between nitroxide (Tempo) and water molecules.

Kinetics of the hydrogen bond formation is similar to that of the protonation of basic functional groups in water. Being a typical bimolecular reaction, the hydrogen bond formation is better described by a second order kinetics. Thus, we can write the following kinetic equations determining the reaction dynamics:



$$0 = \frac{d}{dt}[NO\cdot] = k_{-1}[NO\cdot \cdots H_2O] - k_1[H_2O]_0[NO\cdot] \quad (1)$$

$$0 = \frac{d}{dt}[NO\cdot \cdots H_2O] = k_1[NO\cdot][H_2O]_0 - k_2[NO\cdot \cdots H_2O][H_2O]_0 + k_{-2}[NO\cdot \cdots (H_2O)_2] \quad (2)$$

$$0 = \frac{d}{dt} [NO \cdots (H_2O)_2] = k_2 [NO \cdots H_2O] [H_2O]_0 - k_{-2} [NO \cdots (H_2O)_2] \quad (3)$$

Rearrangement of (1) gives:

$$k_{-1} [NO \cdots H_2O] = k_1 [H_2O]_0 [NO] \quad (A)$$

$$[NO] = \frac{k_{-1} [NO \cdots H_2O]}{k_1 [H_2O]_0} \quad (B)$$

Using (A) to rewrite (2) gives (2a):

$$0 = k_{-1} [NO \cdots H_2O] - k_2 [NO \cdots H_2O] [H_2O]_0 + k_{-2} [NO \cdots (H_2O)_2] \quad (2a)$$

$$[NO] = [NO \cdots (H_2O)_2] + [NO]_0 + [NO \cdots H_2O]$$

Rearranged,

$$[NO \cdots (H_2O)_2] = [NO]_0 - [NO \cdots H_2O] - [NO]$$

Using (B),

$$[NO \cdots (H_2O)_2] = [NO]_0 - [NO \cdots H_2O] - \frac{k_{-1} [NO \cdots H_2O]}{k_1 [H_2O]_0}$$

After factoring out $[NO \cdots H_2O]$,

$$[NO \cdots (H_2O)_2] = [NO]_0 - [NO \cdots H_2O] \left\{ 1 + \frac{k_{-1}}{k_1 [H_2O]_0} \right\} \quad (C)$$

After plugging (C) into (2a),

$$0 = k_{-1} [NO \cdots H_2O] - k_2 [NO \cdots H_2O] [H_2O]_0 + k_{-2} \left\{ [NO]_0 - [NO \cdots H_2O] \left\{ 1 + \frac{k_{-1}}{k_1 [H_2O]_0} \right\} \right\}$$

$$\begin{aligned}
& k_{-1}[NO \cdots H_2O] - k_2[NO \cdots H_2O][H_2O]_0 - k_{-2}[NO \cdots H_2O] \left\{ 1 + \frac{k_{-1}}{k_1[H_2O]_0} \right\} \\
& = -k_{-2}[NO]_0
\end{aligned}$$

$$[NO \cdots H_2O] \left[k_{-1} - k_2[H_2O]_0 - k_{-2} \left\{ 1 + \frac{k_{-1}}{k_1[H_2O]_0} \right\} \right] = -k_{-2}[NO]_0$$

$$[NO \cdots H_2O] = \frac{-k_{-2}[NO]_0}{k_{-1} - k_2[H_2O]_0 - k_{-2} \left\{ 1 + \frac{k_{-1}}{k_1[H_2O]_0} \right\}}$$

$$[NO \cdots H_2O] = \frac{k_{-2}[NO]_0}{k_{-2} \left\{ 1 + \frac{k_{-1}}{k_1[H_2O]_0} \right\} + k_2[H_2O]_0 - k_{-1}}$$

$$[NO \cdots H_2O] = \frac{[NO]_0}{1 + \frac{k_{-1}}{k_1[H_2O]_0} + \frac{k_2[H_2O]_0}{k_{-2}} - \frac{k_{-1}}{k_{-2}}} \quad (\mathbf{D})$$

Plug **(D)** into **(C)** gives

$$[NO \cdots (H_2O)_2] = [NO]_0 - \frac{[NO]_0}{1 + \frac{k_{-1}}{k_1[H_2O]_0} + \frac{k_2[H_2O]_0}{k_{-2}} - \frac{k_{-1}}{k_{-2}}} \left\{ 1 + \frac{k_{-1}}{k_1[H_2O]_0} \right\}$$

$$[NO \cdots (H_2O)_2] = [NO]_0 \left\{ 1 - \frac{\left\{ 1 + \frac{k_{-1}}{k_1[H_2O]_0} \right\}}{1 + \frac{k_{-1}}{k_1[H_2O]_0} + \frac{k_2[H_2O]_0}{k_{-2}} - \frac{k_{-1}}{k_{-2}}} \right\}$$

Let fractions $\mathcal{F}_1 = \frac{[NO \cdots H_2O]}{[NO]_0}$ and $\mathcal{F}_2 = \frac{[NO \cdots (H_2O)_2]}{[NO]_0}$

Then signal obtained by the HYSORE experiment

$$S_{HYSORE} = C_{EXP} \{ \mathcal{F}_1 + 2\mathcal{F}_2 \}$$

where C_{EXP} is a constant characteristic of the HYSCORE experiment.

$$S_{HYSCORE} = C_{EXP} \left\{ \frac{1}{1 + \frac{k_{-1}}{k_1[H_2O]_0} + \frac{k_2[H_2O]_0}{k_{-2}} - \frac{k_{-1}}{k_{-2}}} + 2 \left\{ 1 - \frac{\left\{ 1 + \frac{k_{-1}}{k_1[H_2O]_0} \right\}}{1 + \frac{k_{-1}}{k_1[H_2O]_0} + \frac{k_2[H_2O]_0}{k_{-2}} - \frac{k_{-1}}{k_{-2}}} \right\} \right\}$$

$$S_{HYSCORE} = C_{EXP} \left\{ 2 + \frac{1 - 2 \left\{ 1 + \frac{k_{-1}}{k_1[H_2O]_0} \right\}}{1 + \frac{k_{-1}}{k_1[H_2O]_0} + \frac{k_2[H_2O]_0}{k_{-2}} - \frac{k_{-1}}{k_{-2}}} \right\}$$

$$S_{HYSCORE} = C_1 \left\{ 2 - \frac{[H_2O]_0 + 2C_2}{[H_2O]_0 + C_2 + \frac{1}{C_3} [H_2O]_0^2 - C_4 [H_2O]_0} \right\} \quad \text{Equation 1}$$

$$\text{Where } C_1 = C_{EXP}, C_2 = \frac{k_{-1}}{k_1}, C_3 = \frac{k_{-2}}{k_2}, \text{ and } C_4 = \frac{k_{-1}}{k_2}$$

Thus, by knowing K_d and measuring \mathcal{F}_{H-bond} one can obtain an estimate of water concentration $[H_2O]_0$.

3.2. HYSCORE Spectroscopy as the optimal method to measure \mathcal{F}_{H-bond}

Binding of a water molecule to a nitroxide spin label can be detected using EPR spectroscopy in two ways: (i) indirectly, by observing the change of magnetic parameters of

nitroxide label and (ii) directly, through magnetic interaction of the water H-bonded proton (deuteron) with the unpaired electron of the nitroxide (hyperfine interaction).

Indirect detection of the H-bonded water to nitroxides has been extensively explored by Derek Marsh (Marsh, 2001). He used the subtle change of the isotropic component of hyperfine coupling between unpaired electron and nitrogen nucleus of the N–O• group, A_{iso}^N . At room temperature in low viscosity liquid solutions of nitroxides, all anisotropic magnetic interactions are averaged out by fast tumbling of nitroxide molecules (fast motion regime). This results in a continuous wave (CW) EPR spectrum consisting of three very narrow lines from the nitroxide, allowing highly accurate determination of A_{iso}^N . In real biological systems, however, steric factors, as well as large size of the biomolecules, often slow down nitroxide motion dynamics to the level when magnetic anisotropies are only partially averaged out. In this case, accurate determination of A_{iso}^N is practically unfeasible, and this is the major drawback of the indirect detection of the H-bonded water molecule. An additional problem of the method proposed by Marsh is the dependence of A_{iso}^N on the local dielectric properties of the medium, which are often unknown in highly complex, heterogeneous biological systems.

As mentioned above, the direct detection of the H-bonded water relies on detection of the hyperfine coupling of the proton (deuteron) directly bound to the oxygen atom of the N–O• group. This hyperfine interaction is nearly anisotropic in nature, and is determined by the hyperfine tensor $A_{H-bond}=[4.69, 10.42, -11.20]$ MHz (Smirnova, Smirnov, Pachtchenko, & Poluektov, 2007). Such highly anisotropic interactions can only be measured if molecular motion is prohibited, requiring a frozen sample. A_{H-bond} is too narrow to be detected by CW-EPR spectroscopy, since its magnitude is smaller than typical unresolved magnetic field inhomogeneity across the sample (multiple unresolved hyperfine interactions, g-strain, hyperfine strains etc.).

In pulsed EPR spectroscopy, the local field inhomogeneity is resolved in the so-called spin echo phenomenon (field inhomogeneity is refocused in the electron spin echo). Thus, pulsed EPR spectroscopy is mandatory in order to measure A_{H-bond} and enable direct detection of the H-bonded water molecule.

There are several pulsed EPR methods capable of detection of such weak hyperfine interactions: (i) Electron-Nuclear Double Resonance (ENDOR) Spectroscopy; (ii) Electron Spin Echo Envelop Modulation (ESEEM) Spectroscopy; (iii) Electron-Electron Double Resonance-(ELDOR)-Detected NMR Spectroscopy; (iv) Hyperfine Sublevel Correlation (HYSCORE) Spectroscopy.

While all the above pulsed EPR methods have been designed to measure weak hyperfine interactions in frozen samples, their practical application is often hampered by complex overlap of spectral lines from different molecular orientations, and more importantly, from different nuclei usually abundantly present in the system. The problem is usually circumvented by isotope labeling of the magnetic nucleus of interest. HYSCORE spectroscopy dramatically enhances resolving power of the pulse methods with respect to multiple overlapping components by expanding the detection space into a second dimension.

3.3. Basic Principles of HYSCORE Spectroscopy

As previously mentioned, Hyperfine Sublevel Correlation (HYSCORE) Spectroscopy is a 2-dimensional pulsed EPR technique. HYSCORE measures weak magnetic interactions between an unpaired electron and surrounding nuclei.

A pulse sequence for a HYSCORE experiment is shown in **Figure 1.9**. The pulse sequence consists of a total of four microwave pulses. Three $\pi/2$ pulses are used to create so called

stimulated electron spin echo. Another π pulse is applied between the second and the third $\pi/2$ pulses. In this pulse sequence, time separation τ between the first two pulses is fixed during the experiment. The time t_1 (between the second $\pi/2$ and the π pulse) is discretely varied in one dimension, and the time t_2 (between the π and third $\pi/2$ pulse) is discretely varied in a second dimension. The signal is recorded as the intensity (height) of the electron spin echo as a 2-dimensional (2D) function of these inter-pulse separations. The measured time domain signal is then Fourier transformed to obtain HYSORE spectrum in 2D frequency domain.

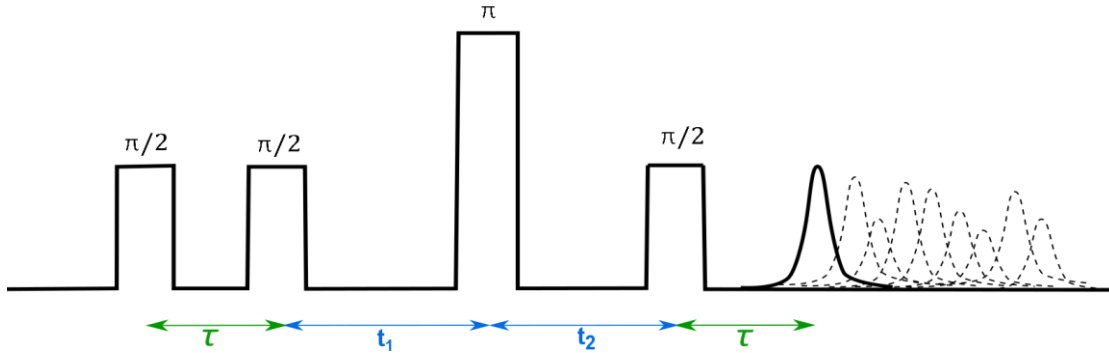


Figure 1.9. Typical 4-pulse sequence of a HYSORE Experiment.

The nuclear hyperfine splittings caused by electron-nuclear hyperfine interaction shown in **Figure 1.10** (see also **Figure 1.5B**) are measured in the form of 2D cross-correlation plots. The 2D frequency domain coordinates of the two detected off-diagonal cross-correlation peaks are given by $[\omega_1, \omega_2]$ and $[\omega_2, \omega_1]$ respectively.

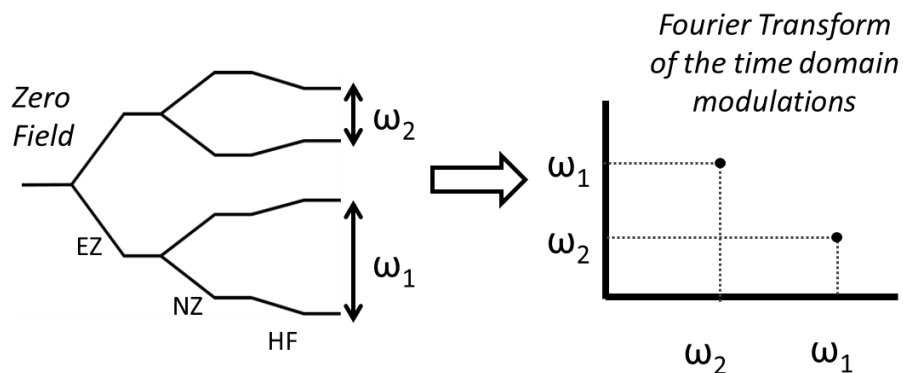


Figure 1.10. Hyperfine splittings measured by HYSCORE Spectroscopy and corresponding cross-correlation peaks.

An example of a HYSCORE spectrum of TEMPOL radical in frozen deuterium oxide and glycerol and the corresponding skyline projection are shown in **Figure 1.11**. Different types of nuclei are well-resolved. The H-bonded D₂O is well resolved from signals arising from matrix (glycerol) protons and protons on the nitroxide molecule. The pulse positions in the experiment were chosen such that contribution of the matrix water deuterons is suppressed through the so called blind-spot effect of HYSCORE spectroscopy (Schweiger & Jeschke, 2001).

The fraction of nitroxides bonded to D₂O molecules, \mathcal{F}_{H-bond} , was measured in lipid bilayers hydrated with deuterated water. \mathcal{F}_{H-bond} is proportional to the height of the detected signal, H_D , corresponding to the bonded deuterons. The superior sensitivity of HYSCORE allows us to detect very small fractions of bonded nitroxide radicals even in the most hydrophobic region of the membrane.

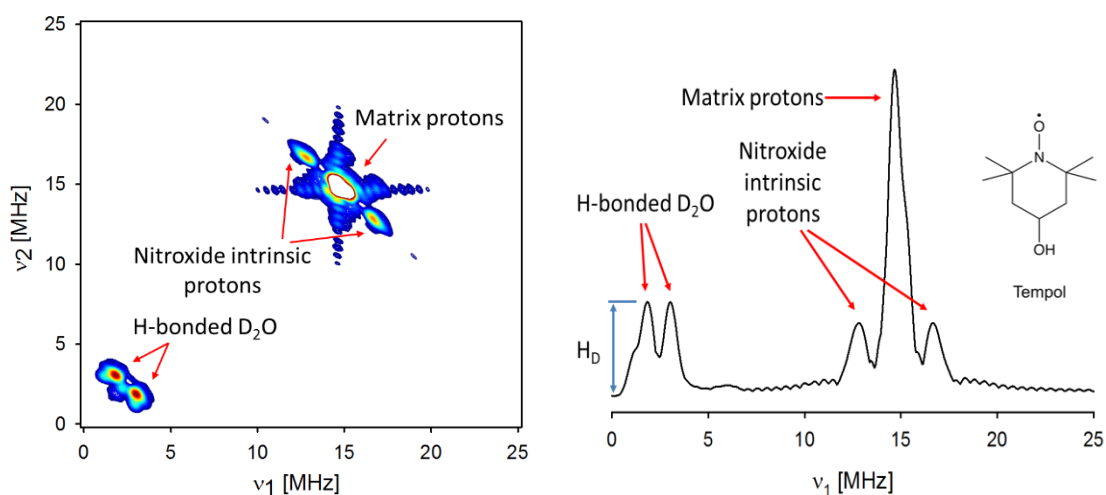


Figure 1.11. HYSORE Spectrum of TEMPOL spin probe in frozen D₂O/glycerol solution and its corresponding Skyline Projection. High resolution of HYSORE enables the selective detection of bonded water molecule(s) with very high sensitivity (small fractions, f_{H-Bond}).

3.4. Relation between the HYSORE signal and \mathcal{F}_{H-bond}

For the case of a single interacting nucleus of $I=1/2$ and under the assumption of ideal microwave pulses (pulses with infinitely short duration and infinitely broad excitation bandwidth), the HYSORE signal in the time domain can be expressed analytically (Schweiger & Jeschke, 2001). Even using the ideal pulse assumption, the expression of the HYSORE signal is complex to be shown here. In reality, the effects of non-ideal microwave pulses are significant. In any case, the relative modulation depth (i.e., the ratio of the modulated signal to the intensity of electron spin echo) depends only on parameters of the spin system and experimental imperfections. Assuming that, for all samples, experimental imperfections could be well reproduced, the intensity of the measured HYSORE signal can be expressed as following:

$$S_{HYSORE} = C_{Exp}^{HYSORE} N_{NO} \cdot \mathcal{F}_{H-bond}$$

Where $C_{Exp}^{HYSCORE}$ is an experimental constant representing the measured HYSCORE signal intensity per one H-bonded nitroxide radical, and N_{NO} is the total number of nitroxides in the sample. $C_{Exp}^{HYSCORE}$ depends on many parameters, such as hyperfine interaction of the bonded proton (deuteron), relaxation times of the radicals, pulse imperfections etc.

Dependence of the measured HYSCORE signal on the total number of nitroxides represents an uncertainty (number of spins will vary from sample to sample) that has to be removed for our purposes of analytically measuring \mathcal{F}_{H-bond} for many samples. This can be done dividing the measured HYSCORE signal by the intensity of the electron spin echo itself, which is proportional to the number of spins in the sample. The intensity of the electron spin echo is given by following:

$$S_{Echo} = C_{Exp}^{Echo} N_{NO}$$

Thus, normalizing the HYSCORE signal by the echo intensity would provide the normalized HYSCORE signal:

$$S_{HYSCORE}^{Norm} = C_{Exp} \mathcal{F}_{H-bond}$$

$$\text{Where } C_{Exp} = C_{Exp}^{HYSCORE} / C_{Exp}^{Echo}.$$

While there are multiple possible ways the measured HYSCORE signal can be normalized by its echo intensity, the normalization of the HYSCORE signal by its echo intensity in this work was determined as follows. First, the HYSCORE signal was measured and processed for a particular sample. Then, the π pulse (the 3rd, inverting pulse) was removed from the pulse sequence, and the echo intensity was measured as the function of t_2 , the time separation between

the second and the third pulses (Refer to **Figure 1.9**). This measured time domain signal corresponds to a 3-pulse ESEEM signal, and therefore may contain unwanted nuclear modulations. To remove the modulations, this signal has been fitted by a stretched exponential function to yield “pure” echo decay signal. Finally, the 4-pulse HYSCORE signal with time domain coordinates t_1 and t_2 has been divided by the corresponding numerically obtained “pure” echo decay signal with time coordinate of $t=t_1+t_2$ which corresponds to the identical positions of three $\pi/2$ -pulses.

In practice, the unknown parameter C_{Exp} , could be easily determined from the hydrogen bond donor concentration dependence of the normalized HYSCORE signal, since C_{Exp} represents the asymptotic maximum of the processed and normalized HYSCORE signal (in some experimental units) upon \mathcal{F}_{H-bond} approaching its maximum value of 1.

3.5. Use of alcohol-toluene model system to estimate experimental and kinetic parameters

To estimate the entire set of unknown parameters in **Equation 1** (see Section 3.1: Main Idea of Proposed Method) required to establish a quantitative connection between the measured bonded D₂O signal and the local water concentration, two model systems were used. The model systems consisted of a) methanol-toluene and b) ethanol-toluene solvent mixtures with a small amount of spin probe (2mM of TEMPO).

These two short-chain alcohols were chosen to mimic the hydrogen (deuterium) bonding behavior of water (D₂O) because of the following reasons: a) both methanol and ethanol are polar, bond forming solvents with dielectric and bonding properties as close as possible to those of water; b) both are well-miscible with some of the non-polar, glass forming solvents, in a wide range of concentrations, which is required to estimate H-bonding equilibrium constant for the membrane system; c) their molecular sizes, although somewhat bigger, are comparable to water, minimizing the effects caused by differences in steric factors. Toluene was chosen to mimic the local hydrophobic interior of the membrane due to its polarity that is close to that of the hydrocarbon environment, as well as excellent miscibility with ethanol.

Section 4

Experimental Methods

4.1. Sample Preparation

4.1.1. POPG Bilayers Doped with Doxyl Stearic Acids

POPG (1-palmitoyl-2-oleoyl-sn-glycero-3-phospho-(1'-rac-glycerol)) was purchased from Avanti Polar Lipids, Inc. (Alabaster, Alabama).

Samples were prepared by mixing the 5- or 16-doxyl stearic acids (DSA) and POPG phospholipid chloroform stock solution to give 2 (mol)% DSA and 15 weight % lipids. Solvent was removed by a stream of nitrogen gas, followed by lyophilization for at least 24 hours. The lipid samples were rehydrated with D₂O containing 20 mM NaCl. Ten freeze-thaw cycles were carried out before using samples for pulsed EPR experiments.

4.1.2. DOPC Bilayers Doped with WALP-n-MTSL

WALP peptides with single cysteine mutations were purchased from RS Synthesis (Louisville, KY) or Peptide 2.0 (Chantilly, VA) (refer to **Table 1.1** for corresponding peptide sequences). The position (n) corresponds to the cysteine residue position.

Table 1.1. Sequences of WALP23 peptides with single cysteine mutations of the nth residue position.

Company	Position (n)	Peptide Sequence
Peptide 2.0	-2	Ac- C AAGWWLALALALALALALALALWWA-NH2
Peptide 2.0	0	Ac- C GWWLALALALALALALALALWWA-NH2
RS Synthesis	1	Ac- C WWLALALALALALALALALWWA-NH2
RS Synthesis	3	Ac-GW C LALALALALALALALALWWA-NH2
RS Synthesis	6	Ac-GWWL C ALALALALALALALWWA-NH2
Peptide 2.0	10	Ac-GWWLALAL C ALALALALALWWA-NH2
Peptide 2.0	11	Ac-GWWLALALAL C LALALALALWWA-NH2
RS Synthesis	12	Ac-GWWLALALAL C ALALALALWWA-NH
RS Synthesis	14	Ac-GWWLALALALAL C ALALALWWA-NH2
RS Synthesis	16	Ac-GWWLALALALALAL C ALALWWA-NH2
RS Synthesis	18	Ac-GWWLALALALALALAL C ALWWA-NH2
RS Synthesis	21	Ac-GWWLALALALALALALALAL C WA-NH2
RS Synthesis	23	Ac-GWWLALALALALALALALALWW C -NH2

DOPC (1,2-dioleoyl-sn-glycero-3-phosphocholine) was purchased from Avanti Polar Lipids, Inc. (Alabaster, Alabama). MTSL (1-Oxyl-2,2,5,5-tetramethylpyrroline-3- methyl)-methanethiosulfonate) was generously provided by Dr. Maxim A. Voynov, NCSU.

Spin labeling reaction (shown in **Figure 1.12**) and HPLC purification was done according to Robinson et al. (Nielsen, Che, Gelb, & Robinson, 2004).

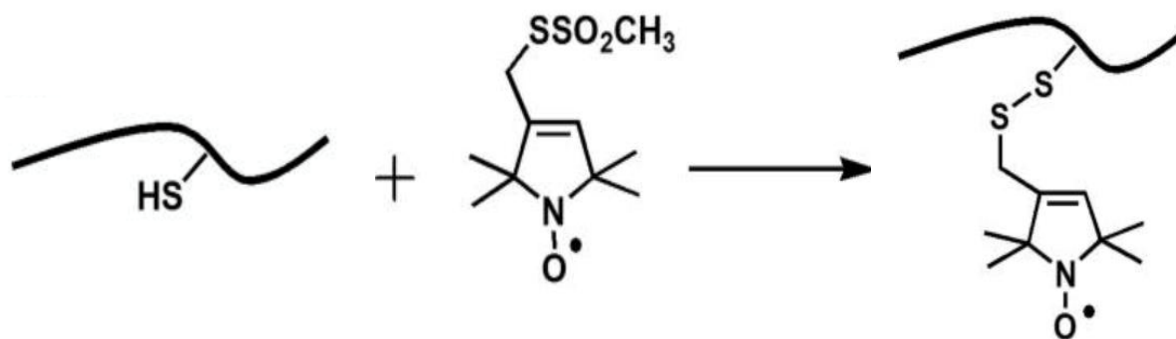


Figure 1.12. Spin labeling reaction of the sulfhydryl group of a cysteine residue with the spin label 1-oxyl-2,2,5,5-tetramethylpyrroline-3-methyl)-methanethiosulfonate (MTSL), producing a nitroxide side chain. (Smirnova & Smirnov, 2015)

EPR samples were prepared by mixing the TFE stock solution of peptide and phospholipid chloroform stock solution to give a peptide to phospholipid ratio of 1:400. Solvent was removed by a stream of nitrogen gas, followed by lyophilization for at least 24 hours. The lipid samples were rehydrated with D₂O containing 20 mM NaCl to give 15 weight % lipids. Ten freeze-thaw cycles were carried out before using samples for pulsed EPR experiments.

4.2. EPR spectroscopy

CW-EPR spectra were measured at X-band (9.7 GHz) using Bruker ELEXSYS E500, equipped with Super-High-Q ER4122SHQE resonator. All measurements were taken at room temperature using 0.5 G modulation amplitude and 2 mW microwave power.

ESEEM and HYSCORE spectra were measured at X-band (9.7 GHz) using a Bruker ELEXSYS E580 spectrometer equipped with a 1 kW TWT amplifier (all from Bruker Biospin, Billerica, MA, USA). All pulsed EPR experiments were carried out at 76 K using a Bruker ER 4118CF flow cryostat cooled by liquid nitrogen. The microwave frequency was set to 9.659 GHz.

The length of the $\pi/2$ pulses was 8 ns for both ESEEM and HYSCORE experiments; the length of the π pulse used for HYSCORE experiments was 16 ns. ESEEM and HYSCORE signals were acquired at a static magnetic field of 3440.6 G, corresponding to the maximum of the frozen nitroxide echo height. For all samples, microwave power, acquisition trigger length, and acquisition trigger position were kept constant.

4.3. Results and Discussion

4.3.1. Model system to mimic nonpolar region of hydrated lipid bilayer

As mentioned earlier, we used short-chain alcohols (methanol and ethanol) as models to estimate the set of unknown experimental and kinetic parameters of **Equation 1** (see Section 3.1: Main Idea of Proposed Method) in order to establish a quantitative connection between the measured H-bonded D₂O signal and the local water concentration.

In order to test if H-bonds formed between alcohols and N–O• group of nitroxide have similar properties for both alcohols and water, the HYSCORE spectra of H-bonded deuterated water and several deuterated alcohols were measured. The spectral features of the detected H-bonded deuteron are determined by deuteron hyperfine coupling constant A_D , which in turn is determined by the distance between the deuteron and unpaired electron localized on the N–O• group. The H-bonding distance is a sensitive measure of the strength of the H-bond, as stronger H-bonding is correlated with a shorter bond length, and vice versa. As can be seen from **Figure 1.13**, spectral features of H-bonded water and all alcohols are nearly identical, confirming that the nature of the H-bond to nitroxides is very similar in all these solvents.

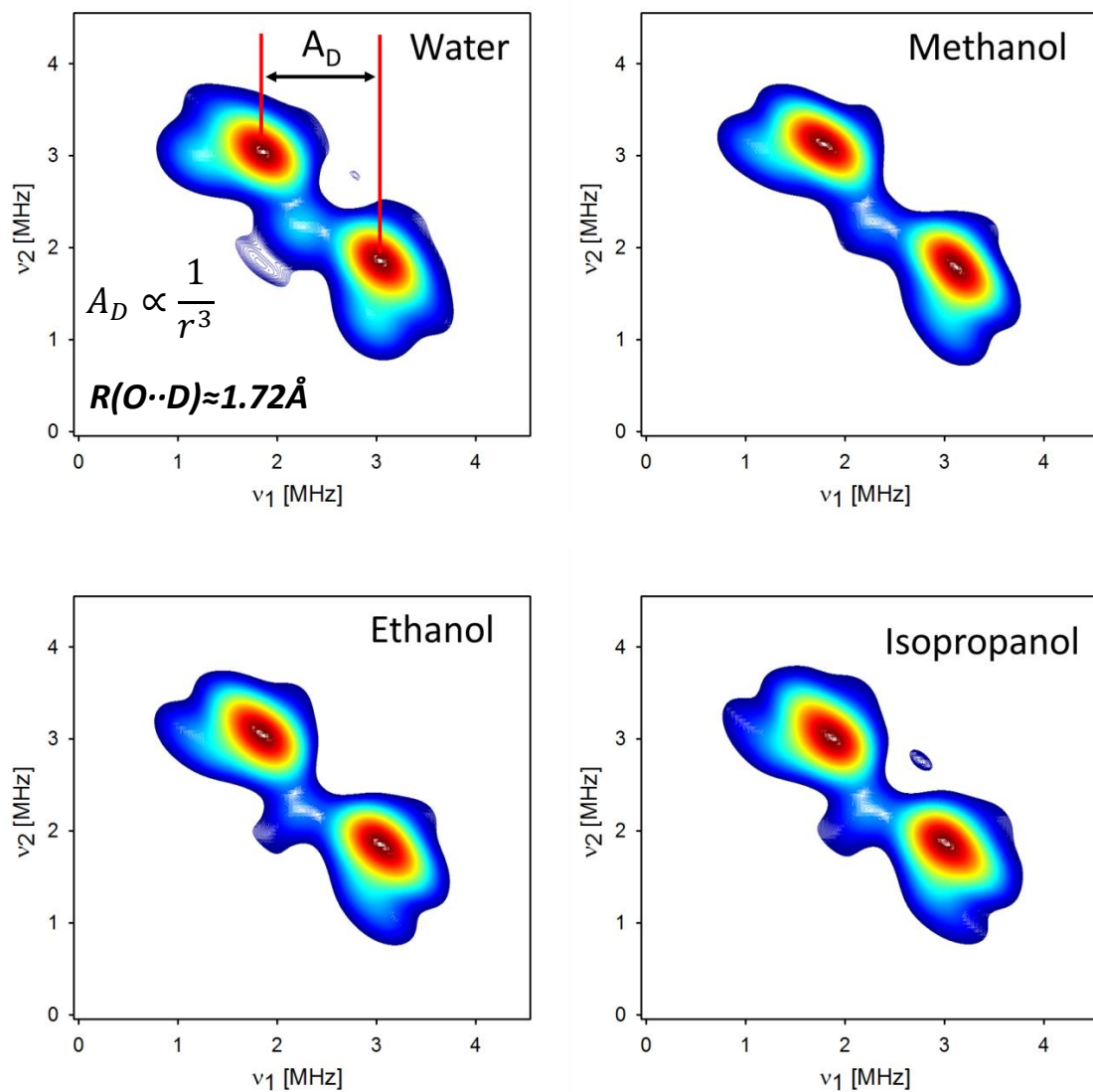


Figure 1.13. Frozen glass ^2H -HYSCORE spectra of TEMPOL spin probes in D_2O (50% vol. mixture with diglyme), CH_3OD , $\text{CH}_3\text{CH}_2\text{OD}$ and $\text{CH}_3\text{CHODCH}_3$.

The observed hyperfine coupling constant A_D closely matches those measured for several different alcohols using ENDOR spectroscopy (Smirnova, Smirnov, Pachtchenko, & Poluektov, 2007). As it was determined by Smirnova et al, the observed hyperfine coupling constant

corresponds to the distance between the H-bonded deuteron and N–O• oxygen of $R_{O...D} = 1.74 \pm 0.06 \text{ \AA}$.

To test if the H-bonding kinetics would be similar for waters and alcohols, we used diglyme as a host solvent and TEMPOL as a spin probe, due to its excellent solubility in water. Diglyme is a glass-forming solvent, well miscible with water, alcohols and the nitroxide radical. Although diglyme is not an ideal mimic for the hydrophobic region of the membrane, as it is relatively polar and competes with the nitroxide as H-bond acceptor, this solvent presents an acceptable compromise as a glass-forming host for comparing binding and kinetic properties of water and alcohols.

Figure 1.14 shows the fraction of H-bonded nitroxides measured as the $S_{HYSCORE}^{Norm}$ signal (H_D signal normalized by the electron spin echo amplitude) for deuterated water and several deuterated alcohols in diglyme. Within relatively small deviations, the measured fractions of H-bonded nitroxides show the same dependence on H-bond donor concentration. This in turn indicates that the kinetic properties of water and alcohols are similar with respect to the H-bond formation with N–O• group of nitroxides.

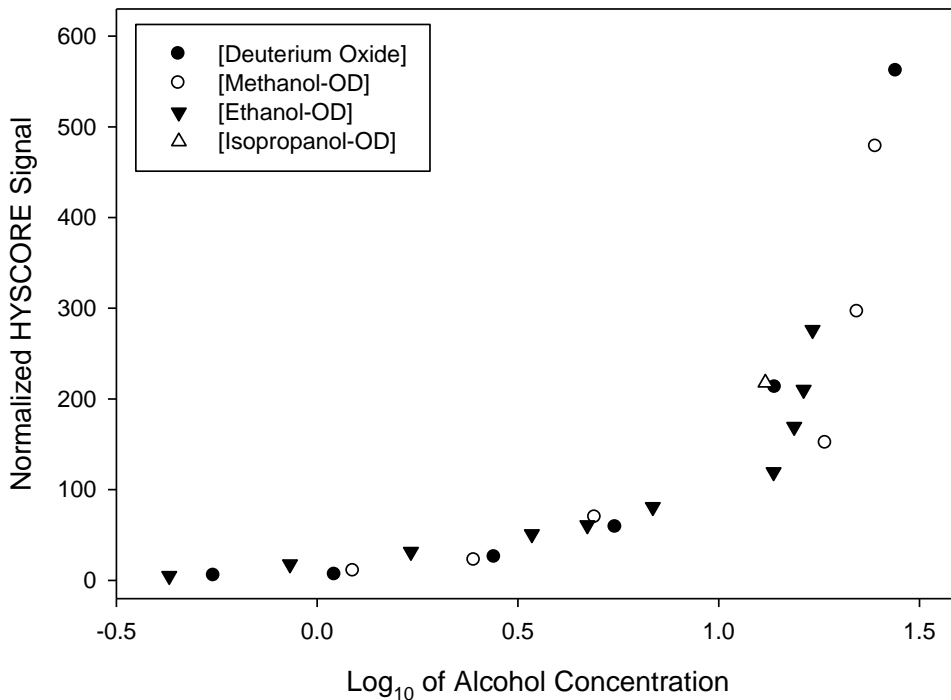


Figure 1.14. Normalized HYSCORE signal intensity of the hydrogen bonded deuteron for frozen glasses of partially deuterated water and three alcohols in diglyme using TEMPOL.

4.3.2. Estimation of equilibrium constants by HYSCORE \mathcal{F}_{H-bond} measurements

Once we determined that short-chain alcohols, namely methanol and ethanol, are reasonably good mimics of water in terms of H-bonding strength and binding kinetics, the set of unknown parameters, namely the experimental parameter C_{EXP} as well as three kinetic parameters:

$C_2 = \frac{k_{-1}}{k_1}$, $C_3 = \frac{k_{-2}}{k_2}$, and $C_4 = \frac{k_{-1}}{k_2}$ from **Equation 1** has been estimated for both methanol and

ethanol in toluene. This was accomplished by fitting the measured $S_{HYSCORE}^{Norm}$ signal proportional to the fraction \mathcal{F}_{H-bond} vs. logarithm of H-bond donor molar concentration by the following equation as described above:

$$S_{HYSCORE} = C_1 \left\{ 2 - \frac{[H_2O]_0 + 2C_2}{[H_2O]_0 + C_2 + \frac{1}{C_3}[H_2O]_0^2 - C_4[H_2O]_0} \right\} \quad \text{Equation 1}$$

The experimentally measured values of $S_{HYSCORE}$ vs hydrogen bond donor concentrations superimposed with the simulated curve corresponding to the fit parameters are shown in **Figure 1.15** and **Figure 1.16** for methanol and ethanol, respectively.

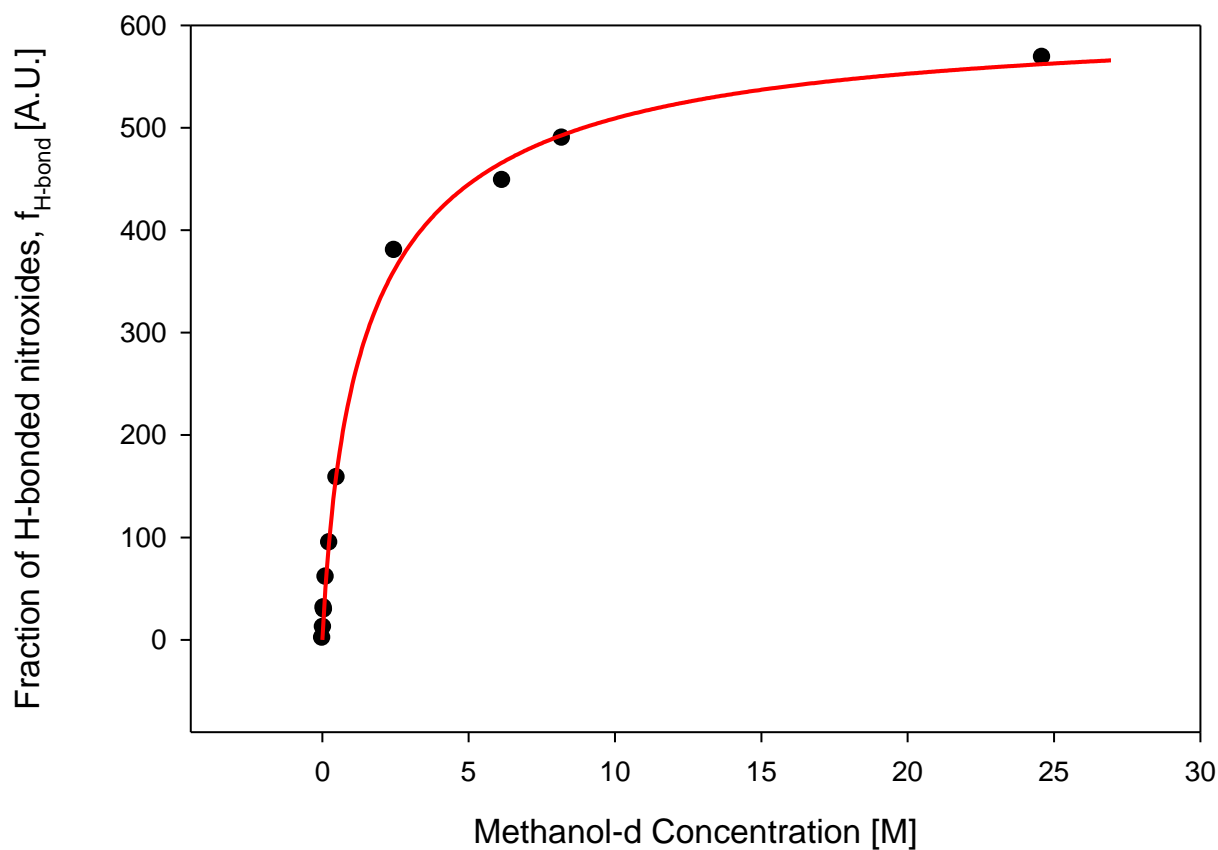


Figure 1.15. Normalized HYSCORE signal intensity of the hydrogen bonded deuteron (H_D/A_{Echo}) to TEMPO for frozen CH_3OD in toluene.

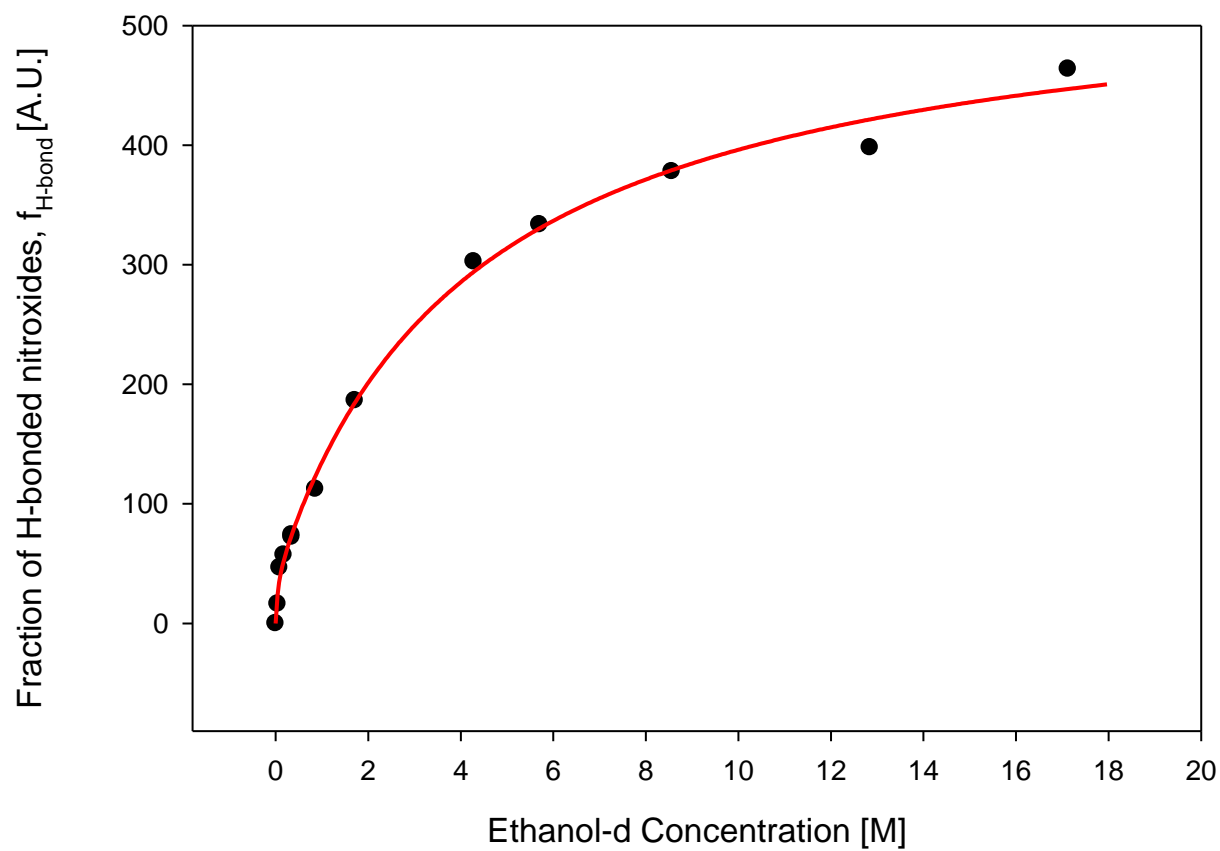


Figure 1.16. Normalized HYSORE signal intensity of the hydrogen bonded deuteron (H_D/A_{Echo}) for frozen $\text{CH}_3\text{CH}_2\text{OD}$ in toluene using TEMPO.

Corresponding sets of the obtained parameters, together with the estimates of their 95% confidence bounds, are given in **Table 2**.

Table 1.2. Experimental and kinetic parameters obtained by least square minimization procedure. In the parenthesis are the 95% confidence bounds.

	C_{EXP} [A.U.]	C_2 [M]	C_3 [M ⁻¹]	C_4
Methanol-d in Toluene	304 (284, 325)	0.51 (0.41, 0.62)	4.2 (2.3, 6.1)	0.05 (fixed at bound)
Ethanol-d in Toluene	274 (247, 302)	0.022 (0, 0.099)	7.9 (5.1, 10.8)	0.46 (0.40, 0.51)

While the size of the experimental parameter C_{EXP} is similar for both methanol-d and ethanol-d (corresponding 95% confidence intervals strongly overlap), the differences in the kinetic parameters C_2 , C_3 and C_4 are evident. Even based on a quick visual inspection of **Figure 1.15** and **Figure 1.16**, one may conclude that binding kinetics of ethanol-d is somewhat slower as compared to methanol-d and chemical equilibrium is clearly shifted towards higher concentrations. This is well in line with a somewhat larger size and thus larger hydrodynamic radius of ethanol-d molecule, as compared to methanol-d, slowing down its rate of diffusion. The size of a water (D₂O) molecule is even smaller than that of methanol-d molecule. Moreover, due to the symmetry, water has two hydrogen bond donor groups versus one in alcohols. Both these factors should accelerate rates of hydrogen bond formation, and therefore, shift the equilibrium towards even lower concentrations. Thus, while short-chain alcohols may provide reasonably good estimates, the real water concentration would probably be somewhat lower than such estimates.

4.3.3. Comparison with the CW EPR spectroscopy at room temperature

For comparison, measurements of isotropic component of the nitrogen hyperfine coupling constant of Tempo, A_{iso}^N , has been performed at room temperature for wide range of methanol and ethanol concentration in toluene using CW-EPR spectroscopy. Additionally, protonated as well as selectively deuterated forms of two alcohols have been used in order to test a potential isotope effect on kinetic equilibrium. The measured dependencies of A_{iso}^N of Tempo radical on alcohol concentrations are shown in **Figure 1.17**.

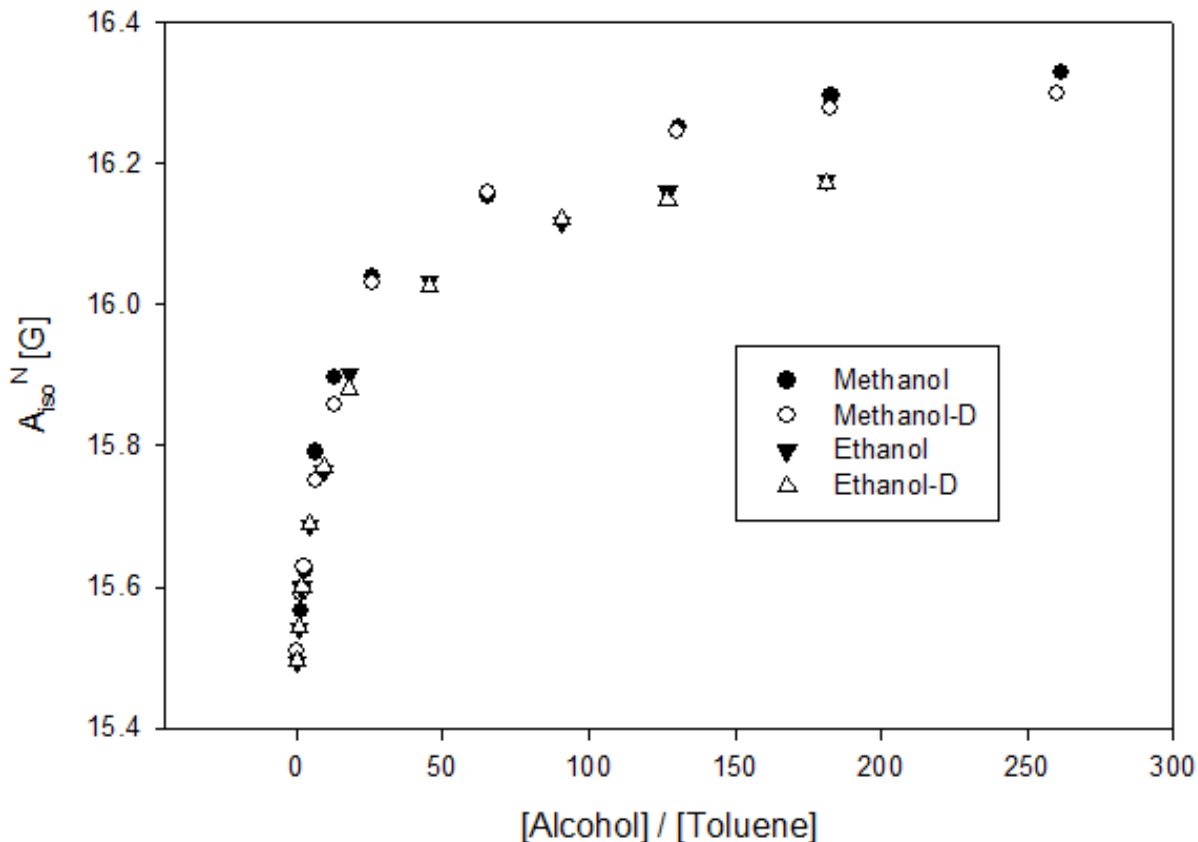


Figure 1.17. Isotropic nitrogen hyperfine coupling constants obtained for 20 μ M Tempo in alcohol-toluene mixtures for both protonated and selectively deuterated methanol and ethanol.

Interestingly, while the magnitude of the A_{iso}^N is somewhat higher in methanol vs ethanol, the dependencies of the normalized change of A_{iso}^N (shown in **Figure 1.18**) are nearly identical in methanol and ethanol, indicating close similarity of the hydrogen binding kinetics. This behavior is different than what is observed by HYSORE for the frozen solutions, where chemical equilibrium is shifted towards the range of higher concentrations for ethanol due to its larger molecular size. Unfortunately, as discussed above (see Section 2), the observed hyperfine coupling is determined by both polarity as well as proticity of the solvent. These two contributions are hard to separate, since the local dielectric properties of the solvent mixture around a spin probe are altered in highly complex manner upon alcohol concentration variation.

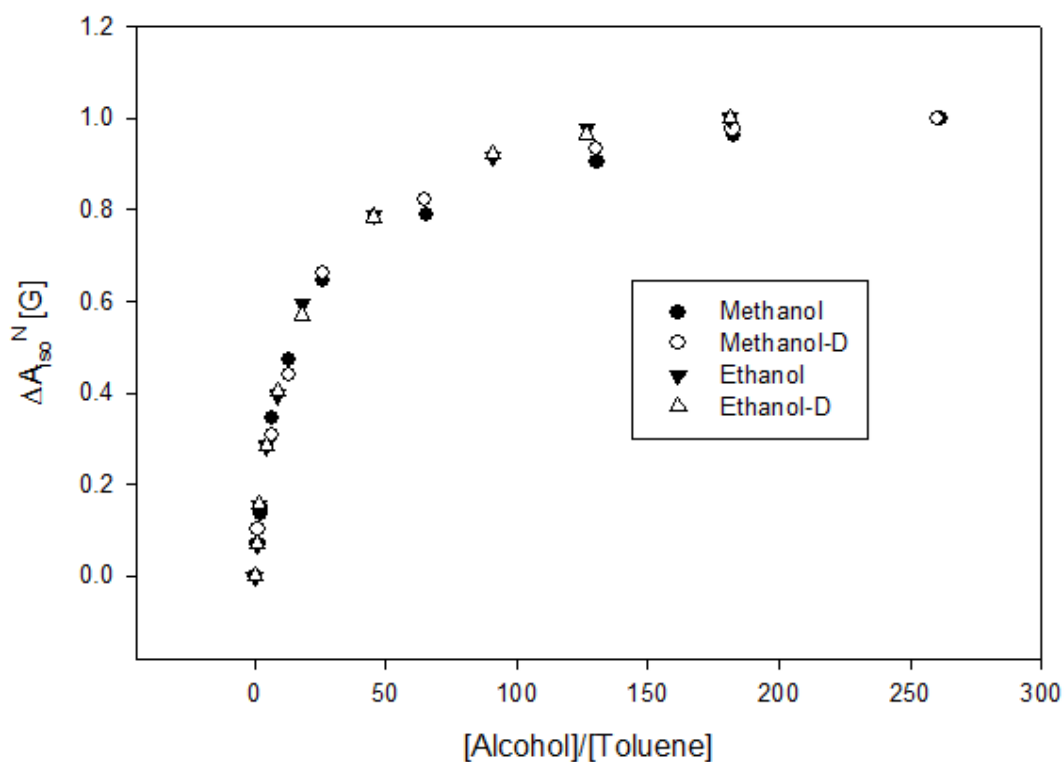


Figure 1.18. Normalized change of the isotropic nitrogen hyperfine coupling constants obtained for 20 μ M Tempo in alcohol-toluene mixtures for both protonated and selectively deuterated methanol and ethanol.

4.3.4. Water Concentration Measurements

4.3.4.1. POPG bilayers doped with doxyl stearic acids

Here, we demonstrate the viability of the method on the example of POPG lipid bilayers doped with doxyl stearic acid, a nitroxide spin probe. HYSCORE spectra of 5-DSA and 16-DSA in POPG liposomes, along with the chemical structures of the corresponding nitroxides, are shown in **Figures 1.19** and **1.20**, respectively.

For 5-DSA (in which the spin probe is located closer to the membrane surface), water concentration was found to be 0.85(vol)% and 2.4(vol)% using methanol-toluene and ethanol-toluene ruler, respectively, whereas for 16-DSA (in which the spin probe is close to the middle of the membrane), measured water concentration dropped to 0.41(vol)% and 0.91(vol)% using methanol-toluene and ethanol-toluene ruler, respectively. These values were obtained using the \mathcal{F}_{H-bond} measurements for each respective lipid sample and its comparison with those obtained from HYSCORE measurements of Tempo in glassy alcohol-toluene model systems (see **Figure 1.15** and **Figure 1.16**).

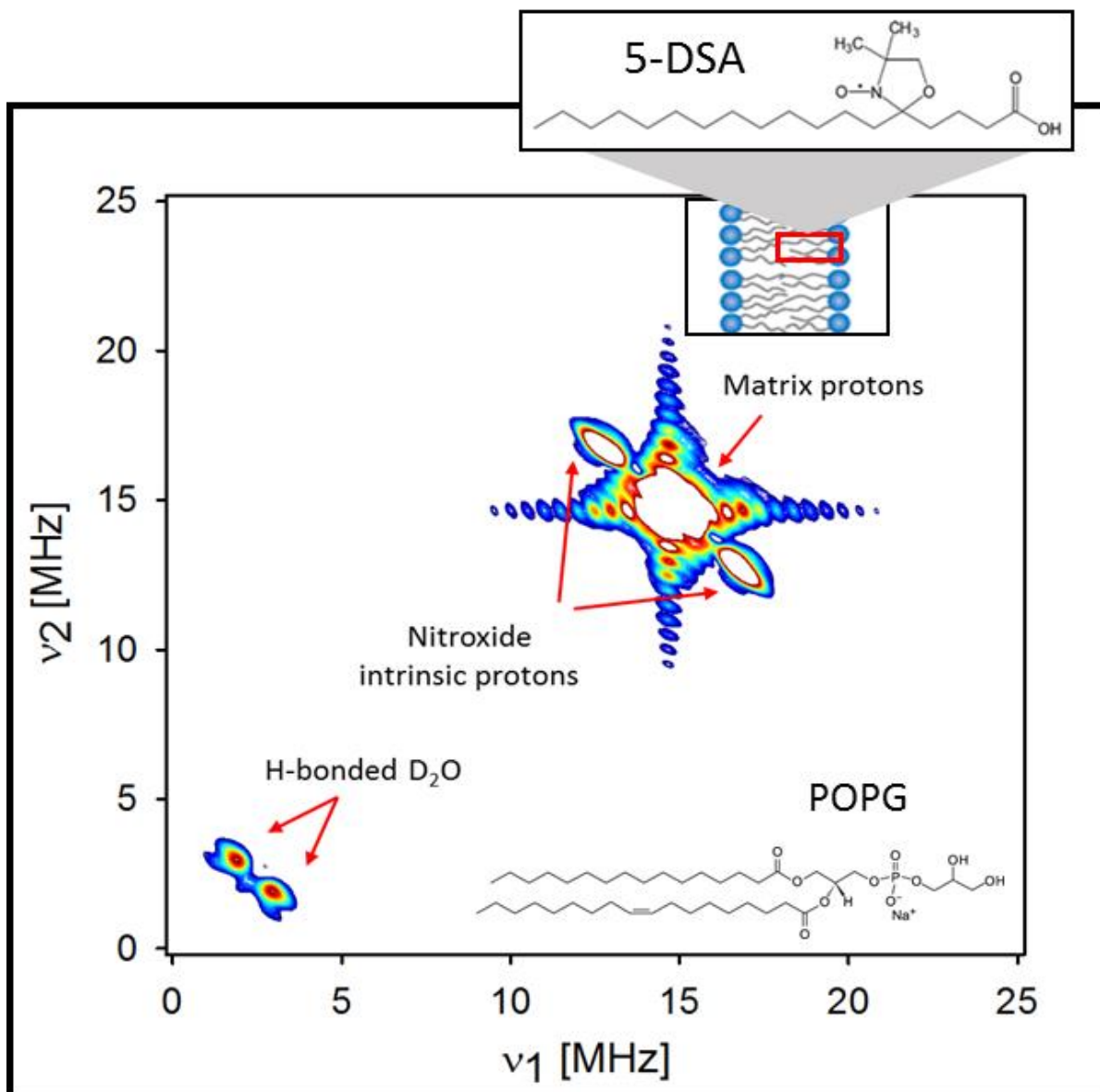


Figure 1.19. HYSCORE spectrum of 5-DSA in POPG Bilayers.

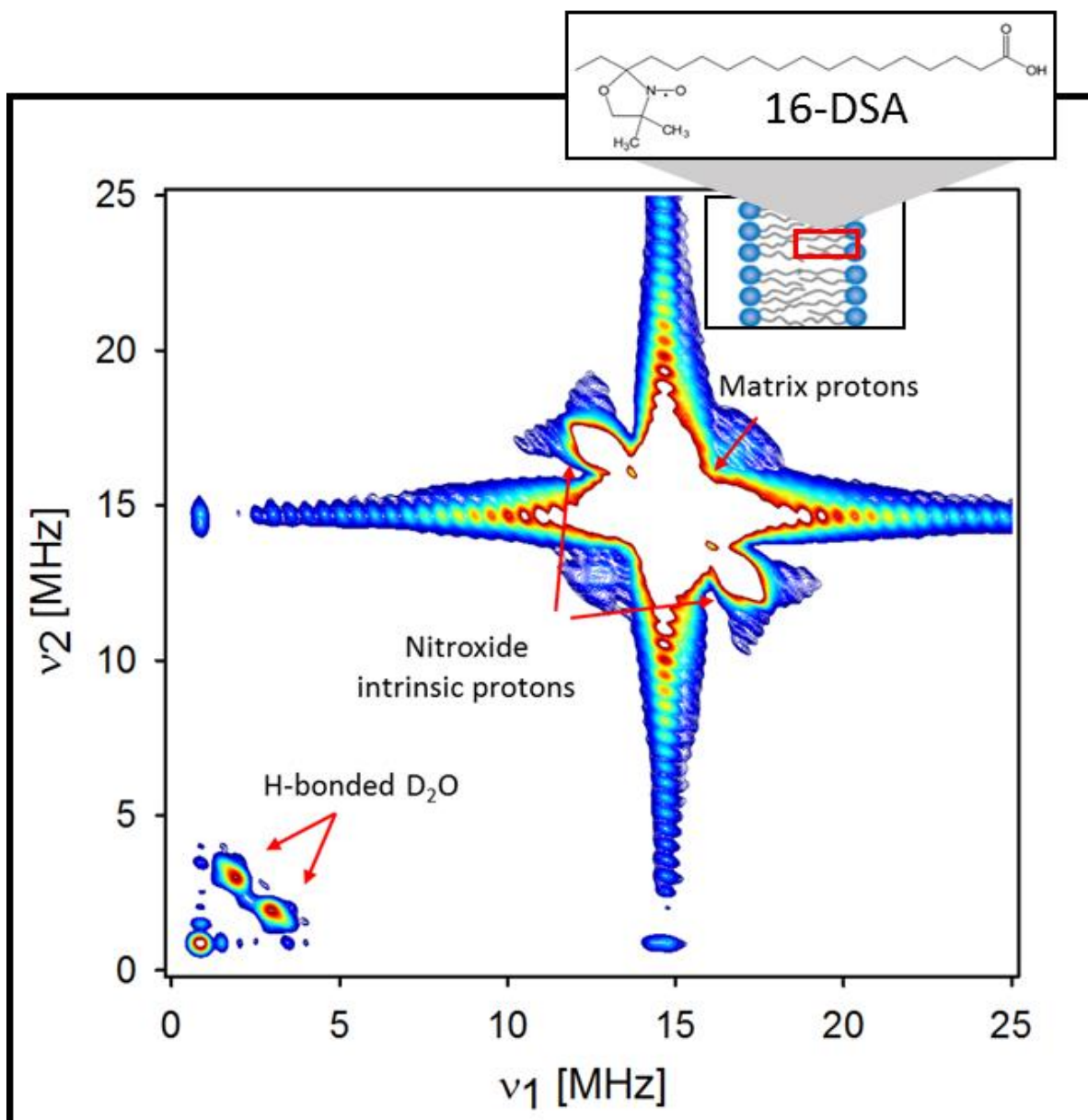


Figure 1.20. HYSCORE spectrum of 16-DSA in POPG Bilayers.

4.3.4.2. DOPC bilayers doped with WALP-n-MTSSL (water profiling at the lipid-peptide interface)

In addition to probing water permeation into lipid bilayers, water concentration was profiled along a lipid-peptide interface. For this experiment, we used a series of spin-labeled α -helical, membrane-spanning WALP peptides (see **Table 1** for peptide sequences) embedded into DOPC bilayers. The position of the spin label was systematically changed along the peptide backbone (nitroxide scan). A water concentration profile measured along the WALP peptide-DOPC lipids interface using methanol and ethanol rulers are shown in **Figure 1.21** and **Figure 1.22**, respectively.

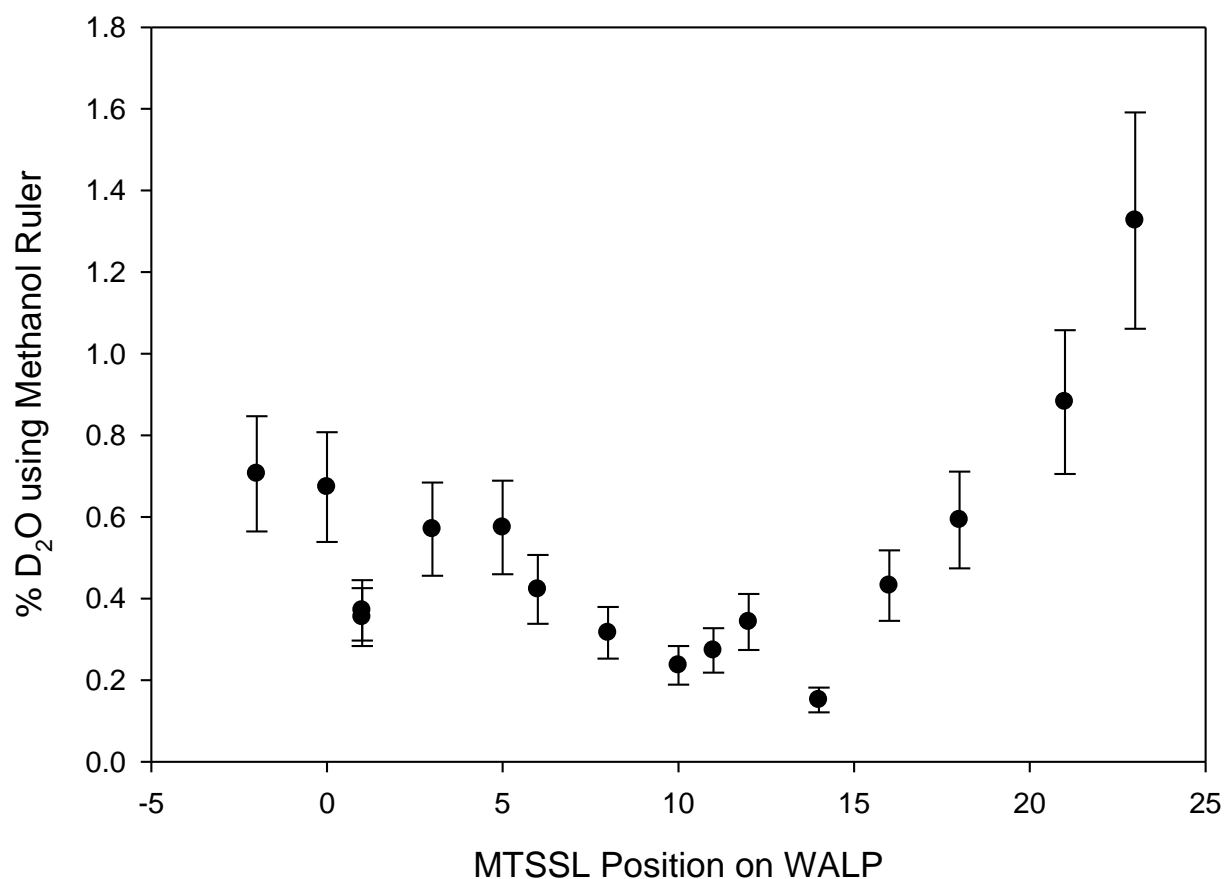


Figure 1.21. Water concentration profile obtained along WALP-DOPC bilayer interface using the proposed HYSORE method and Tempo radical solution in methanol-toluene as a model system.

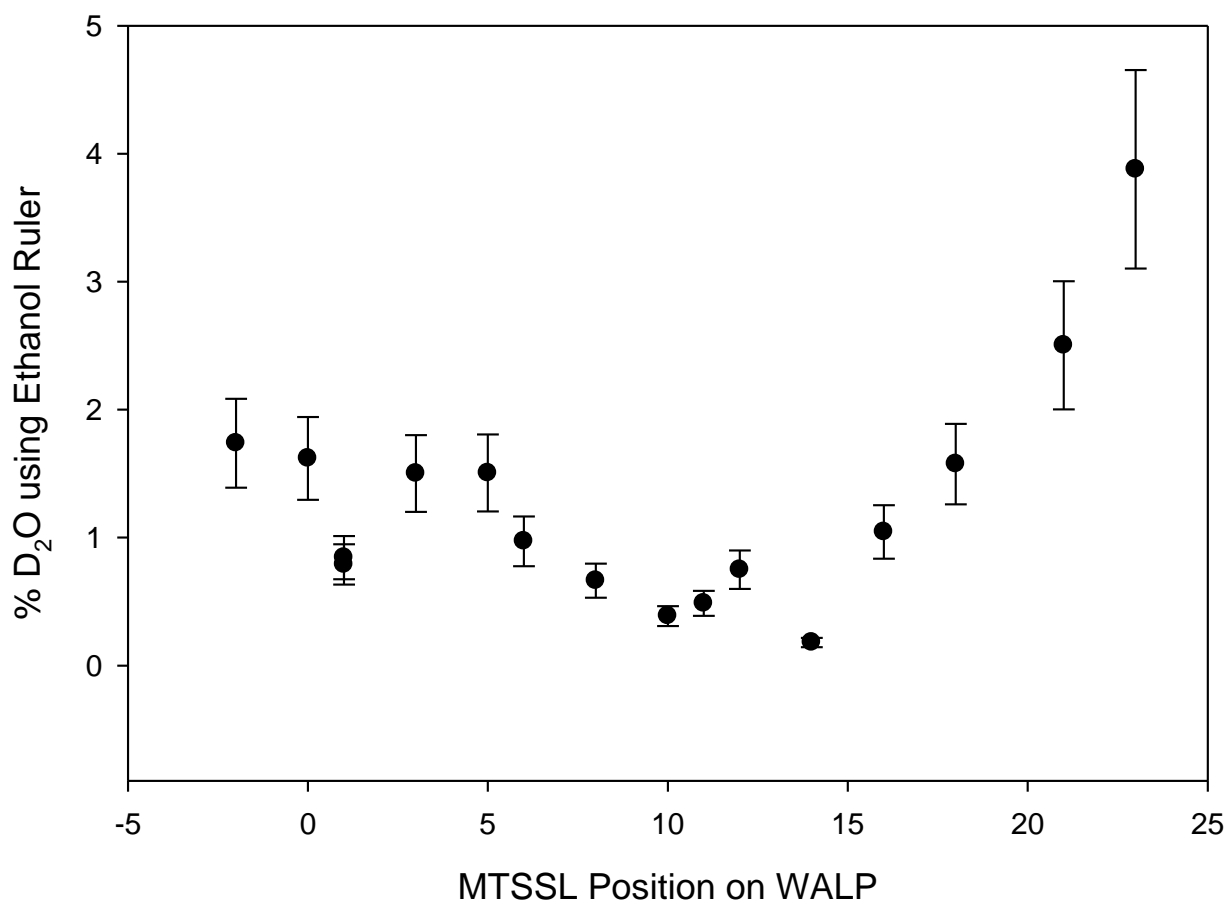


Figure 1.22. Water concentration profile obtained along WALP-DOPC bilayer interface using the proposed HYSORE method and Tempo radical solution in ethanol-toluene as a model system.

As discussed above, chemical equilibriums of TEMPO spin label in the ethanol-toluene mixture are shifted towards higher concentrations, compared to the methanol-toluene mixture,

resulting in water concentration estimates approximately a factor of 3 higher than the values obtained if methanol-toluene is used as a mimic. Moreover, the rate of hydrogen bond formation is expected to be even higher for water, compared to methanol, due to its smaller molecular size. Thus, while the present method provides reasonably good estimates of water concentration inside the lipid membrane, the actual water concentration inside the membrane is probably even somewhat lower. Therefore, we will consider estimates obtained by using methanol-toluene mimic as more accurate and these results will be referred further in the text.

The observed water concentration gradient near the membrane surface qualitatively agrees with theoretical predictions of a steep water gradient of around 15 angstroms from the membrane center (Wiener & White, 1992).

Water concentrations measured in the hydrophobic regions of the membrane (below 1%) are slightly higher than the water solubility in non-polar hydrocarbon liquids. At the center of the membrane, we measured 0.2-0.4(vol)% of water, in agreement with our results obtained for 16-DSA (spin label near middle of membrane) – in which we obtained 0.4(vol)% water (using methanol ruler).

As it can be seen from **Figure 1.21** and **Figure 1.22**, the plot is somewhat asymmetric with respect to the center of the bilayer (which corresponds to approximately position 12 of the spin-labeled WALP peptide). We suggest that the asymmetry seen in the water concentration profile could be caused by the spin labels at the C-terminus experiencing a slightly more polar environment than those at the N-terminus, due to the position of peptide itself being asymmetric with respect to the center of the DOPC bilayer center. We speculate that one of the possible reasons for this asymmetric positioning is a dipole moment of the WALP peptide. It is well known that α -helical peptides possess a significant (3.46 D per a residue) dipole moment directed from the

C-terminus to the N-terminus (W. G. J. Hoi 1978), i.e., the α -helix could be considered as an extended dipole with the negative charge located at the C-terminus, and the positive charge located at the N-terminus. If it is so, in the bilayer composed of zwitterionic DOPC lipids the positively charged N-terminus, which coincides with the smaller numbers of the spin-labeling position, will be slightly pulled down closer to the negatively charged phosphate ($P-O^-$) group, deeper to the low-dielectric environment of the bilayer. The negatively charged C-terminus, on the contrary, will be slightly pushed out to the more polar environment, toward positively charged trimethylammonium ($N(CH_3)_3^+$) residue.

Another potential reason could be a significant effect of the spin label location on the peptide tilt angle (with respect to the membrane normal) distribution inside the DOPC bilayer. The distributions of the tilt angles are known to be rather broad and thus having no strong specific preferences (Özdirekcan, Etchebest et al. 2007; Holt, Rougier et al. 2010; Im, Jo et al. 2012). In this case, even small perturbations, such as spin labeling, could potentially affect the preferred tilt angles, introducing significant asymmetry with respect to the position of WALP peptide residues.

The somewhat sharp water gradient observed at one of the ends of the WALP peptide confirms higher spatial resolution of the method, since gradients observed by ESEEM and Overhauser DNP are significantly less steep (Segawa, et al., 2016). The potentially high spatial resolution ($\sim 2\text{\AA}$) of the method described here is diminished by the uncertainty of the spin label position due to flexibility of the linker connecting the label to the peptide backbone (Rink, Riesle et al. 1997; Hustedt, Stein et al. 2006; Fleissner, Bridges et al. 2011).

In addition to the fraction of H-bonded water measured by HYSCORE, intensity of the matrix deuteron signal of 3-pulse ESEEM spectra has been detected for the same WALP peptide/DOPC lipid samples. The intensities of the matrix deuteron peaks normalized by the

electron spin echo intensity are shown in **Figure 1.23** for all measured spin label positions. Compared to the HYSORE based method described above, only relative change of local water concentration could be obtained using this method, while estimates of absolute values of water concentration are not feasible. The observed profile exhibits significantly flatter water concentration gradients. While small asymmetry of the profile is still observed, it is not as drastic as it was determined by HYSORE. This is in line with lower spatial resolution of the ESEEM method caused by long range dipole-dipole interactions between the unpaired electron of the spin probe and numerous deuterons of matrix water.

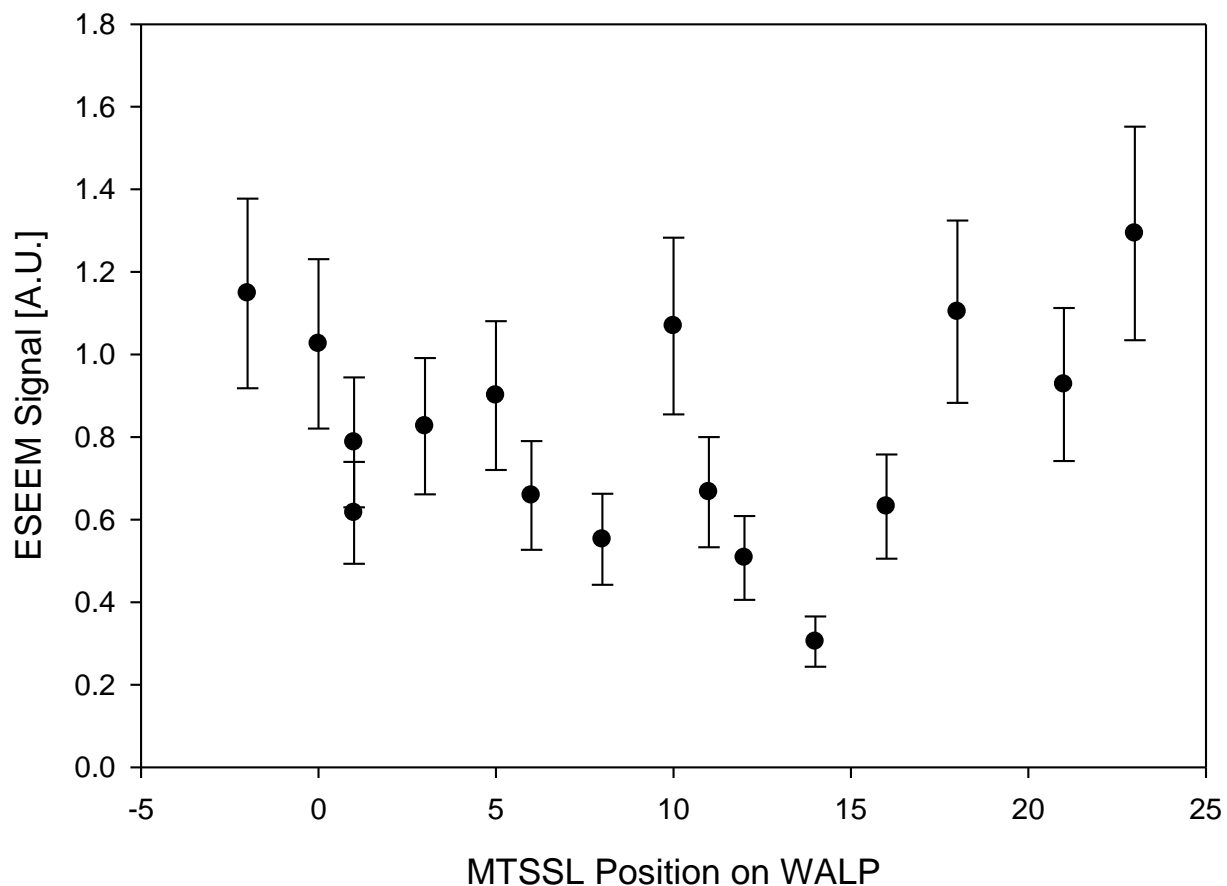


Figure 1.23. Profile of relative concentration of water given in arbitrary units as obtained along WALP-DOPC bilayer interface using the 3-pulse ESEEM method.

4.3.5. Comparison to Existing Methods

We compared the results obtained by the novel method proposed here to those obtained by utilizing 3-pulse ESEEM (**Figure 1.23**) and Overhauser DNP (**Figure 1.24**) reported recently by Segawa et al (Segawa, et al., 2016).

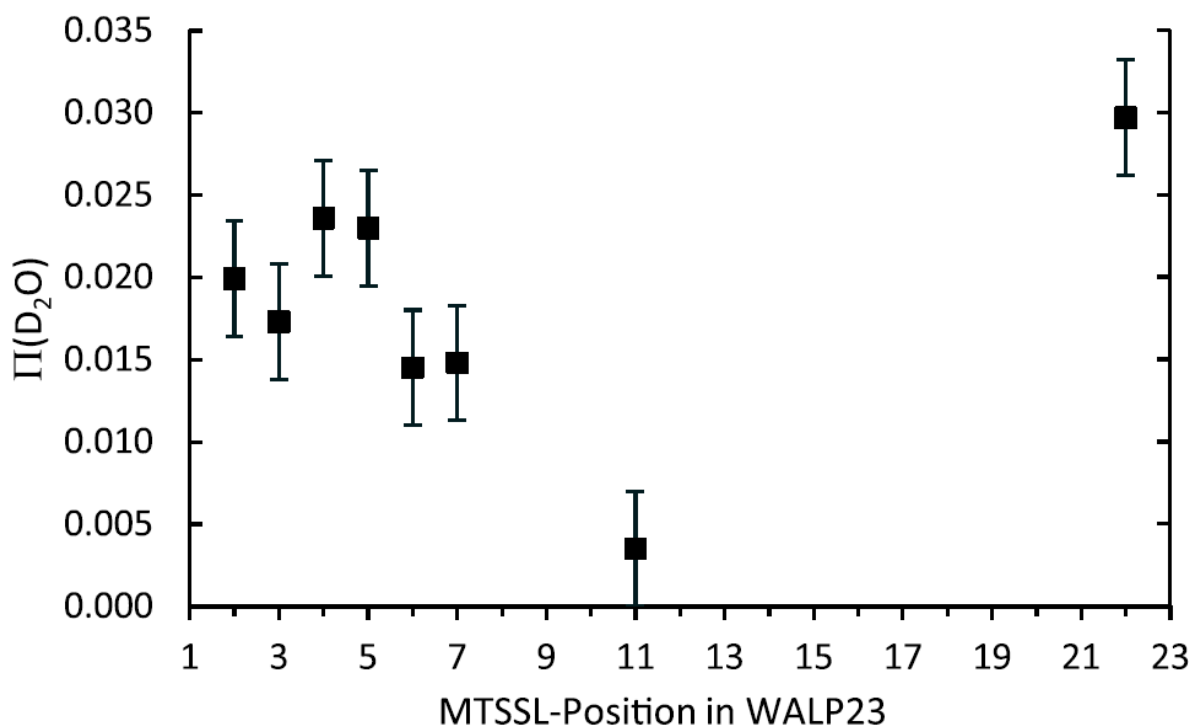


Figure 1.24. Accessibility parameter of D_2O vs position obtained by 3-Pulse ESEEM of MTSSL-WALP in DOPC bilayers (Segawa, et al., 2016).

As already discussed above, as compared to the methods utilizing 3-pulse ESEEM and O-DNP, the method proposed here yields higher spatial resolution and more importantly, yield absolute value of local water concentrations. In contrast, the water permeation profile obtained using Overhauser DNP (O-DNP) is indirectly related and is hard to convert to actual water concentration. In the O-DNP method, the DNP enhancement parameter is measured. This

experimentally obtained parameter is difficult to relate to real water concentration, since the DNP enhancement parameter is highly affected by local spin dynamics and also due to the complexity of the DNP relaxation phenomenon. The water permeation profile obtained by Segawa et al. (Segawa, et al., 2016) using 3-pulse ESEEM is similar to that obtained by us, taking into account the difference in spin label positions in two experiments.

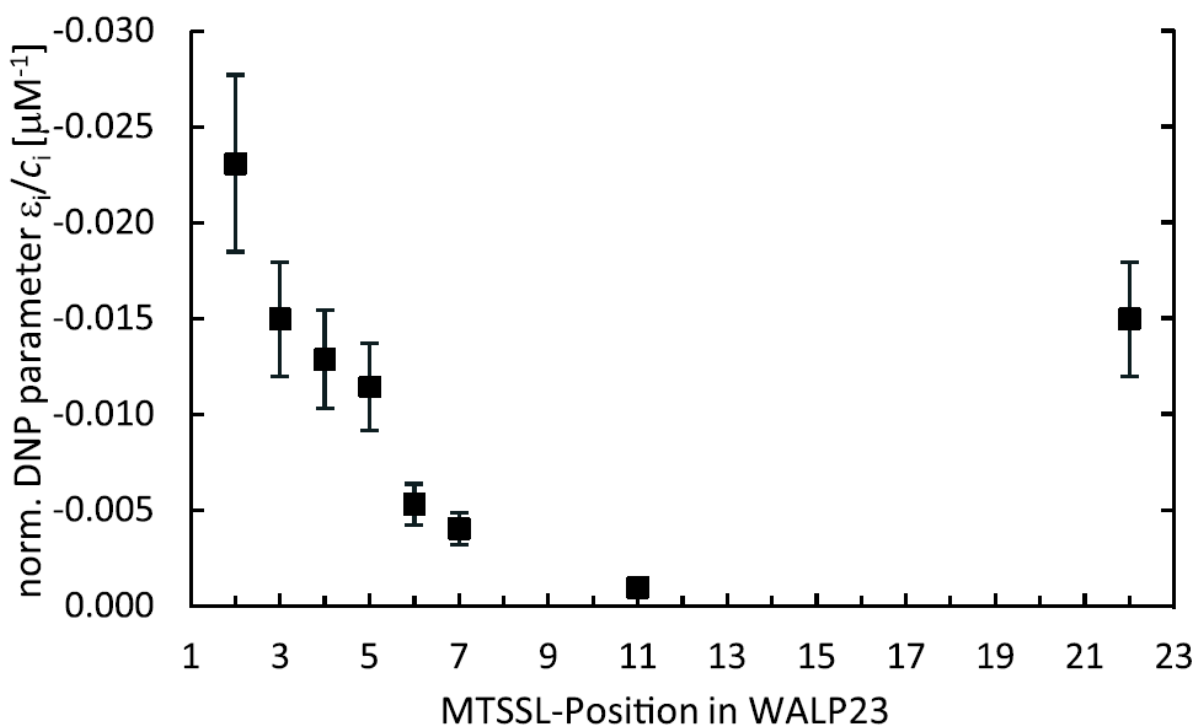


Figure 1.25. Normalized DNP parameter vs position obtained by Overhauser DNP of MTSSL-WALP in DOPC bilayers (Segawa, et al., 2016).

Section 5

Extension of the Proposed Method to Measure Local Lithium Ion Concentrations.

5.1. Introduction

We hypothesize that our HYSORE method could be further extended towards detecting biologically important metal ions (such as Na^+ and Li^+) using specially designed spin probes. For the method to work, the designed nitroxide spin label should provide a binding site in a close proximity to the NO group where approximately 90% of the electron spin density is located. Another necessary condition is that the ion of interest has at least one of its stable isotopes to be magnetic i.e. to have nuclear spin.

Among the other alkali cations, studying the Li^+ membrane permeation seems to present a most interesting and important scientific goal. Lithium's role in biological systems is not entirely understood, although it is considered an essential nutrient (Marshall 2015). For years, it has been known that animals need small amounts of lithium for reproductive health and maintenance of general health and wellness (Marshall 2015). At low doses, lithium acts as a nutrient required for B12 and folate transport and uptake (Schrauzer 2002). Lithium also up-regulates some neurotrophins (such as BDNF, brain-derived neurotrophic factor, and NGF, nerve-growth factor) which are important in neuronal function, plasticity, and repair (Young 2009). In addition, lithium has recently been described as an antioxidant and has anti-inflammatory activity, in addition to its powerful neuroprotective effects (Lieb 2008). Low doses of lithium therapy has potential to prevent or treat a wide range of neurological disorders, such as traumatic brain injury, Alzheimer's disease, Parkinson's disease, amyotrophic lateral sclerosis (ALS), chronic pain, mercury toxicity, depression/anxiety, alcoholism, and drug addiction (Marshall 2015).

Literature reports on the application of HYSCORE spectroscopy to detect Li nuclei are rather scarce and limited to characterization of only solid inorganic materials. For example, ^7Li -HYSCORE was employed to study paramagnetic defects created by γ -irradiation in mixed alkali silicate glasses. (Polienko, Schanding et al. 2008). ^7Li -HYSCORE of nitroxides was also used for characterization of the di-tert-butyl nitroxide- Li^+ adsorption complex in zeolites (Woldman, Semenov et al. 2009) and polymer-clay interface in polymer-clay nanocomposite materials (Guo, Zhao et al. 2019). However, no reports on the application of ^7Li -HYSCORE of nitroxides, both in solution and lipid bilayers, can be found in literature. Thus, the proposed here combination of ^7Li -HYSCORE spectroscopy with site-directed spin labeling methods would provide a new measurement capability for biomedical researchers.

For the extension of the proposed method to the detection of Li^{2+} in heterogeneous biological systems, like lipid membranes, the design of novel nitroxide probes and labels capable of chelating Li^+ ions is required. The main idea of the design of such label would be to coordinate Li^+ to a donor group in the immediate vicinity of the nitroxide group, so it would form a five or six-membered chelating cycle involving the $\text{N}-\text{O}^\bullet$ moiety itself. The chelating effect is expected to increase stability of the bound ($\text{Li}^+ \dots \bullet\text{O}-\text{N}$) species due to a higher binding constant. The significantly higher fraction of the bound Li^+ (we anticipate increasing this fraction by at least two orders of magnitude) would result in a proportionally higher intensity of the corresponding HYSCORE peaks/ridges allowing for Li^+ quantification across the bilayer with a high resolution.

5.2. Preliminary Results and Outlook

Here, are presented the preliminary steps towards the major goal – extending the above described method to measure local concentration of water towards the lithium ions. **Figure 1.26** shows the HYSORE spectrum measured for TEMPO radicals in frozen MTHF glass in presence of 1M of LiClO_4 .

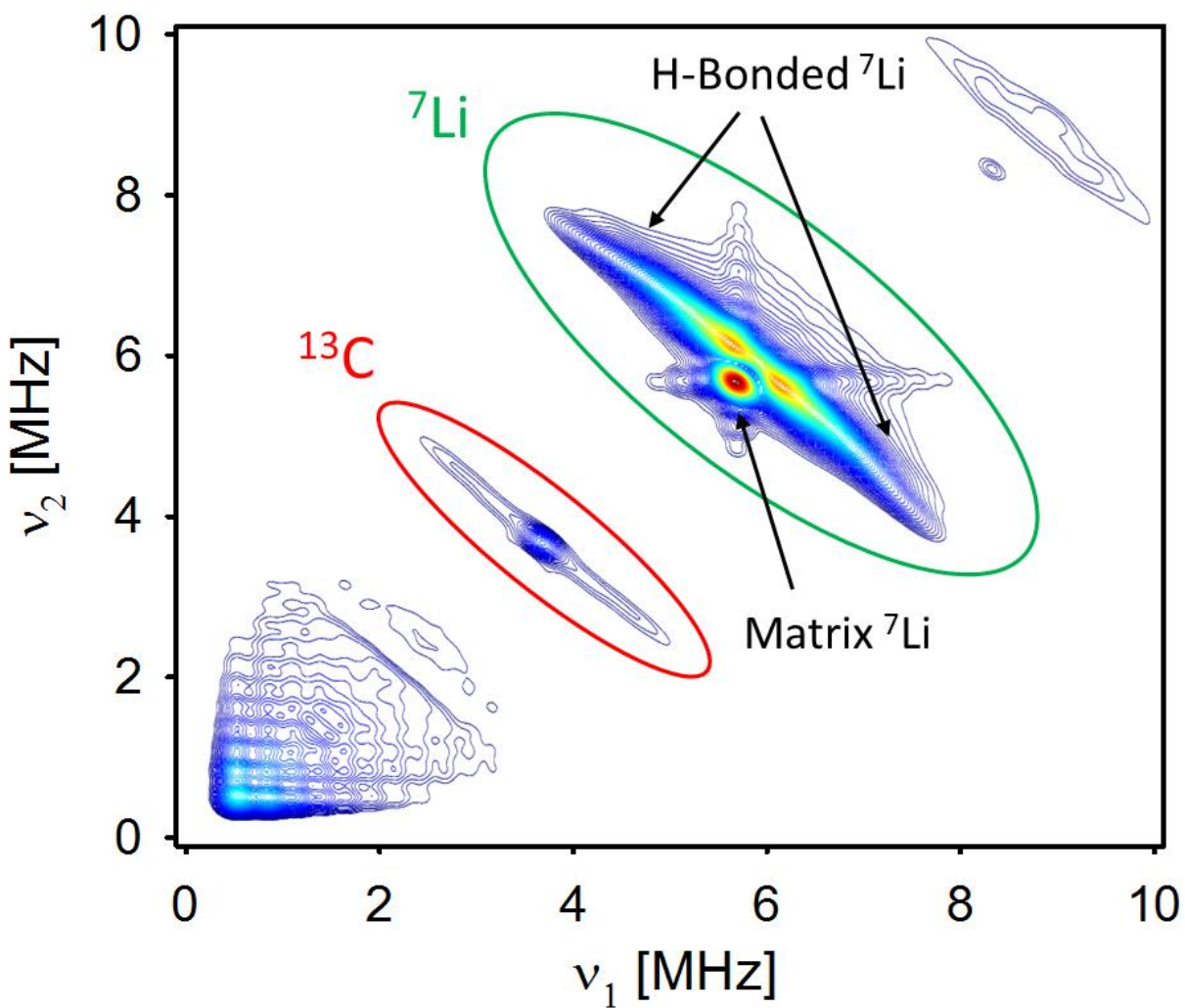


Figure 1.26. HYSORE spectrum measured for TEMPO radicals in frozen MTHF glass in presence of 1M of LiClO_4 .

The most intense feature of the spectrum - the peak located on the main diagonal at ~ 5.7 MHz corresponds to matrix (homogeneously distributed across the frozen glass) ^7Li nuclei. Small HYSORE signals at ~ 3.6 MHz belong to the naturally abundant ($\sim 1\%$) ^{13}C , primarily from the solvent matrix, as well as TEMPO radical itself. More importantly, rather intense and extended 2D ridges from strongly coupled ^7Li are observed. **Figure 1.27** shows selectively these pair of ridges plotted in squared frequency coordinates.

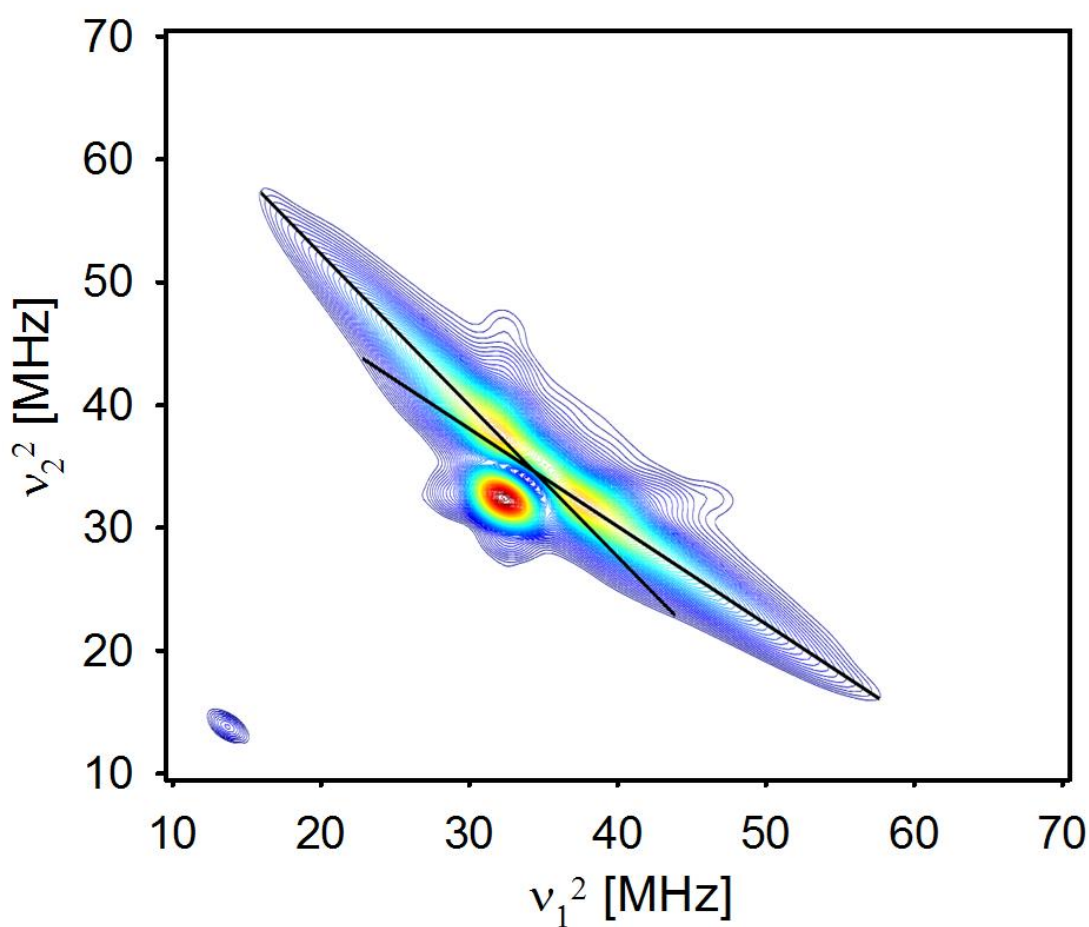


Figure 1.27. Lithium ridges plotted in squared frequency coordinates from the HYSORE spectrum measured for TEMPO radicals in frozen MTHF glass in presence of 1M of LiClO_4 .

In these squared frequency coordinates, the ridges are well approximated by segments of two straight lines, indicating that only one type of magnetic coupling is detected. Using the linear analysis procedure, described in details previously (e.g., (Chatterjee, Milikisiyants et al. 2011)), quantitative information about electron-nuclear hyperfine coupling could be obtained. More precisely, based on the slope and the intercept of the two straight lines containing the segments, both isotropic, $A_{\text{iso}}=0.15\text{MHz}$, and anisotropic, $T=1.98\text{MHz}$, components of the hyperfine coupling could be estimated. The sizes of these two components clearly indicate that the observed ^7Li -HYSCORE signal originates from the ^7Li nuclei bound with oxygen atom of the N-O^\bullet group. The distance between the oxygen atom and ^7Li could be estimated using point-dipole approximation from the size of anisotropic coupling parameter $T=1.98\text{ MHz}$ to be 1.91 \AA - a typical internuclear distance for hydrogen bonding-type interaction. Moreover, small isotropic coupling of $A_{\text{iso}}=0.15\text{ MHz}$ indicates very little spin density transfer over such short distance, further confirming the hydrogen bond nature of the observed ^7Li -HYSCORE signal. These data provide clear evidence that nitroxide spin labels are capable of binding lithium ions and the above described method applied to measure water concentration could in principle be extended to small metal ions.

Figure 1.28 shows the dependence of ^7Li -HYSCORE signal intensity for both, weakly coupled matrix (solvent) nuclei as well as stronger coupled nitroxide-bound nuclei on concentration of LiClO_4 salt in frozen MTHF.

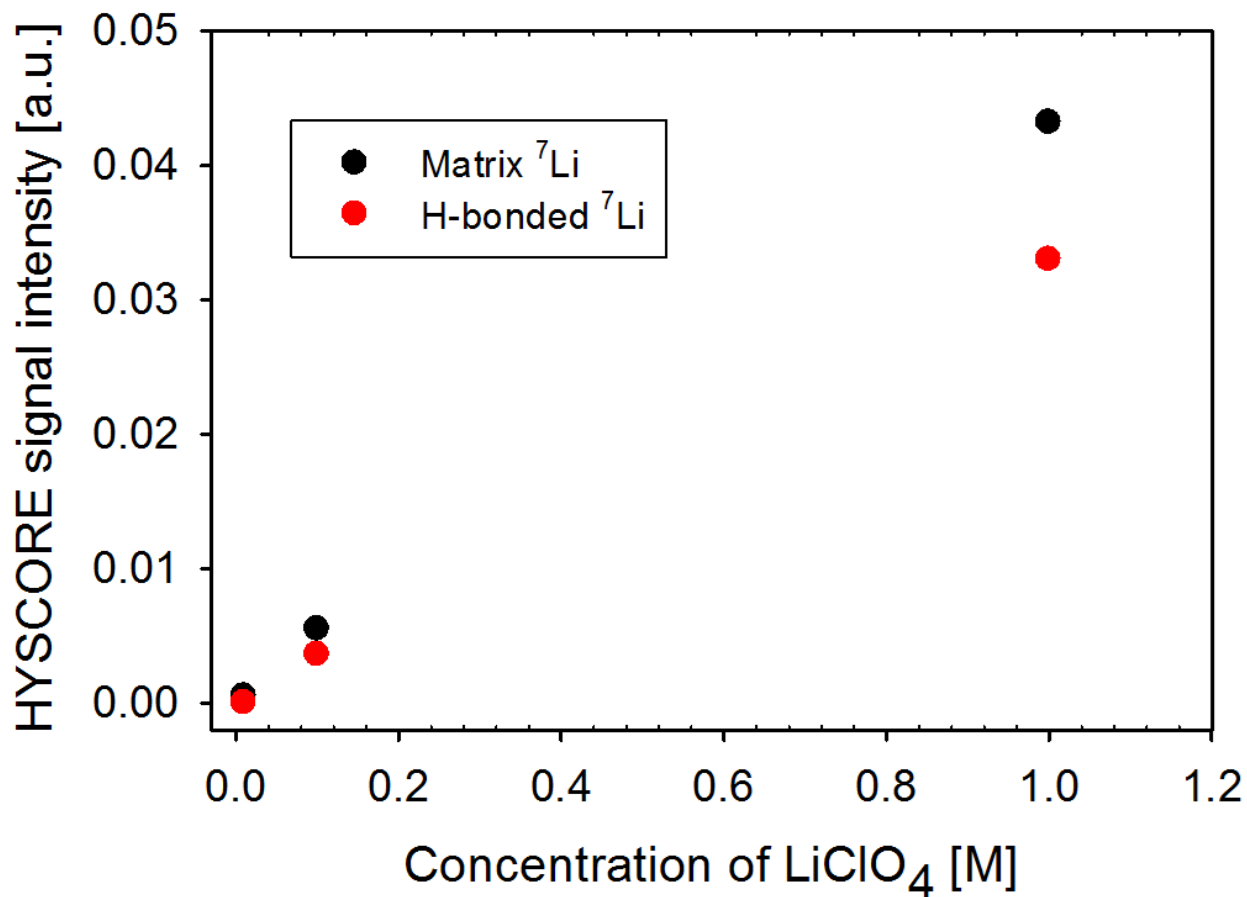


Figure 1.28. Dependence of HYSCORE signal intensity of matrix as well as nitroxide-bound ⁷Li nuclei on concentration of LiClO₄ salt in frozen MTHF.

As can be seen from the figure, both signals grow approximately linearly with the concentration of LiClO₄. While linear growth of matrix signal is expected to be directly proportional to the bulk Li⁺ concentration, absence of signal intensity saturation for the bound nuclei clearly indicate low binding affinity of Li⁺ to the N–O• group of TEMPO radical. This confirms the above mentioned suggestion, that a series of novel intelligently designed nitroxide

spin probes optimal for Li⁺ binding is required for applicability of the method to biologically relevant systems in particular lipid membranes.

We speculate that the efficiency of our method with respect to Li⁺ detection could be improved if the nitroxide moiety (N–O•) will be involved into cation chelation. Examples of the nitroxides that could be used in Li⁺ chelation HYSCORE experiments are shown in **Figure 29**. Compounds 1 and 2 (Amitina & Volodarskii, 1976); Compounds 4 and 5 (Grigor'ev, et al., 1985); Compounds 3 and 5 (Grigor'ev, Shchukin, Dikanov, Kuznetsova, & Volodarskii, 1982).

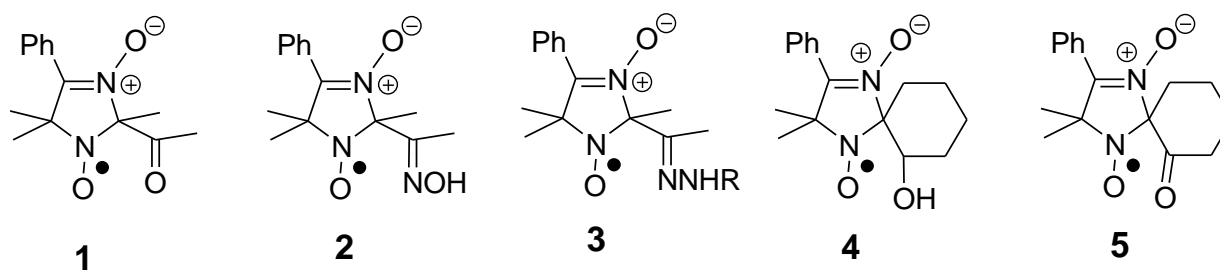


Figure 1.29. Compounds 1 and 2 (Amitina & Volodarskii, 1976); Compounds 4 and 5 (Grigor'ev, et al., 1985); Compounds 3 and 5 (Grigor'ev, Shchukin, Dikanov, Kuznetsova, & Volodarskii, 1982).

The proposed new spectroscopic methodology and new membrane probes are expected to expand the arsenal of biomedical and biophysical methods for nondestructive studies of the transport, mobility and distribution of the alkali metal ions, as well as other small-molecule analytes, in membranes, cells, and biological tissues. We also hypothesize that our chelating nitroxides could be further used as enhancement agents for Overhauser DNP.

CHAPTER 1 REFERENCES

- Amitina, S. A., & Volodarskii, L. B. (1976). Synthesis of Sterically Hindered 1-Hydroxy-2-Acetyl-3-Imidazoline 3-Oxides and Stable Nitroxyl Radicals From Them. *Russ Chem Bull*, 25, 1997-1999.
- Astrakas, Y., Deligiannakis, Y., Mitrikas, G., & Kordas, G. (1998). *Journal of Chemical Physics*, 109, 8612.
- Carpenter, E. P., & Iwata, S. (2008, October). Overcoming the challenges of membrane protein crystallography. *Current Opinion in Structural Biology*, 18(5), 581-586.
- Charifson, P. S., Hiskey, R. G., & Pedersen, L. G. (1997). Construction and molecular modeling of phospholipid surfaces. *Journal of Computational Chemistry*, 11, 1181-1186.
- Farahbakhsh, Z. T., Altenbach, C., & Hubbell, W. L. (1992). Spin Labeled Cysteines as Sensors for Protein-Lipid Interaction and Conformation in Rhodopsin. *Photochemistry and Photobiology*, 56(6), 1019-1033.
- Griffith, O. H., Dehlinger, P. J., & Van, S. P. (1974, December). Shape of the hydrophobic barrier of phospholipid bilayers (Evidence for water penetration in biological membranes). *The Journal of Membrane Biology*, 15(1), 159-192.
- Grigor'ev, I. A., Shchukin, G. I., Dikanov, S. A., Kuznetsova, I. K., & Volodarskii, L. B. (1982). Formation of 2,3,6,8-Tetraazabicyclo(3,2,1)Oct-3-ene Derivatives in Reaction Between 2-Acyl-3-Imidazoline 3-Oxides and Hydrazine and their Oxidation to the Corresponding Nitroxyl Radicals and 1,2,4-Triazine 4-Oxide. *Russ Chem Bull*, 31, 972-980.
- Grigor'ev, I. A., Shchukin, G. I., Khramtsov, V. V., Vainer, L. M., Starichenko, V. F., & Volodarskii, L. B. (1985). Conversion of 3-Imidazoline-3-Oxide Nitroxyl Radicals into Nitronylnitroxyl Radicals. *Russ Chem Bull*, 34, 2169-22177.
- Gutjahr, M., Bottcher, R., & Poppl, A. (2002). *J. Phys. Chem.*, 106, 1345-1349.
- Marsh, D. (2001). Polarity and permeation profiles in lipid membranes. *Proceedings of the National Academy of Sciences of the United States of America*, 98(14), 7777-7782.
- Marsh, D. (2001, July 3). Polarity and permeation profiles in lipid membranes. *Proceedings of the National Academy of Sciences of the United States of America*, 98(14), 7777-7782.
- Milov, A. D., Samoilova, R. I., Shubin, A. A., Grishin, Y. A., & Dzuba, S. A. (2008, November). ESEEM Measurements of Local Water Concentration in D₂O-Containing Spin-Labeled Systems. *Applied Magnetic Resonance*, 35(1), 73-94.

- Murray, D., Ben-Tal, N., Honig, B., & McLaughlin, S. (1997). Electrostatic interaction of myristoylated proteins with membranes: simple physics, complicated biology. *Structure*, 5(8), 985-989.
- Nielson, R. D., Che, K., Gelb, M. H., & Robinson, B. H. (2004, November). A Ruler for Determining the Position of Proteins in Membranes. *Journal of the American Chemical Society*, 127, 6430-6442.
- O'Connor, C. M., & Adams, J. U. (2010). *Essentials of Cell Biology*. Cambridge, MA: NPG Education.
- Schweiger, A., & Jeschke, G. (2001). *Principles of pulse electron paramagnetic resonance*. Oxford, UK: Oxford University Press.
- Segawa, T. F., Doppelbauer, M., Garbulo, L., Doll, A., Polyhach, Y. O., & Jeschke, G. (2016). Water accessibility in a membrane-inserting peptide comparing Overhauser DNP and pulse EPR methods. *The Journal of Chemical Physics*, 144, 194201.
- Smirnova, T. I., & Smirnov, A. I. (2007). High-field ESR Spectroscopy In Membrane And Protein Biophysics. In M. A. Hemminga, & L. Berliner, *ESR Spectroscopy in Membrane Biophysics* (Vol. 27). New York, NY: Springer.
- Smirnova, T. I., & Smirnov, A. I. (2015, April 4). Peptide-membrane Interactions by Spin-labeling EPR. *Methods in enzymology*, 564, 219-258.
- Smirnova, T. I., Smirnov, A. I., Pachtchenko, S., & Poluektov, O. G. (2007, March 28). Geometry of Hydrogen Bonds Formed by Lipid Bilayer Nitroxide Probes: A High Frequency Pulsed ENDOR/EPR Study. *Journal of the American Chemical Society*, 129(12), 3476-3477.
- Subczynski, W. K., Wisniewska, A., Hyde, J. S., & Kusumi, A. (1994). *Biochemistry*, 159-192.
- White, S. (2018, April 8). Membrane Proteins of Known 3D Structure. Retrieved from Stephen White Laboratory Homepage: <http://blanco.biomol.uci.edu/mpstruc/>
- White, S. H., & Wimley, W. C. (1998, Nov 10). Hydrophobic interactions of peptides with membrane interfaces. *Biochimica et Biophysica Acta*, 1376(3), 339-352.
- Wiener, M. C., & White, S. H. (1992). Structure of a fluid dioleoylphosphatidylcholine bilayer determined by joint refinement of x-ray and neutron diffraction data. III. Complete structure. *Biophysical Journal*, 61(2), 434-447.
- Wiener, M. C., & White, S. H. (1992). Structure of a fluid dioleoylphosphatidylcholine bilayer determined by joint refinement of x-ray and neutron diffraction data. III. Complete structure. *Biophysical Journal*, 61(2), 434-47.

- Zeevi, A., & Margalit, R. (1991). *J. Membrane Biol.*, 133-140.
- Bratt, P. J., O. G. Poluektov, et al. (2000). "The g-factor anisotropy of plant chlorophyll a(center dot)." *Journal of Physical Chemistry B* **104**(30): 6973-6977.
- Bratt, P. J., M. Rohrer, et al. (1997). "Submillimeter high-field EPR studies of the primary donor in plant photosystem I P700." *Journal of Physical Chemistry B* **101**(47): 9686-9689.
- Breton, J., E. Nabedryk, et al. (1999). "FTIR Study of the Primary Electron Donor of Photosystem I (P700) Revealing Delocalization of the Charge in P700+and Localization of the Triplet Character in 3P700." *Biochemistry* **38**(36): 11585-11592.
- Budil, D. E. and M. C. Thurnauer (1991). "The chlorophyll triplet state as a probe of structure and function in photosynthesis." *Biochimica et biophysica acta* **1057**(1): 1-41.
- Chatterjee, R., S. Milikisiyants, et al. (2011). "High-Resolution Two-Dimensional ^1H and ^{14}N Hyperfine Sublevel Correlation Spectroscopy of the Primary Quinone of Photosystem II." *Biochemistry* **50**(4): 491-501.
- Chion, B. and J. Lajzerowiczbonneteau (1980). "Hydrogen-Bonds and Short Intermolecular Contacts Involving Nitroxide Groups in Crystals." *Acta Crystallographica Section B-Structural Science Crystal Engineering and Materials* **36**(Apr): 998-1000.
- Chitnis, P. R. (1996). "Photosystem I." *Plant physiology* **111**(3): 661-669.
- Chitnis, P. R., Q. Xu, et al. (1995). "Function and organization of Photosystem I polypeptides." *Photosynthesis research* **44**(1-2): 23-40.
- Deligiannakis, Y., M. Louloudi, et al. (2000). "Electron spin echo envelope modulation (ESEEM) spectroscopy as a tool to investigate the coordination environment of metal centers." *Coordination Chemistry Reviews* **204**(1): 1-112.
- Den Blanken, H. J. and A. J. Hoff (1983). "High-resolution absorbance-difference spectra of the triplet state of the primary donor P-700 in Photosystem I subchloroplast particles measured with absorbance-detected magnetic resonance at 1.2 K. Evidence that P-700 is a dimeric chlorophyll complex." *Biochimica et Biophysica Acta (BBA) - Bioenergetics* **724**(1): 52-61.
- Dikanov, S. A., A. M. Tyryshkin, et al. (2000). "Intensity of cross-peaks in hyscore spectra of $S = 1/2$, $I = 1/2$ spin systems." *Journal of magnetic resonance* **144**(2): 228-242.
- Dikanov, S. A., L. Xun, et al. (1996). "Orientationally-Selected Two-Dimensional ESEEM Spectroscopy of the Rieske-Type Iron-Sulfur Cluster in 2,4,5-Trichlorophenoxyacetate Monooxygenase from *Burkholderia cepacia* AC1100." *Journal of the American Chemical Society* **118**(35): 8408-8416.

- Diller, A., E. Roy, et al. (2007). "15N photochemically induced dynamic nuclear polarization magic-angle spinning NMR analysis of the electron donor of photosystem II." Proceedings of the National Academy of Sciences of the United States of America **104**(31): 12767-12771.
- Flanagan, H. L. and D. J. Singel (1987). "Analysis of 14N ESEEM patterns of randomly oriented solids." The Journal of Chemical Physics **87**(10): 5606-5616.
- Frank, H. A., M. B. McLean, et al. (1979). "Triplet states in photosystem I of spinach chloroplasts and subchloroplast particles." Proceedings of the National Academy of Sciences of the United States of America **76**(10): 5124-5128.
- Fromme, P. (1996). "Structure and function of photosystem I." Current opinion in structural biology **6**(4): 473-484.
- Golbeck, J. H. (1992). "Structure and Function of Photosystem I." Annual Review of Plant Physiology and Plant Molecular Biology **43**(1): 293-324.
- Golbeck, J. H. (1994). "Photosystem I in Cyanobacteria." 319-360.
- Guo, W., M. Zhao, et al. (2019). "Developments towards synthesis of N-heterocycles from amidines via C–N/C–C bond formation." Organic Chemistry Frontiers **6**(13): 2120-2141.
- Höfer, P., A. Grupp, et al. (1986). "Hyperfine sublevel correlation (hyscore) spectroscopy: a 2D ESR investigation of the squaric acid radical." Chemical Physics Letters **132**(3): 279-282.
- Holzwarth, A. R., M. G. Muller, et al. (2006). "Ultrafast transient absorption studies on Photosystem I reaction centers from *Chlamydomonas reinhardtii*. 2: Mutations near the P700 reaction center chlorophylls provide new insight into the nature of the primary electron donor." Biophysical Journal **90**(2): 552-565.
- Jordan, P., P. Fromme, et al. (2001). "Three-dimensional structure of cyanobacterial photosystem I at 2.5 Å resolution." Nature **411**(6840): 909-917.
- Käss, H., P. Fromme, et al. (2001). "Orientation and Electronic Structure of the Primary Donor Radical Cation in Photosystem I: A Single Crystals EPR and ENDOR Study." The Journal of Physical Chemistry B **105**(6): 1225-1239.
- Kasumaj, B. and S. Stoll (2008). "5- and 6-pulse electron spin echo envelope modulation (ESEEM) of multi-nuclear spin systems." Journal of magnetic resonance **190**(2): 233-247.
- Käβ, H., P. Fromme, et al. (1996). "Quadrupole parameters of nitrogen nuclei in the cation radical P700.+ determined by ESEEM of single crystals of photosystem I." Chemical Physics Letters **257**(1-2): 197-206.

- Lendzian, F., M. Huber, et al. (1993). "The electronic structure of the primary donor cation radical in Rhodospirillum rubrum R-26: ENDOR and TRIPLE resonance studies in single crystals of reaction centers." Biochimica et Biophysica Acta (BBA) - Bioenergetics **1183**(1): 139-160.
- Lieb, J. (2008). "Defeating Cancer With Antidepressants." ecancermedicalsecience.
- Liesum, L. and A. Schweiger (2001). "Multiple quantum coherence in HYSCORE spectra." Journal of Chemical Physics **114**(21): 9478-9488.
- Lubitz, W. (2003). "Photochemical processes in photosynthesis studied by advanced electron paramagnetic resonance techniques." Pure and Applied Chemistry **75**(8): 1021-1030.
- Marshall, T. M. (2015). "Lithium as a Nutrient." J. Amer. Phys. Surg. **20**(4): 104-109.
- Müller, M. G., J. Niklas, et al. (2003). "Ultrafast Transient Absorption Studies on Photosystem I Reaction Centers from Chlamydomonas reinhardtii. 1. A New Interpretation of the Energy Trapping and Early Electron Transfer Steps in Photosystem I." Biophysical Journal **85**(6): 3899-3922.
- Najdanova, M., G. J. Janssen, et al. (2015). "Analysis of electron donors in photosystems in oxygenic photosynthesis by photo-CIDNP MAS NMR." Journal of photochemistry and photobiology. B, Biology **152**(Pt B): 261-271.
- Petrenko, A., A. L. Maniero, et al. (2004). "A High-Field EPR Study of P700⁺ in Wild-Type and Mutant Photosystem I from Chlamydomonas reinhardtii^{†,‡}." Biochemistry **43**(7): 1781-1786.
- Plato, M., N. Krauss, et al. (2003). "Molecular orbital study of the primary electron donor P700 of photosystem I based on a recent X-ray single crystal structure analysis." Chemical Physics **294**(3): 483-499.
- Plato, M., H.-J. Steinhoff, et al. (2002). "Molecular orbital study of polarity and hydrogen bonding effects on the g and hyperfine tensors of site directed NO spin labelled bacteriorhodopsin." Molecular Physics **100**(23): 3711-3721.
- Polienko, J. F., T. Schanding, et al. (2008). "Studies toward the Synthesis of 4-(2-R-ethyl)amino-2,2,5,5-tetramethyl-3-imidazoline 1-Oxyls. Nucleophilic Substitution of Bromide in the N-Alkyl Chain of the 1,2,4-Oxadiazol-2-one Precursor." The Journal of Organic Chemistry **73**(2): 502-510.
- Poluektov, O. G., L. M. Utschig, et al. (2002). "Electronic Structure of the P700 Special Pair from High-Frequency Electron Paramagnetic Resonance Spectroscopy." Journal. Physical Chemistry B **106**(35): 8911-8916.
- Ptushenko, V. V., D. A. Cherepanov, et al. (2008). "Semi-continuum electrostatic calculations of redox potentials in photosystem I." Photosynthesis Research **97**(1): 55-74.

- Saito, K. and H. Ishikita (2011). "Cationic State Distribution over the P700 Chlorophyll Pair in Photosystem I." *Biophysical Journal* **101**(8): 2018-2025.
- Schrauzer, G. N. (2002). "Lithium: Occurrence, Dietary Intakes, Nutritional Essentiality." *Journal of the American College of Nutrition* **21**(1): 14-21.
- Schweiger, A. and G. Jeschke (2001). *Principles of pulse electron paramagnetic resonance*. New York, Oxford University Press.
- Setif, P. and K. Brettel (1990). "Photosystem-I Photochemistry under Highly Reducing Conditions - Study of the P700 Triplet-State Formation from the Secondary Radical Pair (P700⁺-A1⁻)." *Biochimica Et Biophysica Acta* **1020**(3): 232-238.
- Smirnova, T. I., A. I. Smirnov, et al. (2007). "Geometry of hydrogen bonds formed by lipid bilayer nitroxide probes: A high-frequency pulsed ENDOR/EPR study." *Journal of the American Chemical Society* **129**(12): 3476-+.
- Srinivasan, N. and J. H. Golbeck (2009). "Protein-cofactor interactions in bioenergetic complexes: The role of the A(1A) and A(1B) phylloquinones in Photosystem I." *Biochimica Et Biophysica Acta-Bioenergetics* **1787**(9): 1057-1088.
- Stoll, S. and A. Schweiger (2006). "EasySpin, a comprehensive software package for spectral simulation and analysis in EPR." *Journal of Magnetic Resonance* **178**(1): 42-55.
- Teutloff, C., W. Hofbauer, et al. (2001). "High-frequency EPR studies on cofactor radicals in photosystem I." *Applied Magnetic Resonance* **21**(3-4): 363-379.
- Vrieze, J., P. Gast, et al. (1996). "Structure of the Reaction Center of Photosystem I of Plants. An Investigation with Linear-Dichroic Absorbance-Detected Magnetic Resonance." *The Journal of Physical Chemistry* **100**(23): 9960-9967.
- W. G. J. Hoi, P. T. v. D. H. J. C. B. (1978). "The α -helix dipole and the properties of proteins." *Nature* **273**(443-446).
- Wang, R. L., V. Sivakumar, et al. (2003). "Mutation induced modulation of hydrogen bonding to P700 studied using FTIR difference spectroscopy." *Biochemistry* **42**(33): 9889-9897.
- Webber, A. N. and W. Lubitz (2001). "P700: the primary electron donor of photosystem I." *Biochimica Et Biophysica Acta-Bioenergetics* **1507**(1-3): 61-79.
- Webber, A. N. and W. Lubitz (2001). "P700: the primary electron donor of photosystem I." *Biochimica et biophysica acta* **1507**(1-3): 61-79.

Woldman, Y. Y., S. V. Semenov, et al. (2009). "Design of liposome-based pH sensitive nanoSPIN probes: nano-sized particles with incorporated nitroxides." The Analyst **134**(5): 904.

Young, W. (2009). "Review of Lithium Effects on Brain and Blood." Cell Transplantation **18**(9): 951-975.

Zech, S. G., W. Hofbauer, et al. (2000). "A Structural Model for the Charge Separated State in Photosystem I from the Orientation of the Magnetic Interaction Tensors." The Journal of Physical Chemistry B **104**(41): 9728-9739.

CHAPTER 2

Electronic Structure of the Primary Electron Donor $P_{700}^{+\bullet}$ in Photosystem I Studied by Multifrequency HYSCORE Spectroscopy at X- and Q-Band

Melanie M. Chestnut, Sergey Millikisiyants, Ruchira Chatterjee, Junko Yano, Alex I. Smirnov

Section 1

Introduction

The pigment-protein complex of the photosystem I (PSI) is present in many organisms that perform photosynthesis including green sulfur bacteria, cyanobacteria, algae, and higher plants (Golbeck 1994; Chitnis, Xu et al. 1995; Chitnis 1996; Fromme 1996). PSI plays an important role in the photosynthetic reaction chain by utilizing harvested light energy to catalyze the oxidation of the plastocyanin/cytochrome c_6 and the reduction of ferredoxin/ferredoxin proteins.

It is commonly accepted that electron transfer in PSI starts with light-induced oxidation of the P_{700} pigment located in the structurally similar PsaA and PsaB membrane-spanning proteins (Srinivasan and Golbeck 2009). P_{700} is a heterodimer consisting of two chlorophyll molecules conventionally denoted as P_A and P_B referring to their location in the PsaA and PsaB subunits, respectively. Structurally, P_B is a chlorophyll a (Chl a) and P_A is C13²-epimer of the chlorophyll a (Chl a'). The electron transfer takes places sequentially via a series of acceptors conventionally called A_0 , A_1 , F_X , F_A and F_B (Srinivasan and Golbeck 2009). The central role of P_{700} in the function of PSI is probably related to its location at the interface of the excitation transfer from in the light harvesting system and the electron transfer in the reaction center as well as its unique redox properties distinct from all other chlorophylls (Käss, Fromme et al. 2001). The reduction potential of the electronically excited P_{700} is ~ -1.2 V making it possibly the most reducing chemical species in nature (Webber and Lubitz 2001). While some of the reports debated the nature of the primary

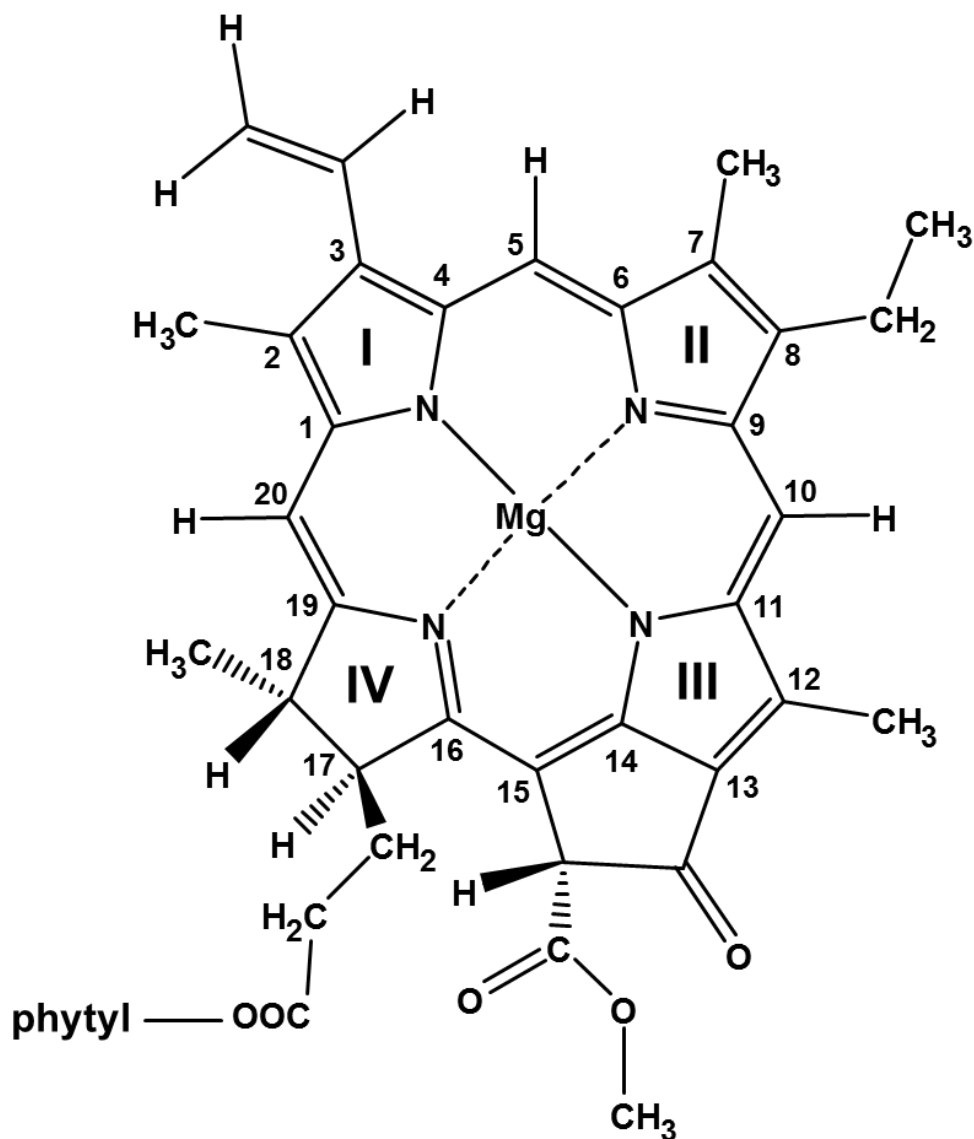
electron donor (Müller, Niklas et al. 2003; Holzwarth, Muller et al. 2006; Ptushenko, Cherepanov et al. 2008), it is the P₇₀₀ special pair that localizes the positive charge, thus stabilizing the charge-separated state required for the reduction of ferredoxin/flavodoxin proteins.

Given the central role P₇₀₀ plays in the redox activity of PSI, its chemical and electronic structures have been the focus of intense research for several decades (Webber and Lubitz 2001). We note that although the chemical composition P₇₀₀ as a Chl a/Chl a' coplanar heterodimer has been unambiguously confirmed by high resolution X-ray crystal structure of cyanobacterial PSI (Jordan, Fromme et al. 2001), the electronic structure of P₇₀₀ in its singlet, triplet, and radical states still remain a subject of much interest. Among the various spectroscopic methods employed to unravel the electronic structure of the primary donor, electron paramagnetic resonance spectroscopy (EPR) has been particularly useful due to the paramagnetic nature of both the triplet and the cation radical forms of P₇₀₀.

The triplet state ³P₇₀₀ is usually formed as a result of a charge recombination when the reduction of F_X and A₁ results in the electron transfer being blocked to continue beyond the first acceptor A₀ (Frank, McLean et al. 1979; Setif and Brettel 1990). At lower magnetic field/microwave frequency bands the EPR spectrum of ³P₇₀₀ is dominated by the zero field splitting (ZFS) interaction, mathematically described by the two parameters D and E. EPR characterization of ³P₇₀₀ has been primarily focused on measurements of these ZFS parameters (Budil and Thurnauer 1991) and their comparison with monomeric Chl a data (Den Blanken and Hoff 1983; Vrieze, Gast et al. 1996; Poluektov, Utschig et al. 2002). Unfortunately, up to this date no unambiguous conclusions could be reached regarding the electron spin density delocalization over the two monomeric chlorophylls of ³P₇₀₀. The available spectroscopic data for ³P₇₀₀ remain rather sparse and yield limited information on the electronic structure.

More extensive research of the electronic structure of P_{700} has been conducted using the cation radical form of the primary electron donor, $P_{700}^{+\bullet}$ (Webber and Lubitz 2001). Specifically, high frequency/ high field (HF) EPR studies of frozen solutions provided for an accurate determination of $P_{700}^{+\bullet}$ g-matrix principle components (Bratt, Rohrer et al. 1997) while orientation of the g-matrix with respect to the molecular frame has been derived from the single crystal studies (Zech, Hofbauer et al. 2000; Teutloff, Hofbauer et al. 2001). The magnitude of the g-matrix anisotropy of $P_{700}^{+\bullet}$ has been found to be nearly identical to that of the monomeric Chl a, indicating that most of the electron spin density is carried by one of the chlorophyll subunits. In contrast, unusual temperature dependence of the g-matrix is more consistent with the dimeric nature of $P_{700}^{+\bullet}$ (Bratt, Poluektov et al. 2000). HF EPR combined with site-directed mutagenesis pointed out that most of the spin density is carried out by P_B , the Chl a molecule located in the B branch of PSI (Petrenko, Maniero et al. 2004). Based on these studies, because of the complex interrelation between the g-matrix anisotropy and the distribution of the electron spin density, no final conclusions could be made with respect to the spin density delocalization over the two dimers.

In contrast to g-matrix data, isotropic components of the electron-nuclear hyperfine interaction directly represent the spin delocalization map of a paramagnetic molecule. In both Chl a (chemical structure is shown in the Scheme 1) and Chl a' the electron spin density can be probed by naturally abundant magnetic nuclei: various protons as well as four pyrrole ring ^{14}N nuclei commonly denoted as N_I - N_IV . Additionally, electron spin density could in principle be transferred partially to the two axial ligands, HisA_{680} and HisB_{660} , which are coordinating P_A and P_B respectively.



Scheme 2.1. Structure of the chlorophyll a (Chl a) with IUPAC numbering of molecular positions.

Previously, hyperfine interactions in $P_{700}^{\bullet+}$ have been studied by a number of EPR techniques (Webber and Lubitz 2001; Lubitz 2003) with electron nuclear double resonance (ENDOR) (Schweiger and Jeschke 2001) and electron spin echo envelop modulation (ESEEM) (Schweiger and Jeschke 2001) spectroscopies being among the most successful methods (Webber

and Lubitz 2001). However, the combination of the bulky conjugated π -system structure with an abundance of both types of magnetic nuclei has been the major obstacle to resolve the individual contributions of the P_A and P_B halves of the P_{700} heterodimer. Moreover, in frozen solutions, the spectral complexity dramatically worsens due to the orientational disorder, making spectral interpretation especially difficult and prone to errors. To this date, the most accurate measurements of hyperfine interactions in $P_{700}^{+\bullet}$ were obtained using single crystals of PSI measured at multiple orientations with respect to the external magnetic field (Käss, Fromme et al. 2001). Full hyperfine tensor parameters (principle values and orientation with respect to the molecular frame) were accurately measured for three types of methyl protons of the P_B molecule (Käss, Fromme et al. 2001). Based on the comparison with the monomeric Chl a, it was argued that at least 85% of the spin density is carried by P_B molecule (Käss, Fromme et al. 2001). On the other hand, some of the detected smaller hyperfine couplings were tentatively assigned to the second half of the dimer P_A , leading to estimates of the spin density distribution between the two halves as 75:25 to 70:30 (H. Käss, PhD thesis, Technische Universität Berlin, 1995). Single crystal samples were also used in an attempt to unravel hyperfine interactions with the available ^{14}N nuclei using ESEEM spectroscopy (Käß, Fromme et al. 1996). The single crystal samples allowed for accurate measurements of five types of nuclear quadrupole coupling parameters, providing indirect evidence of the electron spin density being carried by both P_A and P_B . However, the more valuable electron-nuclear couplings (regarding the structural information that could be obtained) remain unresolved even for the single crystals, owing to the extreme complexity of the measured ESEEM spectra (Käß, Fromme et al. 1996).

No unambiguous detection of any of the nuclei belonging to the P_A side has been achieved to this day, leaving the question of the dimeric vs. monomeric nature of the cation radical $P_{700}^{+\bullet}$ still

unsolved. Methods alternative to EPR, such as photo-CIDNP (Diller, Roy et al. 2007; Najdanova, Janssen et al. 2015) and FTIR (Breton, Nabedryk et al. 1999; Wang, Sivakumar et al. 2003) were unable to provide the clear answer either and resulted in contradictive models of $P_{700}^{+\bullet}$ ranging from a fully monomeric radical species to the equal contributions from the both chlorophylls P_A and P_B .

Here we report on multi-frequency (X- and Q-band) investigation of the electronic structure of $P_{700}^{+\bullet}$ in PSI from thermophilic cyanobacterium *Synechococcus elongatus* using hyperfine sublevel correlation (HYSCORE) spectroscopy (Höfer, Grupp et al. 1986). As a 2D-method, HYSCORE dramatically reduces the spectral crowding of the 1D techniques of ESEEM and ENDOR, thus, allowing for detection of ^{14}N hyperfine couplings with high resolution. Here we have chosen a combination of the 4-pulse (Höfer, Grupp et al. 1986) and 6-pulse sequences (Kasumaj and Stoll 2008) to extend the sensitivity range of the HYSCORE spectroscopy. Special attention is paid to distinguish the spectral contributions from weakly interacting nuclei from potential artifacts caused by experimental imperfections.

Section 2

Materials and Methods

2.1 Sample Preparation

Cultivation of *Thermosynechococcus elongatus* and membrane protein extraction were performed as reported previously (Kern, J. et al. Purification, characterisation and crystallisation of photosystem II from *Thermosynechococcus elongatus* cultivated in a new type of photobioreactor. *Biochimica et Biophysica Acta (BBA) - Bioenergetics* **1706**, 147-157 (2005). PSI was purified by a column packed with Toyo Pearl DEAE 650 S (GE Healthcare, Germany) where PSI was eluted at 20 mM MES-NaOH, pH 6.0, 5 % glycerol (v/v), 20 mM CaCl_2 and 0.02 % DDM

(w/v), 55 mM MgSO₄. The final PSI protein was in a buffer containing 20 mM MES-NaOH, pH 6.0, 5 % glycerol (v/v), 20 mM CaCl₂ and 0.02 % DDM (w/v), 60 mM MgSO₄.

2.2 EPR Spectroscopy

Pulsed EPR experiments have been carried out using ELEXSYS E580 spectrometer (Bruker Biospin, Billerica, MA, USA) equipped with a SuperQ-FT bridge for X (9 GHz) - and Q (35 GHz) - band experiments. Both X- and Q-band spectra have been acquired at 76 K using the Bruker ER 4118CF flow cryostat cooled with liquid nitrogen. We used the standard 16-step phase cycling procedure for the 4-pulse HYSCORE and the original 8-step phase cycling procedure (Kasumaj and Stoll 2008) for the 6-pulse HYSCORE.

2.2.1. X-band EPR

X-band $\pi/2$ (of 10 ns duration) and π (of 20 ns duration) microwave pulses at 9.67 GHz have been generated using an E-580–1030 1 kW TWT amplifier. Aqueous samples were drawn into 3 × 4 mm (i.d. × o.d.) quartz tubes (Wilma-LabGlass, Vineland, NJ, USA), frozen by immersing into liquid nitrogen, and rapidly transferred into a precooled ER 4118X-MD5W dielectric resonator. All HYSCORE spectra were measured at magnetic field of ca. 3,450 G corresponding to the maximum of the echo-detected field-swept spectra (see **Figure 2.1**).

Initial separation between the second and the third pulses (for 4-pulse HYSCORE), as well as between the third and the fourth pulse (for 6-pulse HYSCORE), was 24 ns. Initial separation between the third and the fourth pulses (for 4-pulse HYSCORE), as well as between the fourth and the fifth pulses (for 6-pulse HYSCORE), was 34 ns. The difference of 10 ns was applied to take into account the difference in length of the $\pi/2$ and π pulses. These pulse separations were incremented

by 16 ns to obtain experimental time domain spectra, consisting of (300×300] points. All other inter-pulse separations for both the 4-pulse and 6-pulse HYSCORE are provided in the main text.

2.2.2. Q-band EPR

Q-band $\pi/2$ (of 10 ns duration) and π (of 18 ns duration) microwave pulses at 33.801 GHz were generated using a 10 W AmpQ solid state amplifier. Aqueous samples were drawn into the standard 1.2 × 1.6 mm (i.d. × o.d.) quartz tubes (Wilmaad-LabGlass), frozen by immersing into liquid nitrogen, and rapidly transferred into a precooled Q-band EN 5107D2 resonator. All HYSCORE spectra were measured at magnetic field of ca. 1,205 G corresponding to the maximum of the echo detected field swept spectra.

Initial separation between the second and the third pulses (for 4-pulse HYSCORE), as well as between the third and the fourth pulse (for 6-pulse HYSCORE), was 22 ns. Initial separation between the third and the fourth pulses (for 4-pulse HYSCORE), as well as between the fourth and the fifth pulses (for 6-pulse HYSCORE), was 30 ns. The difference of 8 ns was applied to take into account the difference in length of $\pi/2$ and π pulses. These pulse separations were incremented by 16 ns to obtain experimental time domain spectrum consisting of 300 × 300 data points. All other inter-pulse separations for both 4-pulse and 6-pulse HYSCORE are blind-spot determining and are provided in the main text.

2.2.3. Signal processing and analysis of HYSCORE spectra

In order to obtain 2D frequency domain spectra, all the measured time domain data were processed in following steps: (1) 3-rd order polynomial was fitted and subtracted from the data in both dimensions as a 2D baseline, (2) a Hamming function was used to reduce the side lobe

artifacts: apodization was applied sequentially to each of the dimensions, (3) 2D time domain signal was zero filled to yield a 2048×2048 matrix, (4) time domain data were fast Fourier transformed, converted into the absolute values, symmetrized by taken an average with respect to the two matrix indices, and plotted using the “contour” function of the Matlab R2016a software (MathWorks, Natick, MA).

All the ^{14}N -HYSCORE spectra were simulated using Easyspin-5.2.20 software package (Stoll and Schweiger 2006) with Matlab R2016a. Estimates of the ^{14}N hyperfine parameters, as well as their approximate errors, have been determined by comparison of the locations and shapes of the (double quantum) - (double quantum) ridges of the simulated and the experimental spectra. As an approximation, electron-nuclear hyperfine tensor was assumed to be axial, i.e. two of the principal components were set to be equal. During the simulations the orientation of the electron-nuclear hyperfine tensor, defined by its principal values $[A_{xx}, A_{yy}, A_{zz}]$, was set to be parallel to the orientation of the traceless nuclear quadrupole tensor with principal values $[-K(1 - \eta), -K(1 + \eta), 2K]$. During the simulations, the direction of the axial electron-nuclear hyperfine component A_{\parallel} was interchanged between all three possible orientations, i.e., either $A_{\parallel} = A_{xx}$, $A_{\parallel} = A_{yy}$, or $A_{\parallel} = A_{zz}$, and the tensor orientation yielding the best agreement between the simulation and experiment has been chosen.

Proton hyperfine parameters were obtained from the ^1H -HYSCORE spectra using linear analysis procedure described in details previously (e.g., (Chatterjee, Milikisiyants et al. 2011)).

Section 3

Results and Discussion

3.1 Field Swept Echo-Detected EPR Spectra of $P_{700}^{+\bullet}$

X- and Q-band echo-detected field-swept spectra of the dark-adapted state of PSI from thermophilic cyanobacterium *Synechococcus elongatus* in the presence of 20 mM $K_3[Fe(CN)_6]$ are shown in **Figures 2.1A and B**, respectively. Both spectra correspond to a single unresolved EPR line centered at ca. $g \approx 2.0025$, in agreement with previous reports (Golbeck 1992). The observed ≈ 10 G (full width at half height) linewidth at X-band is slightly larger than ≈ 7 G measured by CW EPR (Golbeck 1992) due to an additional broadening caused by pulse excitation bandwidth. The field swept spectra confirm that the observed species are indeed $P_{700}^{+\bullet}$. Importantly, the measured echo-detected spectra are free of unwanted contributions, such as EPR-active A_0^- , A_1^- , and Fe^{3+} of ferricyanide, which would result in much broader EPR features (Srinivasan and Golbeck 2009). The contribution from Fe^{3+} ions, abundantly present in the sample, was not observed by pulsed EPR at liquid nitrogen temperatures due to very fast electron spin relaxation. Additionally, the presence of A_0^- and A_1^- are not expected at these experimental conditions (Käss, Fromme et al. 2001). Both X- and Q-band HYSCORE spectra were measured at the spectral maxima indicated by arrows in **Figure 2.1**.

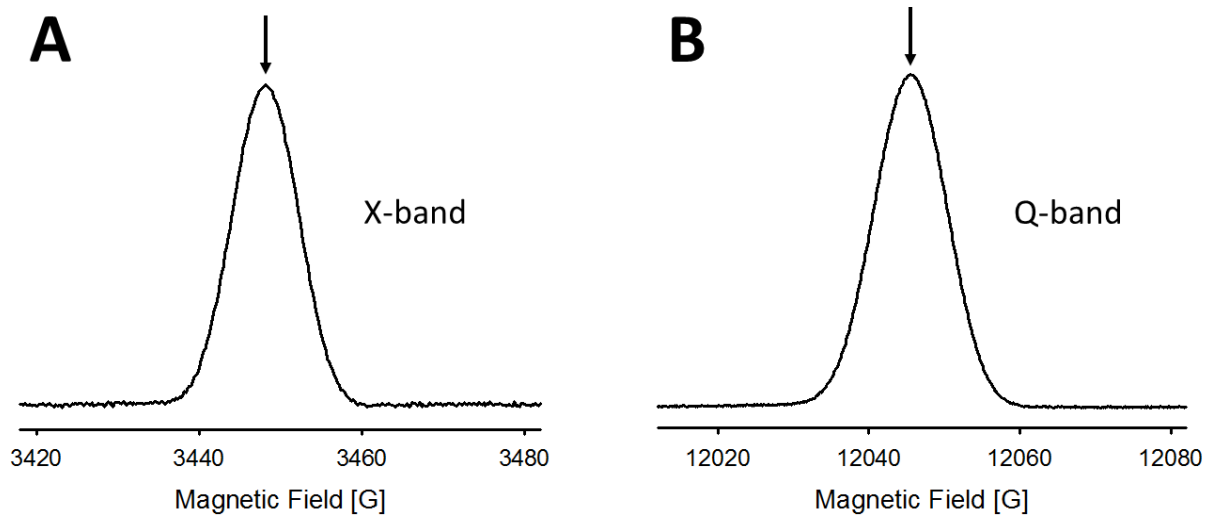


Figure 2.1. Echo-detected field-swept spectra of the primary electron donor $P_{700}^{+\bullet}$ in the oxidized state at X- (A) and Q-band (B) EPR frequencies. The arrows indicate the magnetic field positions for the respective HSCORE experiments.

3.2 X-Band 4-pulse HSCORE of $P_{700}^{+\bullet}$

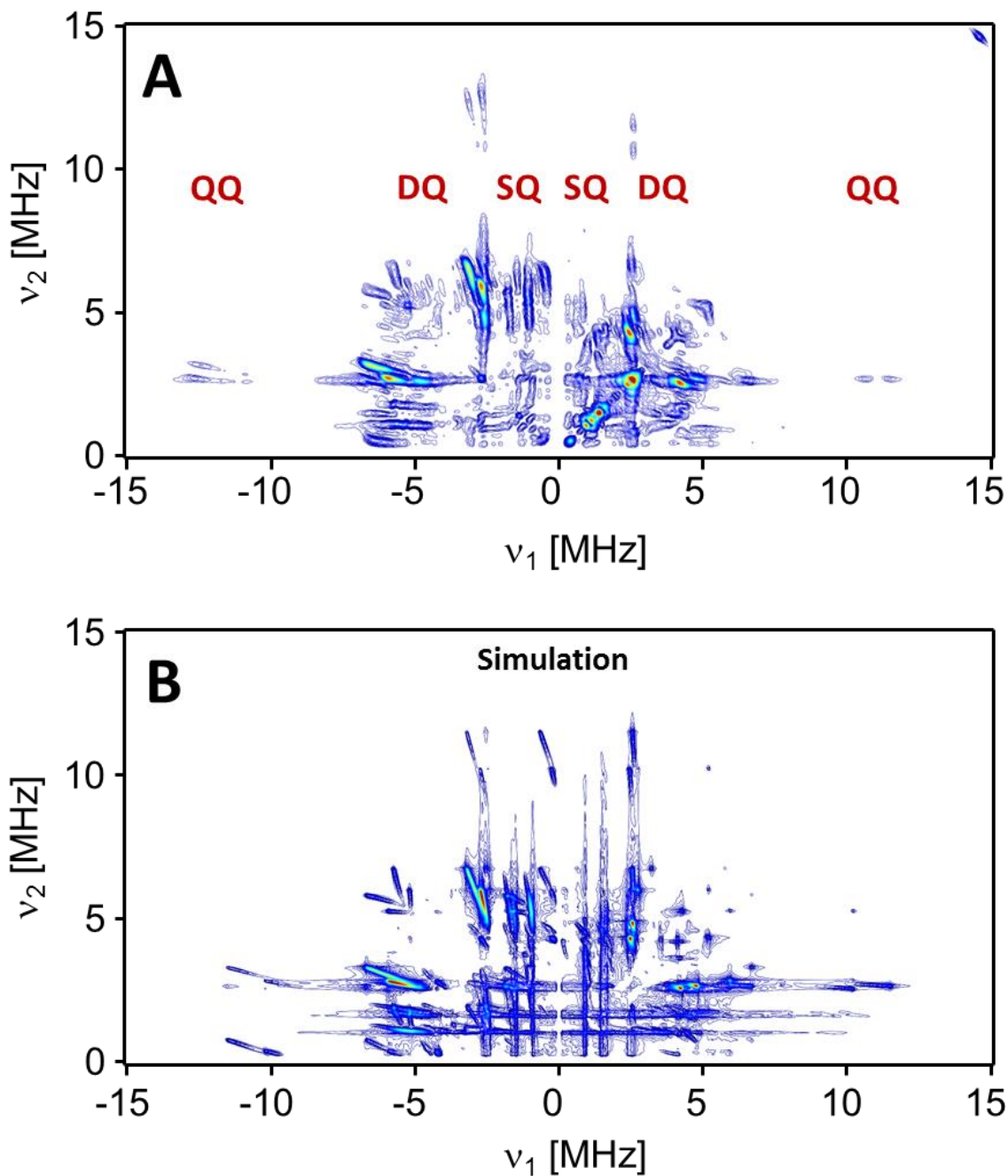


Figure 2.2. (A) Experimental X-band 4-pulse HSCORE spectrum of $P_{700}^{+\bullet}$ measured at a delay of 120 ns between the first ($\pi/2$) and the second ($\pi/2$) microwave pulses. Spectral regions corresponding to multi-quantum nuclear transitions are denoted with red text. (B) Simulated 4-pulse HSCORE spectrum yielding the best agreement with the experimental spectrum.

The (+,+) and (-,+) quadrants of the 4-pulse HYSCORE spectrum of $P_{700}^{+\bullet}$ measured at X-band are shown in **Figure 2.2A**. The delay between the first ($\pi/2$) and second ($\pi/2$) pulses was 120 ns, which corresponds to the blind spots appearing at $n \times 8.3$ MHz with n being a positive integer ($n=0, 1, 2\dots$). To ensure that no additional signals are hidden due to these blind spots, 4-pulse HYSCORE spectra with 100 ns (blind spots at $n \times 10$ MHz) and 140 ns (blind spots at $n \times 7.1$ MHz) delays between the first and second pulses were also measured (not shown).

The spectrum (**Figure 2.2A**) exhibits a rather complex pattern composed of features arising from multiple ^{14}N nuclei and a single unresolved low intensity feature at (14.7, 14.7) MHz due to ^1H . The observed features correspond to the cross-correlation peaks (cross-peaks) of the single quantum (SQ), double quantum (DQ), and quadruple quantum (QQ) nuclear transitions. The location of each individual cross-peak depends on the relative orientation of the external magnetic field with respect to the molecular frame. In frozen solutions, in which molecular orientations are randomly distributed, the cross-peaks form 2D patterns, commonly called HYSCORE ridges. The spectral regions approximately corresponding to SQ, DQ, and QQ transition frequencies are denoted in **Figure 2.2A**. The complex spectral pattern consists of ridges corresponding to correlations of various quantum transitions (e.g., SQ-SQ, SQ-DQ, DQ-DQ, etc.), as well as some of their combination peaks. The combination peaks arise mainly from factorization of the HYSCORE signal in the case of a simultaneous interaction of an unpaired electron spin with more than one magnetic nuclei. In addition, non-correlated features (pseudo 2D cross-peaks) located on the main diagonals ($\nu_1 = \nu_2$ for the (+,+) quadrant and $\nu_1 = -\nu_2$ for the (-,+) quadrant) are caused mainly by incomplete inversion of the spins by the third π -pulse, are also observed in the spectrum. The incomplete inversion by the π -pulse (estimated efficiency of $\approx 70\%$) causes the 3-pulse ESEEM signal to “leak” into the detected 2D time domain signal. The effective time coordinate of

the 3-pulse ESEEM is equal to the sum of the two HYSCORE time coordinates resulting in a peaks appearing on the main diagonals. The sharp non-correlated signals correspond to the ν_0 , ν_- , ν_+ , and ν_{DQ} peaks dominating a 1D 3-pulse ^{14}N -ESEEM spectrum at the so called “cancellation condition”, i.e. when the strength of the electron nuclear hyperfine interaction is about twice of the ^{14}N Larmor frequency ($A \sim 2\nu_I$) (Flanagan and Singel 1987; Deligiannakis, Louloudi et al. 2000). At exactly the “cancellation condition” ($A = 2\nu_I$) the spectral position of the peaks is determined by only quadrupole interaction parameters K and η : $\nu_0 = 2K\eta$, $\nu_- = 3K(1 - \eta)$, $\nu_+ = 3K(1 + \eta)$ and $\nu_{DQ} = 2K(3 + \eta^2)$ (Deligiannakis, Louloudi et al. 2000). Being the pseudo 2D peaks, they have the coordinates (ν_0, ν_0) , (ν_-, ν_-) , (ν_+, ν_+) and (ν_{DQ}, ν_{DQ}) , respectively. These non-correlated 3-pulse ESEEM peaks, together with the ridges corresponding to the DQ-DQ transitions, are the most intense features in the crowded HYSCORE spectrum. These spectral features corresponding to correlated and non-correlated signals become the most pronounced for different reasons. If the “cancellation condition” is fulfilled for a ^{14}N nucleus, 3-pulse signal intensity increases dramatically, resulting in an intense sharp peaks at the ν_0 , ν_- , ν_+ frequencies, corresponding to single quantum, and a lesser intense and broader peak at ν_{DQ} , corresponding to a double quantum transitions within the electron spin manifold at which the electron-nuclear and nuclear Zeeman interactions cancel each other. These peaks are usually so intense that even a small fraction of the “leaked” 3-pulse ESEEM signal would cause the corresponding HYSCORE features to be highly pronounced. As for the cross-correlated DQ-DQ ridges, the reason for their more pronounced intensity is the weak orientation dependence of the spectral position of the corresponding cross-peaks, which are approximately determined by the following equations (Dikanov, Xun et al. 1996):

$$v_1^{DQ} = \pm 2\sqrt{(v_l + A/2)^2 + K^2(3 + \eta^2)}, v_2^{DQ} = \pm 2\sqrt{(v_l - A/2)^2 + K^2(3 + \eta^2)} \quad (1)$$

where the + or - signs are determined by the quadrants in which the transition peaks appear.

While the spectral complexity makes unambiguous interpretation of the observed HYSCORE a difficult task, the spectral location of the non-correlated 3-pulse ESEEM features, and especially the DQ-DQ ridges, provide the valuable information about the structure of the spectrum.

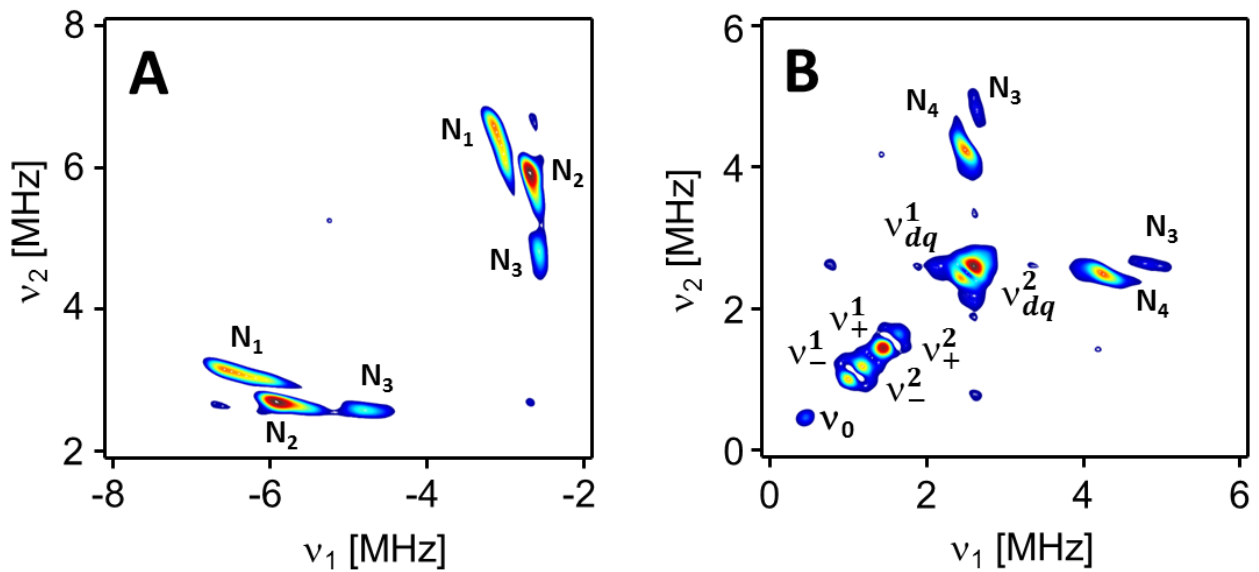


Figure 2.3. Selected regions of the experimental X-band HYSCORE spectrum shown in **Figure 2.2A** corresponding to the DQ and SQ spectral features. (A) Zoomed (-,+) quadrant region with DQ-DQ ridges of N_1 - N_3 . (B) Zoomed (+,+) region with DQ-DQ and 3-pulse ESEEM ridges of N_3 - N_4 .

Figure 2.3A-B selectively shows DQ-DQ and 3-pulse ESEEM features by using a higher minimal level in the contour map, removing nearly all other spectral contributions. At least three types of DQ-DQ ridges are clearly resolved in the (-,+) and two in the (+,+) quadrant. Seven 3-

pulse ESEEM features denoted as $\nu_0, \nu_-^1, \nu_-^2, \nu_+^1, \nu_+^2, \nu_{DQ}^1$ and ν_{DQ}^2 are resolved on the main diagonal of the (+,+) quadrant. Using equations (1), initial estimates of the hyperfine parameters A, K and η was made for each of the resolved DQ ridges. While electron-nuclear coupling A may vary significantly ($\sim 1-5$ MHz), the quadrupole tensor parameters of all the observed ^{14}N nuclei must be very similar. We interpret the observed spectrum as a superposition of contributions of four different ^{14}N nuclei: N_1, N_2, N_3 and N_4 . DQ-DQ ridges of N_1 and N_2 appear only in the (-,+) quadrant indicating their electron-nuclear couplings to be bigger than the double of the nuclear Larmor frequency, $A > 2\nu_I$. On the contrary, DQ-DQ ridges of N_4 are only observed in the (+,+) quadrant indicating the opposite, $A < 2\nu_I$. Only N_3 has pronounced DQ-DQ intensity on both quadrant indicating $A \sim 2\nu_I$. Seven 3-pulse ESEEM features indicate two types of the quadrupole couplings having (nearly) identical value of K and η . The 3-pulse features are most probably due to N_3 and N_4 , since, to the authors experience, no significant 3-pulse ESEEM features (except sometimes the (ν_{DQ}, ν_{DQ}) feature) are observed in the HYSORE spectrum for the case of $A > 2\nu_I$ (i.e., whenever the DQ-DQ features appear only in the (-,+) quadrant).

The spectral location of the observed DQ-DQ ridges and the diagonal features all point to close similarities between the quadrupole parameters of all the observed ^{14}N nuclei. This similarity of the quadrupole couplings increases spectral crowding and leads to a potential ambiguity of the spectral interpretation. Thus, extra care must be taken to avoid the possibility that (i) any of the observed DQ-DQ ridges may be experimental artifacts or (ii) originate from the same ^{14}N nucleus, as is the case for N_3 . The first (i) possibility was ruled out by measuring multiple HYSORE spectra with different inter-pulse delays and also by using a 6-pulse version of the HYSORE pulse sequence (see the section below). In all the cases, the same spectroscopic pattern consisting of 5 DQ-DQ ridges was observed. The second (ii) possibility was ruled out by numerical

simulations of the ^{14}N -HYSCORE spectrum. **Figure 2.2B** shows a simulated 4-pulse HYSCORE spectrum assuming four different ^{14}N nuclei contributing to the spectrum and the axial character of their electron-nuclear couplings (see Materials and Methods section). Obtained hyperfine parameters with $A_{\parallel} = A_{xx}$ and $A_{\perp} = A_{yy} = A_{zz}$ and error estimates are listed in Table 1. A reasonably good agreement between the experimental and the simulated spectra was achieved. Positions of the DQ-DQ ridges were reproduced with high accuracy while the exact shape of the ridges in the experimental spectrum was clearly affected by the pulse imperfections, which were not considered in the numerical simulations. The only significant deviation was the signal intensity distribution among the N_3 DQ-DQ ridges located in the $(-,+)$ and $(+,+)$ quadrants. To the authors' experience, similar deviations are typical for the case of $A \sim 2\nu_1$: pulse imperfections usually result in a notable "intensity shift" towards the $(-,+)$ quadrant as compared to numerical calculations. Interestingly, the experimental spectrum could only be reproduced with a satisfactory agreement if all the electron-nuclear hyperfine tensors (i.e., all their axial axes) were set to be mutually parallel. This seems reasonable, since the major fraction of the electron spin density must be delocalized over the π -orbitals of the two coupled Chl a and Chl a' molecules.

No other DQ-DQ ^{14}N ridges could be unambiguously detected in any of the measured 4-pulse HYSCORE spectra. If any strongly interacting ^{14}N was present in the spectrum, their approximate location would be determined by eq. (1) with the quadrupole parameters most likely close to those of N_1 - N_4 , since such a strong hyperfine interaction would only be possible for the Chl a or Chl a' pyrrole ring nitrogen. We can confidently exclude a possibility of another ^{14}N nucleus interacting stronger than N_1 - N_4 because the spectral space at the potential location of the corresponding DQ-DQ ridges is "clean" (i.e., free of other contributions except some random noise). The intensities of the DQ-DQ ridges drop gradually with the size of A ; thus, to escape the

detection, the size of A must be very large, presumably >10 MHz. If such a large hyperfine coupling were present, this would clearly contradict the well-known narrow line width of the CW-EPR spectrum (≈ 7 G according to (Golbeck 1992)). Moreover, no ^{14}N interacting stronger than N_1 was observed in the Q-band HYSCORE spectra (see the discussion and figures below), where the condition of the Larmor frequency being about threefold of that at X-band favors the detection of such nuclei.

For ^{14}N nuclei interacting weaker than N_4 , the spectral resolution problem is significantly more complex. The intensities of the DQ-DQ ridges drop rapidly with decrease in A. The spectral region where the potential DQ-DQ cross-peaks from such a weakly interacting ^{14}N could be detected is very crowded by the side lobes of the very intense DQ-DQ ridges of N_3 and N_4 as well as a rather complex pattern made of numerous combination peaks. Thus, detection of such weakly coupled nuclei would require an application of a method more sensitive to the weakly coupled nuclei than the standard 4-pulse HYSCORE sequence.

3.3. X-Band 6-pulse HSCORE of $P_{700}^{+\bullet}$

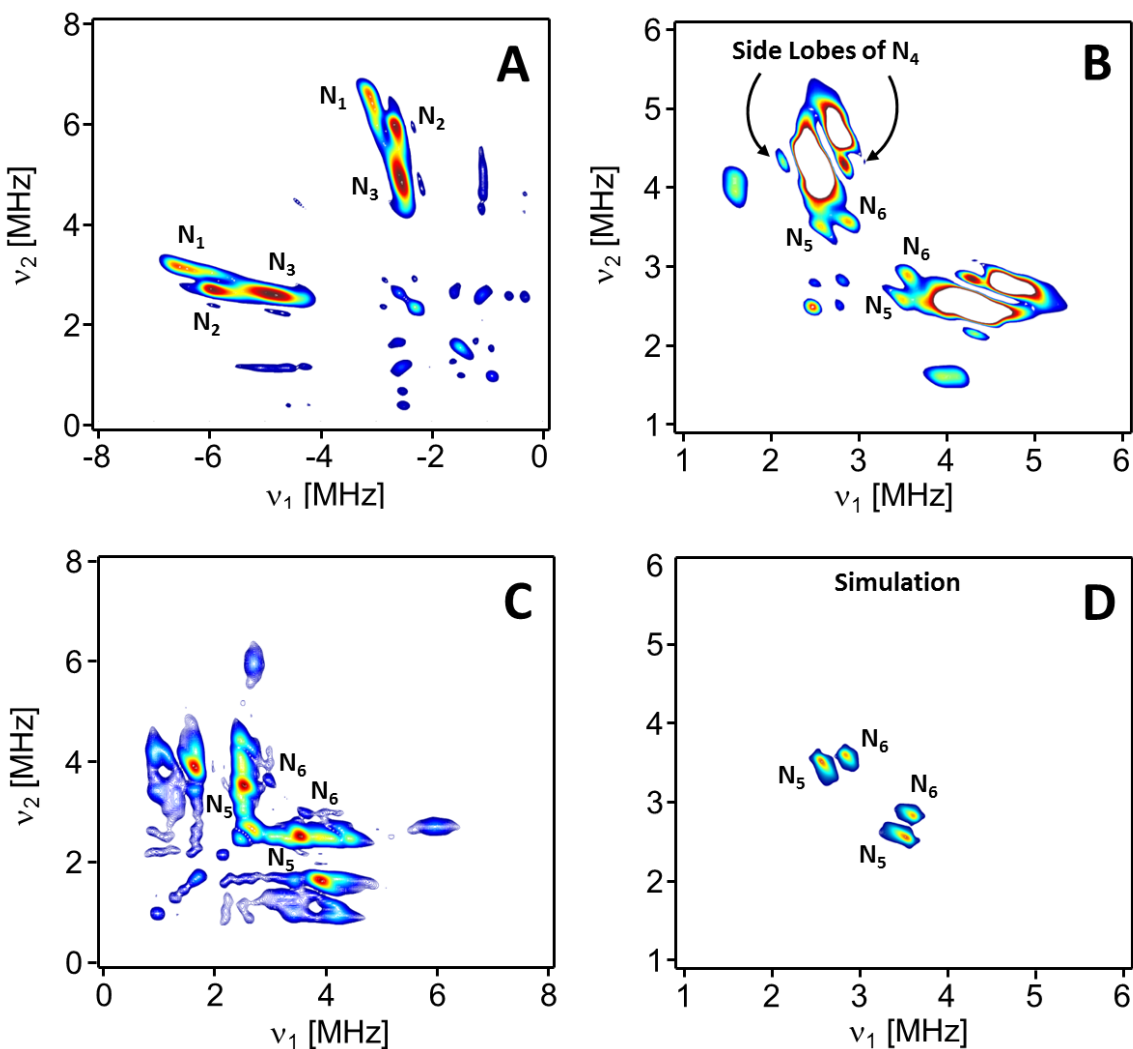


Figure 2.4. Selected region of the (-,+) quadrant (A) and (+,+) quadrant (B) of X-band 6-pulse HSCORE spectrum of $P_{700}^{+\bullet}$ measured with an inter-pulse delays of 68 ns and 120 ns between the first two and the last two microwave pulses, respectively. (C) Selected region of the (+,+) quadrant of the X-band 6-pulse HSCORE spectrum of $P_{700}^{+\bullet}$ measured with an inter-pulse delays of 68 ns and 234 ns between the first two and the last two microwave pulses, respectively. (D) Simulated HSCORE spectrum of N_5 and N_6 nuclei.

To search for potentially missing weakly interacting ^{14}N nuclei, we measured 6-pulse HYSCORE spectra of the $\text{P}_{700}^{+\bullet}$ radical. 6-pulse HYSCORE has much higher sensitivity towards weaker hyperfine couplings and is significantly less prone to yield unwanted combination peaks (Kasumaj and Stoll 2008). **Figure 2.4A-B** shows selected ranges of the (-,+) and (+,+) quadrants of the 6-pulse HYSCORE spectrum of $\text{P}_{700}^{+\bullet}$ measured with an inter-pulse delays of 68 ns (blind spots at $n \times 14.7$ MHz, $n=0,1,2\dots$) and 120 ns (blind spots at $n \times 8.3$ MHz, $n=0,1,2\dots$) between the first two and the last two microwave pulses, respectively. To avoid a loss of spectral information due to the blind-spot effects, two additional 6-pulse HYSCORE spectra with corresponding inter-pulse delays of 68 ns and 140 ns (blind spots at $n \times 7.1$ MHz, $n=0,1,2\dots$; not shown) and 68 ns 234 ns (blind spots at $n \times 4.3$ MHz, $n=0,1,2\dots$), respectively, were also measured. (The low frequency region of the (+,+) quadrant of the latter spectrum is shown in **Figure 2.4C** and discussed below.) All the DQ-DQ ridges observed by 4-pulse HYSCORE spectroscopy are clearly resolved in the 6-pulse HYSCORE spectra. As expected, compared to 4-pulse HYSCORE, a strong suppression effect on the 3-pulse ESEEM diagonal features located in the main diagonal was observed. Such suppression significantly reduced the “crowding” around the spectral area where the DQ-DQ ridges of weakly interacting ^{14}N are expected. In contrast to the 4-pulse HYSCORE, two additional pairs of spectral features are clearly detected and resolved by the 6-pulse HYSCORE. We assign these two pairs of features to two weakly interacting ^{14}N nuclei, N_5 and N_6 . Due to small intensity of the spectral features, extra care was taken with respect to the assignment of these signals to two “new” ^{14}N nuclei. Four alternative possibilities were rigorously considered: (i) the features are random noise or pulse imperfections artifacts, (ii) any of the four features represent a combination of other peaks in the spectrum, (iii) the features do not

correspond to DQ-DQ transitions, and (iv) the features are side-lobe artifacts of much more intense DQ-DQ ridges of N_3 and N_4 nuclei.

The first possibility (i) could be reliably excluded, since all the four features are clearly detected in the non-symmetrized spectrum, and, more importantly, are well reproduced in the 6-pulse HYSORE spectrum measured with 140 ns inter-pulse delays between the last two pulses. Thus, a random (noise) nature of the features could safely be excluded. The second possibility (ii) requires the presence of at least two rather intense additional cross-peaks for each feature having at least one of the frequency coordinates identical to those of the corresponding feature. No such or even similar cross-peaks were detected. Furthermore (iii), being located in the DQ-DQ region, the observed features cannot be attributed to SQ or higher than DQ N_1 - N_4 transitions. To confirm this, we were unable to reproduce such features by numerical calculations assuming only contributions of N_1 - N_4 transitions with any reasonable set of the hyperfine parameters. The last possibility (iv) could be ruled out for the features assigned to the N_6 , since the side-lobes in the HYSORE spectrum appear as multiple, rapidly decaying images of the main signal, shifted perfectly parallel along one of the frequency axes. At least two side-lobes of the intense N_4 DQ-DQ ridge along the first frequency axis are clearly seen in the spectrum shown in **Figure 2.4B**. Features assigned to N_5 appear shifted from the DQ-DQ ridges of N_4 towards lower frequencies approximately parallel to the second frequency axis, indicating a possibility of N_5 features could be the side-lobes of the DQ-DQ ridges of N_4 . To discriminate between these two possibilities, a 6-pulse HYSORE spectrum with 234 ns delay between the last two pulses has been measured. For such a delay, the lowest frequency blind-spot appears at the location of the N_4 DQ-DQ ridges, causing a nearly complete suppression of their intensity. The corresponding spectral region of the (+,+) quadrant of the measured spectrum is shown in the **Figure 2.4C**. While the overall intensity

of all the spectral features decreased significantly, the N₅ ridges became the most pronounced signals in the spectral region, clearly rejecting the possibility of the features being the side lobes or induced by other imperfections originating from the signal processing of the N₄. Unfortunately, due to the significantly increased effect of the pulse imperfections, as well as partial intensity suppression due to proximity to the blind spot, the intensity of the N₆ ridges became comparable to that of the noise artifacts. Thus, preventing their clear and unambiguous detection using this extended delay (234 ns) between the last two pulses.

As for the case of N₁-N₄, numerical simulations were employed to estimate the hyperfine interaction parameters of N₅ and N₆. In the simulations, only N₅ and N₆ were taken into consideration, while all the interactions with N₁-N₄ were omitted for the sake of simplicity. The set of hyperfine parameters providing the best agreement with the experimental spectrum (**Figure 2.4B**) is given in Table 1. The corresponding simulated spectrum is shown in **Figure 2.4D**. As expected, while electron-nuclear couplings are much weaker for N₅ and N₆ as compared to N₁-N₄, their quadrupole tensor parameters are very similar to those of N₁-N₄, indicating identical covalent bond structure around all the observed nitrogen nuclei.

The quadrupole and electron-nuclear hyperfine parameters of Table 1 agree well with those obtained previously for single crystals of PSI using 1D ESEEM spectroscopy (Käβ, Fromme et al. 1996). Specifically, Kass et al. resolved five distinct ¹⁴N nuclei having very similar quadrupole parameters, with K and η being in the range of 0.63-0.75 MHz and 0.73-0.83, respectively. Within the experimental errors, these values measured for the single crystal are identical to those in Table 1 measured in this work for the frozen solution of PSI. Due to insufficient resolution inherent of the 1D nature of 3-pulse ESEEM, only the upper limit for the electron-nuclear hyperfine coupling components were estimated from the single crystal spectra (Käβ, Fromme et al. 1996). We note

that the upper limit of 4.3 ± 0.1 MHz obtained from ESEEM spectra also agrees well with the highest value 4.1 ± 0.2 of Table 1 (A_{\parallel} of N_1) we measured by HYSORE.

While the 6-pulse HYSORE has superior sensitivity towards much weaker ^{14}N (despite of a significantly smaller electron spin echo signal and a significantly increased effect of pulse imperfections), it also provides better resolved signals from ^1H nuclei. **Figure 2.5A** shows proton cross correlation signals of the 6-pulse HYSORE spectrum measured with 68 ns inter-pulse separation between the first two pulses and 120 ns inter-pulse delay between the last two pulses (corresponding ^{14}N signals are shown in the **Figure 2.4A-B**). Besides the intense unresolved feature centered at the main diagonal and corresponding to multiple overlapping matrices and other weakly coupled ^1H nuclei, two pairs of the ridges corresponding to the two types H_1 and H_2 of stronger coupled protons are observed. The ridges have a large separation within each pair, but their lengths and deviations from the anti-diagonal defined by $\nu_1 + \nu_2 = 2\nu_1$ ($\nu_1=14.7$ MHz, the proton Larmor frequency) are small, indicating a large electron-nuclear coupling with relatively small anisotropy. H_1 and H_2 hyperfine interaction parameters obtained using linear analysis (see “Materials and Methods” section for details) are shown in Table 1.

Table 1. ^{14}N and ^1H hyperfine interaction parameters of $\text{P}_{700}^{+\bullet}$ obtained from experimental HYSCORE spectra.

	$\{A_{\parallel}, A_{\perp}\}$, MHz	K, MHz	η
N_1	$\{4.1\pm 0.2, 2.1\pm 0.6\}$	0.70 ± 0.05	0.65 ± 0.25
N_2	$\{3.4\pm 0.2, 1.8\pm 0.5\}$	0.65 ± 0.05	0.70 ± 0.25
N_3	$\{1.9\pm 0.1, 1.2\pm 0.3\}$	0.70 ± 0.05	0.65 ± 0.25
N_4	$\{1.5\pm 0.1, 1.0\pm 0.2\}$	0.65 ± 0.05	0.70 ± 0.25
N_5	$\{0.77\pm 0.05, 0.32\pm 0.1\}$	0.55 ± 0.05	0.85 ± 0.15
N_6	$\{0.64\pm 0.05, 0.35\pm 0.1\}$	0.62 ± 0.05	0.80 ± 0.2
H_1	$\{9.9\pm 0.5, 6.6\pm 0.5\}$	-	-
H_2	$\{8.3\pm 0.4, 5.2\pm 0.4\}$	-	-

Assignment of H_1 and H_2 in HYSCORE spectra were made based on a comparison with previously reported ENDOR measurements of $\text{P}_{700}^{+\bullet}$ in frozen solution (Käss, Fromme et al. 2001). In the latter study, hyperfine splittings of 9.6 MHz and 7.7 MHz were observed and assigned to either A_{\parallel} or A_{\perp} hyperfine components of the \square -protons on the ring IV at positions 17 or 18 (see Scheme 1). Thus, we tentatively assign H_1 and H_2 to either of the \square -protons.

3.4 Q-Band HYSCORE of $\text{P}_{700}^{+\bullet}$

As a test of the interpretation of the X-band (9.7 GHz) ^{14}N -HYSCORE described above, 4-pulse and 6-pulse HYSCORE spectra of $\text{P}_{700}^{+\bullet}$ radical were measured at Q-band (33.8 GHz) EPR frequency. The (+,+) quadrant of the 4-pulse spectrum measured using 140 ns separation between the first two pulses is shown in **Figure 2.5B**. No cross-correlated signals were detected in the (-,+) quadrant. Compared to X-band, the Q-band spectrum is much “cleaner”: it consists of

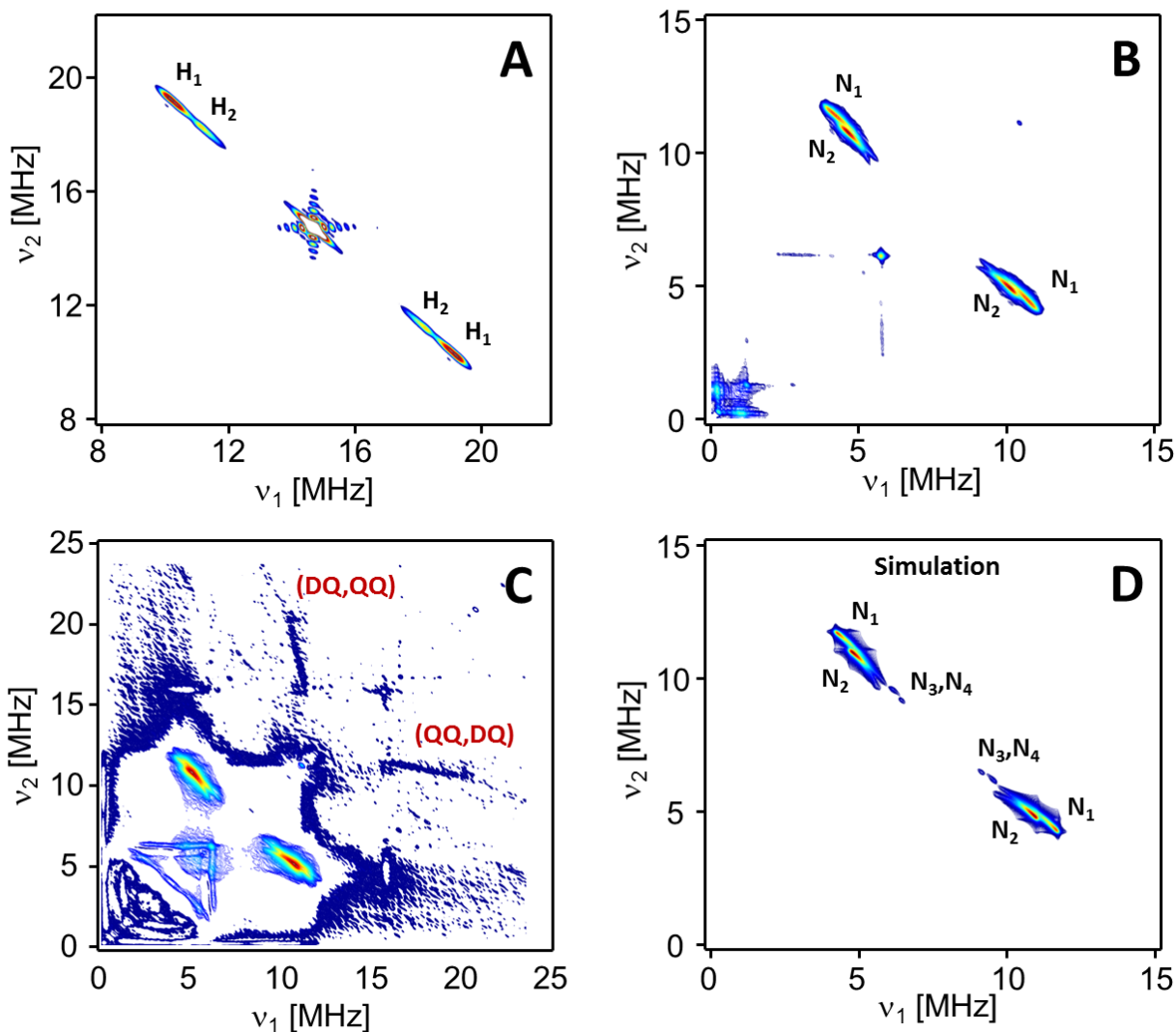


Figure 2.5. (A) X-band ^1H -HYSCORE spectrum obtained using 6-pulse sequence with 68 ns inter-pulse separation between the first two pulses and 120 ns inter-pulse delay between the last two pulses. (B) (+,+) quadrant of 4-pulse Q-band HYSCORE spectrum obtained with 140 ns separation between the first two pulses. (C) (+,+) quadrant of Q-band 6-pulse HYSCORE spectrum obtained with 68 ns inter-pulse separation between the first two pulses and 140 ns inter-pulse delay between the last two pulses (D) Simulated Q-band 4-pulse HYSCORE spectrum of N_1 - N_4 nuclei. Contributions from N_5 and N_6 were neglected.

two partially overlapping pairs of the DQ-DQ ridges, one diagonal peak corresponding to 3-pulse ESEEM frequency ν_{DQ} , barely detectable SQ-DQ ridges, and low frequency (<2 MHz) artifacts, presumably caused by remaining imperfections of the baseline subtraction during the signal post processing. For comparison, the simulated spectrum using the hyperfine parameters listed in Table 1 is shown in **Figure 2.5D**. Experimental ridges, corresponding to N_1 and N_2 , are reproduced well in the simulated spectrum, thus, confirming the validity of their assignment and the accuracy of the estimated hyperfine values. No resolved cross-peaks from N_3 - N_6 could be observed in the experimental spectrum. While N_5 and N_6 are not expected to appear in the experimental spectrum, simulations predict the intensity of the DQ-DQ ridges of the stronger interacting N_3 and N_4 to reduce by an order of magnitude compared to those of N_1 and N_2 , but still to be above the detection limit of the experiment. At this point we may only suggest that in the actual Q-band experiment the intensity of the DQ-DQ peaks reduces more with decrease of hyperfine coupling than in simulations where microwave pulses is assumed to have ideal excitations. Another possibility is a more pronounced destructive interference effect (Dikanov, Tyryshkin et al. 2000) in the experimental spectrum due to non-zero initial inter-pulse separations, corresponding to the two time coordinates of the HYSORE experiment.

As an attempt to recover peaks corresponding to weaker hyperfine couplings, a 6-pulse Q-band HYSORE spectrum was measured. The spectrum plotted using unevenly distributed contour levels density is shown in **Figure 2.5C**. The contour levels were chosen to make the very low intensity features well pronounced: for the low intensity signals (below 5% of the maximal intensity), the density of the contour levels was chosen to be 100-fold higher than for the rest of the spectrum. This uneven contour level distribution permitted for the best visual representation of the spectral features with very low intensities while avoiding the dramatic overcrowding around

more intense signals. Unfortunately, no peaks from any of the N₃-N₆ were recovered by applying the 6-pulse sequence. However, partially resolved DQ-QQ peaks of N₁ and N₂ were observed. QQ frequency corresponds to simultaneous DQ transitions of the two ¹⁴N nuclei. As can be seen in the **Figure 2.5C**, an extension of the DQ-QQ peaks is clearly longer than those of the DQ-DQ ridges. This supports (Liesum and Schweiger 2001) the hypothesis that the axial symmetry axis of the hyperfine tensors of at least N₁ and N₂ are (approximately) collinear, in agreement with the hyperfine parameters listed in **Table 1**.

3.5. Spin density distribution in P₇₀₀⁺•

It is important to note here that an experimental investigation of the electronic structure of P₇₀₀⁺• using magnetic resonance spectroscopy, while uniquely informative, is an extremely difficult task due to an abundance of the nuclei magnetically coupled to the unpaired electron of the radical due to a strong delocalization of the electron spin density over the two coupled chlorophylls and, potentially, even the surrounding amino acids. While similar complexity has been successfully resolved for the P₈₆₅⁺• primary donor cation radical in *Rhodospseudomonas sphaeroides* R-26 reaction center (Lendzian, Huber et al. 1993), as well as for P₉₆₀⁺• in *Rhodospseudomonas viridis* (Webber and Lubitz 2001), no unambiguous estimates of the electron spin density distribution among P_A and P_B has been successfully achieved so far for P₇₀₀⁺•. Earlier studies using ENDOR and ESEEM have only provided rather tentative evidence of the electron spin delocalization over the two halves of the special pair.

Unambiguous assignment of the obtained ¹⁴N hyperfine couplings does not seem feasible using only frozen solution experimental data, as it would require orientation-resolved single crystal data. A detailed HYSORE study of a model Chl a radical could potentially provide another set

of useful information. Nevertheless, some important conclusions with respect to the electronic structure of the $P_{700}^{+\bullet}$ radical were made based on the experimental data presented here. First, all the observed N_1 - N_6 nuclei were tentatively assigned to six pyrrole ring nitrogen atoms of the coupled Chl a and Chl a'. There are two solid reasons to favor this assignment. (i) All the quadrupole interaction parameters of N_1 - N_6 are very similar, with subtle differences within experimental and/or numerical simulation errors. The close similarity between the six quadrupole couplings is rather obvious, even based on a simple visual inspection of the spectra shown in **Figures 2.2-5**, since within small deviations, all the observed DQ-DQ ridges are located in the proximity of the same curve determined by the equations (1), where A is considered as a variable and K , η as fixed parameters. The close similarity of the quadrupole couplings strongly indicates close similarity/identity of the chemical bonding structure involving all the observed ^{14}N , since quadrupole interaction being induced by electric field gradient is very sensitive to the local electronic structure around an interacting magnetic nucleus. (ii) The only alternative assignment would be to any of the amino nitrogens belonging to the two histidine ligands, namely His A680 and/or His B660. This is, however, not probable from a theoretical perspective as no significant electron spin density will be transferred to neither of the His A680 and His B660 residues (Plato, Krauss et al. 2003). Thus, we may reasonably assign N_1 - N_6 to be six pyrrole ring nitrogen atoms belonging to Chl a and Chl a' moieties of the $P_{700}^{+\bullet}$ radical.

Additionally, six non-equivalent ^{14}N pyrrole ring observed by HYSCORE indicates immediately the dimeric nature of the P_{700} donor with a clearly asymmetric electron spin density distribution, and, thus, an asymmetric electronic structure of the two halves of the $P_{700}^{+\bullet}$ radical, since only four different nitrogens at most could be from the same chlorophyll molecule. Furthermore, the overwhelming experimental and theoretical data (Webber and Lubitz 2001) all

point to P_B carrying more spin density than P_A. While quantification of the degree of asymmetry defined by a so-called asymmetry factor $R_{B/A}$ requires an exact assignment of the hyperfine couplings, some conclusions about its upper limit could be deduced in this study. For the highest asymmetry case, the four largest hyperfine couplings would belong to the same chlorophyll dimer half and the two smallest to the other. In this case, the degree of asymmetry could be estimated by a ratio of the two largest and two smallest hyperfine couplings. We would expect that an estimate using just the axial hyperfine component A_{\parallel} would be more accurate than based on the isotropic value $A_{\text{iso}} = (A_{\parallel} + 2A_{\perp})/3$ because the experimental errors for the perpendicular components A_{\perp} are significantly higher than those for A_{\parallel} . Thus, based on A_{\parallel} values, the upper limit of the asymmetry factor is estimated as $R_{B/A}^{\text{upper}} \approx 5.3$; i.e., the ratio of the electron spin density of P_B and P_A is $\approx 5.3:1$. If the isotropic couplings A_{iso} are considered, the value of the asymmetry factor rises slightly to $R_{B/A}^{\text{upper}} \approx 5.5$. Such high asymmetry is very close to $R_{B/A} \approx 5.7$ estimated in earlier works using ENDOR and TRIPLE resonance (Käss, Fromme et al. 2001).

No reliable estimation of the lower limit for the asymmetry parameter $R_{B/A}^{\text{lower}}$ could be made based on the data obtained in this work. This is because the spin density distribution patterns could in principle be completely different in Chl a and Chl a' leading to $8!/2 = 20,160$ theoretically possible assignments (only half of them corresponding to $R_{B/A} \geq 1$). Given the size of the experimental errors (shown in Table 1), $R_{B/A}^{\text{lower}}$ could be as small as 0. Negative $R_{B/A}^{\text{lower}}$ should be rejected as it would lead to inverted asymmetry not supported by the overwhelming experimental evidence available today (Webber and Lubitz 2001).

A more reasonable estimate of the asymmetry ratio $R_{B/A}$ could be made based on an assignment arising from earlier theoretical predictions of the spin density distribution among the pyrrole nitrogens (Plato, Krauss et al. 2003). According to the calculations by Plato et al. for both

P_A and P_B , only ring II, ring III and ring IV nitrogen atoms carry significant spin density while only a small fraction is located on the ring I nitrogen. Comparing experimental data from Table 1 with the predicted ^{14}N electron-nuclear hyperfine couplings (Plato, Krauss et al. 2003), we tentatively assign two ^{14}N groups $[\text{N}_1, \text{N}_2, \text{N}_3]$ and $[\text{N}_4, \text{N}_5, \text{N}_6]$ to the ring III, ring II and ring IV atoms of P_B and P_A , respectively. In this case, using the ratio of the average isotropic couplings, we obtain $R_{B/A} \approx 3$. This value is very close to $R_{B/A} \approx 2.8$ predicted theoretically for the “bare” dimer (Plato, Krauss et al. 2003) and $R_{B/A} \approx 2.6$ more recently for the entire PSI protein-pigment complex (Saito and Ishikita 2011). Also this is comparable to the asymmetry ratio $\approx 2:1$ measured for the primary donor cation radicals in bacterial reaction centers of *Rhodospseudomonas sphaeroides* R-26 (Lendzian, Huber et al. 1993) and *Rhodospseudomonas viridis* (Webber and Lubitz 2001).

As a final remark, we would like to point out that the HYSCORE data obtained in this work allow for a comparison of sensitivities of two microwave bands and the effect of an increased Zeeman interaction with respect to its effect on resolution of ^{14}N -HYSCORE spectroscopy. Comparing the ^{14}N -HYSCORE spectra of the same paramagnetic center $P_{700}^{+\bullet}$ shown in **Figures 2.2-5**, it is obvious that sensitivity of the X-band with respect to weakly coupled nuclei (N_3 - N_6 in our case) is dramatically higher than that of Q-band. This is because Zeeman interaction at Q-band is on the order of ≈ 3 MHz, significantly higher than the size of the quadrupole $K < 1$ MHz and half of the electron-nuclear hyperfine $A/2 < 1$ MHz interactions. While higher frequency bands are more sensitive to strongly interacting nuclei and are complimentary to lower microwave frequency data, small quadrupole and electron-nuclear ^{14}N couplings are typical for biologically relevant paramagnetic species and often carry particularly valuable spectroscopic information. Thus, the authors would like to suggest using a microwave frequency below X-band to enhance

HYSCORE sensitivity towards weakly coupled nuclei and, potentially, to provide important structural information not accessible by HYSCORE at X- and higher microwave frequency bands.

Section 4

Summary and outlook

A combination of 4-pulse and 6-pulse HYSCORE, each at two different microwave frequency bands (X- and Q-band), was applied to map the electron spin density distribution in the primary donor cation radical $P_{700}^{+\bullet}$ of the frozen PSI solution from cyanobacteria. Six distinct types of ^{14}N and two ^1H nuclei were resolved by these combinations of HYSCORE methods, yielding estimates of their magnetic interaction parameters, i.e. principal values of the electron-nuclear hyperfine as well as quadrupole interaction tensors (for ^{14}N). All the detected ^{14}N nuclei were tentatively assigned to the pyrrole ring nitrogen atoms of the $P_{700}^{+\bullet}$ radical, indicating delocalization of the electron spin density over both Chl a and Chl a' halves of the P_{700} heterodimer. While precise assignment of the detected ^{14}N would require single crystal HYSCORE data obtained at multiple orientations, the spectra measured for frozen solutions permitted an estimate of the upper limit of the electron spin density asymmetry of $P_{700}^{+\bullet}$ as $R_{\text{B/A}}^{\text{upper}} \approx 5.6$. More reliable estimates based on earlier theoretical predictions yielded $R_{\text{B/A}} \approx 3$, a value comparable to the asymmetry observed for the primary electron donor cation radical in bacterial reaction centers.

More precise and detailed information may be obtained by applying the multi-frequency HYSCORE approach presented here to single crystals of PSI. As compared to orientationally disordered frozen solutions, single crystals are expected to provide significantly less crowded, and more importantly, orientation resolved HYSCORE spectra. This would potentially lead to improved experimental accuracy, aid in detection of still missing ^{14}N hyperfine interactions and

provide unambiguous assignment of the measured hyperfine couplings. This approach may finally yield an accurate electron spin density map of $P_{700}^{\dot{\bullet}}$ radicals in PSI.

CHAPTER 2 REFERENCES

- Bratt, P. J., O. G. Poluektov, et al. (2000). "The g-factor anisotropy of plant chlorophyll a(center dot)." Journal of Physical Chemistry B **104**(30): 6973-6977.
- Bratt, P. J., M. Rohrer, et al. (1997). "Submillimeter high-field EPR studies of the primary donor in plant photosystem I P700." Journal of Physical Chemistry B **101**(47): 9686-9689.
- Breton, J., E. Nabedryk, et al. (1999). "FTIR Study of the Primary Electron Donor of Photosystem I (P700) Revealing Delocalization of the Charge in P700+and Localization of the Triplet Character in 3P700." Biochemistry **38**(36): 11585-11592.
- Budil, D. E. and M. C. Thurnauer (1991). "The chlorophyll triplet state as a probe of structure and function in photosynthesis." Biochimica et biophysica acta **1057**(1): 1-41.
- Chatterjee, R., S. Milikisiyants, et al. (2011). "High-Resolution Two-Dimensional ^1H and ^{14}N Hyperfine Sublevel Correlation Spectroscopy of the Primary Quinone of Photosystem II." Biochemistry **50**(4): 491-501.
- Chion, B. and J. Lajzerowiczbonneteau (1980). "Hydrogen-Bonds and Short Intermolecular Contacts Involving Nitroxide Groups in Crystals." Acta Crystallographica Section B-Structural Science Crystal Engineering and Materials **36**(Apr): 998-1000.
- Chitnis, P. R. (1996). "Photosystem I." Plant physiology **111**(3): 661-669.
- Chitnis, P. R., Q. Xu, et al. (1995). "Function and organization of Photosystem I polypeptides." Photosynthesis research **44**(1-2): 23-40.
- Deligiannakis, Y., M. Louloudi, et al. (2000). "Electron spin echo envelope modulation (ESEEM) spectroscopy as a tool to investigate the coordination environment of metal centers." Coordination Chemistry Reviews **204**(1): 1-112.
- Den Blanken, H. J. and A. J. Hoff (1983). "High-resolution absorbance-difference spectra of the triplet state of the primary donor P-700 in Photosystem I subchloroplast particles measured with absorbance-detected magnetic resonance at 1.2 K. Evidence that P-700 is a dimeric chlorophyll complex." Biochimica et Biophysica Acta (BBA) - Bioenergetics **724**(1): 52-61.
- Dikanov, S. A., A. M. Tyryshkin, et al. (2000). "Intensity of cross-peaks in hyscore spectra of $S = 1/2$, $I = 1/2$ spin systems." Journal of magnetic resonance **144**(2): 228-242.
- Dikanov, S. A., L. Xun, et al. (1996). "Orientationally-Selected Two-Dimensional ESEEM Spectroscopy of the Rieske-Type Iron-Sulfur Cluster in 2,4,5-Trichlorophenoxyacetate Monooxygenase from *Burkholderia cepacia* AC1100." Journal of the American Chemical Society **118**(35): 8408-8416.

- Diller, A., E. Roy, et al. (2007). "15N photochemically induced dynamic nuclear polarization magic-angle spinning NMR analysis of the electron donor of photosystem II." Proceedings of the National Academy of Sciences of the United States of America **104**(31): 12767-12771.
- Flanagan, H. L. and D. J. Singel (1987). "Analysis of 14N ESEEM patterns of randomly oriented solids." The Journal of Chemical Physics **87**(10): 5606-5616.
- Fleissner, M. R., M. D. Bridges, et al. (2011). "Structure and dynamics of a conformationally constrained nitroxide side chain and applications in EPR spectroscopy." Proceedings of the National Academy of Sciences **108**(39): 16241-16246.
- Frank, H. A., M. B. McLean, et al. (1979). "Triplet states in photosystem I of spinach chloroplasts and subchloroplast particles." Proceedings of the National Academy of Sciences of the United States of America **76**(10): 5124-5128.
- Fromme, P. (1996). "Structure and function of photosystem I." Current opinion in structural biology **6**(4): 473-484.
- Golbeck, J. H. (1992). "Structure and Function of Photosystem I." Annual Review of Plant Physiology and Plant Molecular Biology **43**(1): 293-324.
- Golbeck, J. H. (1994). "Photosystem I in Cyanobacteria." 319-360.
- Guo, W., M. Zhao, et al. (2019). "Developments towards synthesis of N-heterocycles from amidines via C–N/C–C bond formation." Organic Chemistry Frontiers **6**(13): 2120-2141.
- Höfer, P., A. Grupp, et al. (1986). "Hyperfine sublevel correlation (hyscore) spectroscopy: a 2D ESR investigation of the squaric acid radical." Chemical Physics Letters **132**(3): 279-282.
- Holt, A., L. Rougier, et al. (2010). "Order Parameters of a Transmembrane Helix in a Fluid Bilayer: Case Study of a WALP Peptide." Biophysical Journal **98**(9): 1864-1872.
- Holzwarth, A. R., M. G. Muller, et al. (2006). "Ultrafast transient absorption studies on Photosystem I reaction centers from *Chlamydomonas reinhardtii*. 2: Mutations near the P700 reaction center chlorophylls provide new insight into the nature of the primary electron donor." Biophysical Journal **90**(2): 552-565.
- Hustedt, E. J., R. A. Stein, et al. (2006). "Dipolar Coupling between Nitroxide Spin Labels: The Development and Application of a Tether-in-a-Cone Model." Biophysical Journal **90**(1): 340-356.
- Im, W., S. Jo, et al. (2012). "An ensemble dynamics approach to decipher solid-state NMR observables of membrane proteins." Biochimica et Biophysica Acta (BBA) - Biomembranes **1818**(2): 252-262.

- Jordan, P., P. Fromme, et al. (2001). "Three-dimensional structure of cyanobacterial photosystem I at 2.5 Å resolution." Nature **411**(6840): 909-917.
- Käss, H., P. Fromme, et al. (2001). "Orientation and Electronic Structure of the Primary Donor Radical Cation in Photosystem I: A Single Crystals EPR and ENDOR Study." The Journal of Physical Chemistry B **105**(6): 1225-1239.
- Kasumaj, B. and S. Stoll (2008). "5- and 6-pulse electron spin echo envelope modulation (ESEEM) of multi-nuclear spin systems." Journal of magnetic resonance **190**(2): 233-247.
- Käβ, H., P. Fromme, et al. (1996). "Quadrupole parameters of nitrogen nuclei in the cation radical P700.+ determined by ESEEM of single crystals of photosystem I." Chemical Physics Letters **257**(1-2): 197-206.
- Lendzian, F., M. Huber, et al. (1993). "The electronic structure of the primary donor cation radical in Rhodospirillum rubrum R-26: ENDOR and TRIPLE resonance studies in single crystals of reaction centers." Biochimica et Biophysica Acta (BBA) - Bioenergetics **1183**(1): 139-160.
- Lieb, J. (2008). "Defeating Cancer With Antidepressants." ecancermedicalsecience.
- Liesum, L. and A. Schweiger (2001). "Multiple quantum coherence in HYSCORE spectra." Journal of Chemical Physics **114**(21): 9478-9488.
- Lubitz, W. (2003). "Photochemical processes in photosynthesis studied by advanced electron paramagnetic resonance techniques." Pure and Applied Chemistry **75**(8): 1021-1030.
- Marshall, T. M. (2015). "Lithium as a Nutrient." J. Amer. Phys. Surg. **20**(4): 104-109.
- Müller, M. G., J. Niklas, et al. (2003). "Ultrafast Transient Absorption Studies on Photosystem I Reaction Centers from Chlamydomonas reinhardtii. 1. A New Interpretation of the Energy Trapping and Early Electron Transfer Steps in Photosystem I." Biophysical Journal **85**(6): 3899-3922.
- Najdanova, M., G. J. Janssen, et al. (2015). "Analysis of electron donors in photosystems in oxygenic photosynthesis by photo-CIDNP MAS NMR." Journal of photochemistry and photobiology. B, Biology **152**(Pt B): 261-271.
- Özdirekcan, S., C. Etchebest, et al. (2007). "On the Orientation of a Designed Transmembrane Peptide: Toward the Right Tilt Angle?" Journal of the American Chemical Society **129**(49): 15174-15181.
- Petrenko, A., A. L. Maniero, et al. (2004). "A High-Field EPR Study of P700+• in Wild-Type and Mutant Photosystem I from Chlamydomonas reinhardtii†,‡." Biochemistry **43**(7): 1781-1786.

- Plato, M., N. Krauss, et al. (2003). "Molecular orbital study of the primary electron donor P700 of photosystem I based on a recent X-ray single crystal structure analysis." Chemical Physics **294**(3): 483-499.
- Plato, M., H.-J. Steinhoff, et al. (2002). "Molecular orbital study of polarity and hydrogen bonding effects on the g and hyperfine tensors of site directed NO spin labelled bacteriorhodopsin." Molecular Physics **100**(23): 3711-3721.
- Polienko, J. F., T. Schanding, et al. (2008). "Studies toward the Synthesis of 4-(2-R-ethyl)amino-2,2,5,5-tetramethyl-3-imidazoline 1-Oxyls. Nucleophilic Substitution of Bromide in the N-Alkyl Chain of the 1,2,4-Oxadiazol-2-one Precursor." The Journal of Organic Chemistry **73**(2): 502-510.
- Poluektov, O. G., L. M. Utschig, et al. (2002). "Electronic Structure of the P700 Special Pair from High-Frequency Electron Paramagnetic Resonance Spectroscopy." Journal. Physical Chemistry B **106**(35): 8911-8916.
- Ptushenko, V. V., D. A. Cherepanov, et al. (2008). "Semi-continuum electrostatic calculations of redox potentials in photosystem I." Photosynthesis Research **97**(1): 55-74.
- Rink, T., J. Riesle, et al. (1997). "Spin-labeling studies of the conformational changes in the vicinity of D36, D38, T46, and E161 of bacteriorhodopsin during the photocycle." Biophysical Journal **73**(2): 983-993.
- Saito, K. and H. Ishikita (2011). "Cationic State Distribution over the P700 Chlorophyll Pair in Photosystem I." Biophysical Journal **101**(8): 2018-2025.
- Schrauzer, G. N. (2002). "Lithium: Occurrence, Dietary Intakes, Nutritional Essentiality." Journal of the American College of Nutrition **21**(1): 14-21.
- Schweiger, A. and G. Jeschke (2001). Principles of pulse electron paramagnetic resonance. New York, Oxford University Press.
- Setif, P. and K. Brettel (1990). "Photosystem-I Photochemistry under Highly Reducing Conditions - Study of the P700 Triplet-State Formation from the Secondary Radical Pair (P700⁺-A1⁻)." Biochimica Et Biophysica Acta **1020**(3): 232-238.
- Smirnova, T. I., A. I. Smirnov, et al. (2007). "Geometry of hydrogen bonds formed by lipid bilayer nitroxide probes: A high-frequency pulsed ENDOR/EPR study." Journal of the American Chemical Society **129**(12): 3476-+.
- Srinivasan, N. and J. H. Golbeck (2009). "Protein-cofactor interactions in bioenergetic complexes: The role of the A(1A) and A(1B) phyloquinones in Photosystem I." Biochimica Et Biophysica Acta-Bioenergetics **1787**(9): 1057-1088.

- Stoll, S. and A. Schweiger (2006). "EasySpin, a comprehensive software package for spectral simulation and analysis in EPR." Journal of Magnetic Resonance **178**(1): 42-55.
- Teutloff, C., W. Hofbauer, et al. (2001). "High-frequency EPR studies on cofactor radicals in photosystem I." Applied Magnetic Resonance **21**(3-4): 363-379.
- Vrieze, J., P. Gast, et al. (1996). "Structure of the Reaction Center of Photosystem I of Plants. An Investigation with Linear-Dichroic Absorbance-Detected Magnetic Resonance." The Journal of Physical Chemistry **100**(23): 9960-9967.
- W. G. J. Hoi, P. T. v. D. H. J. C. B. (1978). "The α -helix dipole and the properties of proteins." Nature **273**(443-446).
- Wang, R. L., V. Sivakumar, et al. (2003). "Mutation induced modulation of hydrogen bonding to P700 studied using FTIR difference spectroscopy." Biochemistry **42**(33): 9889-9897.
- Webber, A. N. and W. Lubitz (2001). "P700: the primary electron donor of photosystem I." Biochimica Et Biophysica Acta-Bioenergetics **1507**(1-3): 61-79.
- Webber, A. N. and W. Lubitz (2001). "P700: the primary electron donor of photosystem I." Biochimica et biophysica acta **1507**(1-3): 61-79.
- Woldman, Y. Y., S. V. Semenov, et al. (2009). "Design of liposome-based pH sensitive nanoSPIN probes: nano-sized particles with incorporated nitroxides." The Analyst **134**(5): 904.
- Young, W. (2009). "Review of Lithium Effects on Brain and Blood." Cell Transplantation **18**(9): 951-975.
- Zech, S. G., W. Hofbauer, et al. (2000). "A Structural Model for the Charge Separated State in Photosystem I from the Orientation of the Magnetic Interaction Tensors." The Journal of Physical Chemistry B **104**(41): 9728-9739.